

ORGANIC MATERIALS FOR THE IMPROVEMENT AND UNDERSTANDING OF
ELECTROCHEMICAL DEVICES

BY

AARON PETRONICO

DISSERTATION

Submitted in partial fulfillment of the requirements
for the degree of Doctor of Philosophy in Chemistry
in the Graduate College of the
University of Illinois at Urbana-Champaign, 2018

Urbana, Illinois

Doctoral Committee:

Professor Ralph G. Nuzzo, Chair
Professor Andrew A. Gewirth
Assistant Professor Joaquín Rodríguez-López
Professor Paul V. Braun

Abstract

The contents of this thesis focus on how organic materials can be applied to improve Li⁺ based batteries. There is specific focus mostly on cathode materials and a single project involving electrolytes. For cathodes the main focus is how quinone polymers can be applied as Li⁺ cathodes and results in a 4e⁻ cathode with record breaking capacity. We then go on to do some minor mechanistic and fundamental studies. The second cathode focus is how organic materials can augment existing technology. In this regard we investigate how alkyl phosphonates can form monolayer coating on Lithium Manganese Oxide cathode particles to suppress Mn dissolution during cycling. Finally we modify Li-S cathodes by chemically crosslinking poly-sulfide with conductive poly aniline to increase cycle life and cathode sulfur loadings. To improve Li⁺ electrolytes we demonstrate that persistently porous organic cages can serve as host structures to form solid-liquid electrolyte nano-composites. Taken together this work demonstrates the innovative impact Organic materials can have on battery technology.

Acknowledgement

A lesson beyond science that I have learned is that your mentors influence not only your learning and success, but your perception of a subject. To this end I thank Dr. Ralph Nuzzo, and Dr. Andy Gewirth for rekindling a love for science and supporting my success.

I thank Timothy Money Penny for his assistance on cage related project as that was an enjoyable collaboration and enabled some very novel and interesting science. Kimberly Mikayla, Maggie, and Bruno were both helpful collaborators and great friends.

Great progress is not made without strong emotional support, and ample mental distractions and to that end I would like to thank Alex Stanton.

I am eternally grateful for a strong network of friends in the program whom supported me both emotionally and scientifically and to that end would like to acknowledge Chris, Tommy, Jenny, Kim S, Kim T, Siraj, and Connor.

Finally I must acknowledge family and those who I have known and loved so long they feel like family, Cornelius, Mom, Dad, Alex, Louis, Greg, Bear, and Jen. You cannot truly achieve your potential without pushing yourself near your limits. It's during those times that you are at your most vulnerable and in need of the most support and these people were vital in providing that support.

Table of Contents

Chapter 1 Energy Storage Devices to Meet Global Energy Challenges.....	1
1.1 Global Energy Challenges	1
1.2 Specific Challenges Facing Li-Ion Batteries	2
1.2.1 An Overview of Li-Ion Battery Chemistry	2
1.2.2 Challenges of Modern Li-Ion Anode Technology	3
1.2.3 Challenges of Modern Li-Ion Cathode Technology	4
1.2.4 Challenges of Modern Li-Ion Electrolyte Technology	4
1.3 An Overview of Organic Quinone Cathode Material	6
1.3.1 Preface.....	6
1.3.2 Fundamentals of Quinone Redox.....	6
1.3.3 Monomeric Quinone Cathode Materials.....	7
1.3.4 Polymeric Quinone Cathode Materials.....	8
1.4 Thesis Outline	8
1.4.1 Chapter 2.....	8
1.4.2 Chapter 3.....	9
1.4.3 Chapter 4.....	9
1.4.4 Chapter 5.....	9
1.5 Figures.....	9
Chapter 2 Polymer Organic Cathodes.....	11
2.1 Towards a Four-Electron Redox Quinone Polymer for High Capacity Lithium Ion Storage.....	11
2.1.1 Abstract	11

2.1.2 Introduction.....	11
2.1.3 Results and Discussion	13
2.1.3.1 Characterization of LiDHAQS and DHAQS.....	13
2.1.3.2 Cyclic Voltammetry of LiDHAQS and 1,4 PAQ.....	15
2.1.3.3 Galvanostatic Cycling of LiDHAQS.....	17
2.1.3.4 Long term Cycling of LiDHAQS	18
2.1.3.5 Discussion of the 4 e ⁻ , 4Li ⁺ Storage Mechanism of LiDHAQS	19
2.1.4 Conclusion	20
2.1.5 Experimental Section.....	20
2.1.5.1 Synthesis of LiDHAQS.....	20
2.1.5.2 Conversion of LiDHAQS to DHAQS.....	21
2.1.5.3 Elemental Analysis	22
2.1.5.4 Solid State ¹³ C and ⁷ Li MAS NMR Spectroscopy	22
2.1.5.5 Gel Permeation Chromatography	23
2.1.5.6 Potentiostatic Evaluations of LiDHAQS and 1,4-PAQS.....	23
2.1.5.7 Galvanostatic Evaluations of LiDHAQS	24
2.2 Evaluating Polymerization Methods Effect on Electrochemical Properties of Anthraquinone Polymer Cathodes.....	25
2.2.1 Abstract	25
2.2.2 Introduction	25
2.2.3 Results and Discussion.....	25
2.2.3.1 Galvanostatic Cycling of Polyamino Anthraquinone (PAQN) Polyphenylanthraquinonyl Sulfide (PAQS) and Polyanthraquinone	25

2.2.3.2 Galvanostatic Rate Studies of Polyamino Anthraquinone (PAQN)	
Polyphenylanthraquinonyl Sulfide (PAQS) and Polyanthraquinone.....	26
2.2.4 Conclusions	27
2.3 Understanding Stress Behavior in Poly-Anthraquinone Cathodes	27
2.3.1 Abstract	27
2.3.2 Introduction	27
2.3.3 Results and Discussion	28
2.3.4 Conclusions	29
2.3.5 Experimental	29
2.4 Figures, Schemes, and Tables	31
Chapter 3 Solid-Liquid Lithium Electrolyte Nanocomposites Derived From Porous Molecular	
Cages	42
3.1 Abstract	42
3.2 Introduction.....	42
3.3 Results and Discussion	44
3.4 Conclusion	49
3.5 Experimental Methods	49
3.5.1 General	49
3.5.2 Materials	50
3.5.3 Characterization	50
3.5.3.1 Solution NMR Spectroscopy	50
3.5.3.2 Solid State ⁷ Li MAS NMR Spectroscopy	50
3.5.3.3 Thermogravimetric Analysis	51

3.5.3.4 SEM and EDS	52
3.5.3.5 Fourier Transform Infrared Spectroscopy (FTIR)	52
3.5.3.6 Elemental Analysis	52
3.5.4 Preperation of SLEN	52
3.5.5 Potentiostatic Electrochemical Impedance Spectroscopy of Cage SLEN	53
3.5.6 Potentiostatic Evaluation of Anode Reaction Using Cage SLEN as Electrolyte	54
3.6 Figures and Tables	54
 Chapter 4 Controlling Interfacial Properties of Lithium-Ion Battery Cathodes with	
Alkylphosphonate Self-Assembled Monolayers.....	65
4.1 Abstract	65
4.2 Introduction	66
4.3 Results and Discussion	68
4.3.1 Surface Modification and Characterization of Model Alkylphosphonate Supported on	
Lithium Manganese Oxide	68
4.3.1.1 Effect of Surface Modification on LMO Cyclic Voltammetry.....	68
4.3.1.2 Impedance Measurements.....	71
4.3.1.3 XPS Measurements.....	72
4.3.1.4 Contact Angle Measurements.....	74
4.3.1.5 Computational Studies of Alkylphosphonate Modified LMO	75
4.3.2 Effect of Surface Modification on Battery Behavior	78
4.3.2.1 ICP-MS Studies of Mn Dissolution	78
4.3.2.2 Galvanostatic Cycling.....	79
4.4: Concluding Remarks.....	81

4.5 Experimental Section	82
4.6 Figures and Tables	86
Chapter 5 Li-S Conductive Polymer Hybrid Cathodes for Li-S batteries	97
5.1 Abstract	97
5.2 Introduction	97
5.3 Results and Discussion	98
5.4 Conclusions.....	101
5.5 Experimental	101
5.6 Figures and Tables	103
References	107

Chapter 1

Energy Storage Devices to Meet Global Energy Challenges

1.1 Global Energy Challenges

The two main driving forces behind energy storage research are the need to address environmental concerns related to energy production and technological limitations related to portable devices. The limited supply of fossil fuels and increasing concern over the effects of global warming have driven an increased interest in renewable environmentally benign fuel sources¹. While clean renewable technologies exist many suffer from issues involving intermittent weather driven supply² and logistical difficulties in grid intergration³. To facilitate wide spread implementation of renewable energy sources, efficient energy storage devices and innovative solutions to decrease energy use must be developed.

In addition to problems associated with intermittent green energy, the rapid advance in energy demands of portable devices necessitate more efficient storage. The processing power of portable computing devices follows an exponential curve increasing over time⁴. These more powerful device coupled with consumer trends towards thinner and lighter devices require energy storage which is more efficient with respect to both mass and volume. The resurgence in interest in the electric powered car⁵ has further driven demand for efficient storage.

Li-Ion batteries have emerged as a promising energy storage technology and have already seen wide spread implementation in portable electronics⁶, vehicles⁵, and hold potential for grid based storage^{2b, 7}. While Li-Ion batteries have proven robust in initial application, progress in their development has been outpaced by increase energy demands. In particular storage capacities have been limited by failure to safely implement Li metal anode⁸ and poor capacities of commercial cathodes⁹ while the safety of Li-Ion technology has been limited by current electrolytes.¹⁰

1.2 Specific Challenges Facing Li-Ion Batteries

1.2.1 An Overview of Li-Ion Battery Chemistry

A battery is a device used to store electrical energy in the form of chemical potential. A more familiar analogy would be that of rocks (symbolizing electrons) stored atop a hill and held back by a gate (an incomplete circuit). The rocks by virtue of their height have a large degree of potential energy just as electrodes when different enough in electrochemical potential have a large degree potential energy. When the gate atop the hill is opened (circuit is connected) the rocks flow down the hill from an area of large potential energy to and an area of low potential energy. Similarly, when we turn on our phones electrons flow from the battery and power the device until we once again break the circuit by turning the device off.

In a technical sense, reversible energy storage is achieved by selecting two electrochemical reactions with sufficiently different reactions potential and assembling them in such a way that when attached to an external circuit electricity spontaneously flows in one direction (discharge) and requires a source of energy to remove in the reverse direction (charging) (typical cell depicted in Figure 1.1). In a rechargeable cell there are three main components an anode which undergoes redox at a reducing potential, a cathode which undergoes redox at a more oxidative potential, and an electrolyte responsible for shuttling ions between electrodes during charge and discharge. The amount of energy held in a chemical cell (Watt-hours) is governed by how much current it can supply for a given time (Ampere-hours) multiplied by the difference in potential between the cathode and anode (Voltage)

Li-Ion chemistry was identified early on as a promising candidate for an anode material in rechargeable cells as its redox potential is one of the most reducing for known materials (~ -3 V vs NHE).¹¹ Additionally its small atomic size and low atomic weight means it has a very high

gravimetric and volumetric theoretical capacity. (3861 mAh g^{-1} and 2062 mAh cm^{-3} respectively)^{9b}. Unfortunately due to safety concerns Li metal cannot be directly used as an anode and substitutes had to be developed.

1.2.2 Challenges of Modern Li-Ion Anode Technology

The fundamental tension in developing high performance anodes is that the material must simultaneously react at a reducing potential to increase cell voltage, store a high degree of charge per unit mass or volume, and be stable over a long device lifetime. The first two qualities (chemical potential and energy density) are both inherently at odds with stability and as such usually involve either stabilizing unstable systems or increasing energy density of stable systems.

As mentioned above, modern Li ion materials don't use Li as their anode material. Lithium is both unstable chemically against many conventional electrolyte systems and under high current loads deposits in the form of branch like dendrites which can short circuit the cell. The most widely used anode material, and the one which has been successfully implemented in commercial products, is graphitic carbon¹². Graphitic carbon is cheap and widely available and safely intercalates Li-Ions at a potential similar to Li metal there by satisfying the condition of low chemical potential. Unfortunately, carbon's inherent limitation is that its theoretical capacity is low compared to Li metal (372 mAh g^{-1}). This low capacity has led to extensive research in alternative high-capacity anodes¹²⁻¹³ with silicon based materials being most promising due to large capacities (over 1000 mAh g). These anodes suffer from poor cycle life due to volumetric expansion and particle cracking.¹² Despite the advances in practical anode materials, the goal of anode chemistry is to move to Li metal anodes

1.2.3 Challenges of Modern Li-Ion Cathode Technology

Cathodes face conceptually similar problems in that they must be at as oxidizing a potential as possible to enable large cell voltages, must store a large quantity of charge per unit mass or unit volume, and must be stable over the lifetime of a device. Once again storing a large amount of charge at high potentials is at ends with stability and cathodes must strike a balance between the three goals.

The majority of commercial cathode technology has focused on metal oxide cathodes including, lithium cobalt oxide (LCO), lithium manganese oxide (LMO), lithium iron phosphate (LFP), lithium nickel cobalt manganese oxide (NCM), and Lithium nickel cobalt aluminum oxide (NCA).^{9b} These metal oxides are all of the class of “intercalation cathodes” as their basic chemical mechanism for Li⁺ storage is for the metal center to undergo redox with minimal structural change and Li⁺ occupy and vacate sites within the lattice.¹⁴ The intercalation cathodes generally have high levels of stability (less than 20% capacity loss over hundreds of cycles) and their redox potential is determined by the metal center and ranges from 3.5-5.0 V vs Li/Li⁺.^{9b} These materials lack high levels of charge storage generally averaging around 125mAh g⁻¹ and becoming less stable when attempting higher levels of charge storage.^{9b, 15}

In commercial batteries capacities of the anode and cathode are matched as to ensure the most gravimetrically and volumetrically efficient fabrication. Because of this, the mismatch between current cathode capacities and the graphitic anode severely hampers the efficiency of battery design and the search for higher capacity cathodes is of great interest.

1.2.4 Challenges of Modern Li-Ion Electrolyte Technology

The function of an electrolyte in a Lithium ion battery is to shuttle Li⁺ from anode to cathode and back in the presence of external discharging and charging loads respectively.

Electrolytes must contact both the anode and cathode to effectively shuttle ions and therefore must be stable at both reducing and oxidizing potentials. They must also show chemical compatibility with electrode materials and maintain high ionic conductivity and low electronic conductivity throughout device life.

The most common composition for a Li^+ electrolyte is a lithium containing salt dissolved in organic solvent¹⁶. The solvent is chosen depending on its compatibility with electrodes and ability to dissolve and transport lithium salts¹⁷. The most common solvents are linear or cyclic ethers and carbonates as the oxygen containing molecule allows coordination to Li ions and facilitates transport. The most common salts used are lithium hexafluorophosphate (LiPF_6), lithium bis(trifluoromethyl)imide (LiTFSI), and lithium perchlorate (LiClO_4). LiPF_6 has emerged as the leader for commercialization as it is much cheaper than LiTFSI and much less dangerous to work with than LiClO_4 . LiPF_6 is not without its own problems as trace water can hydrolyze the salt generating HF and degrading the cell.

Modern liquid electrolytes have adequate conductivities for applied purposes but all share two common problems which still need to be addressed. First, liquid electrolytes generally have low transference numbers which results in polarization of anions and cell degradation. Second, lithium metal plates in a dendritic fashion at high current loadings for almost all liquid electrolytes resulting in shorting and cell failure.^{10, 18} Solid electrolytes are generally viewed as the future solution to both these problems as they often have larger transference numbers and can have the mechanical durability necessary to suppress dendrite growth.¹⁹

1.3 An Overview of Organic Quinone Cathode Materials

1.3.1 Preface

The second chapter of this thesis will address advances made in organic quinone cathodes. While quinone cathode materials have slowly been gaining traction in the scientific literature²⁰, they remain an unfamiliar concept to many materials scientists. It is therefore appropriate to provide a brief overview of both fundamental principles behind the relevant chemistries as well as an overview of the field.

1.3.2 Fundamentals of Quinone Redox

The basic principle behind Li^+ storage is that a material is reduced taking on a net negative charge therefore encouraging the uptake of positively charged Li^+ ions. The chemistry most battery researchers are familiar with is the reduction of a metal center and subsequent intercalation of Li^+ . Organic carbonyls are a redox labile functional group and are the basis for quinone electrochemistry.

A carbon double bonded to oxygen is referred to as a carbonyl (**Figure 1.2a**) and is capable of undergoing a one electron reduction forming an oxygen anion and a carbon centered radical. Carbon centered radicals are unstable species except in specific cases and as such would not make for robust electrode materials. If instead of a single carbonyl two carbonyls are located adjacent to one another (**Figure 1.2b**) the product of the reduction of both carbonyls would result in a diradical which can quickly recombine into a carbon double bond. Simple alkyl dicarbonyls are still too unstable for practical use but addition of conjugated vinyl groups and acid salts can allow for stable reversible redox (**Figure 1.2c**). The reduction of these conjugated acid salts are energetically unfavorable and therefore reduce at potentials more useful for anode chemistry. If instead of linear conjugation, the dicarbonyl is conjugated through a six member ring system, the

resulting product of the reduction will have aromaticity and provide an energetic driving force for the reaction. (**Figure 1.2d**). These cycling dicarbonyls which form aromatics upon reduction are known as quinones as they make up the basis of carbonyl based cathode materials.

Quinone cathode materials are fundamentally interesting as they are capable of high gravimetric capacities albeit at lower voltages than metal oxide cathodes. (**Figure 1.3**). Gravimetric capacity is a measure of how much charge can be stored in a material per unit mass and its theoretical value is given by equation 1.1.

$$C_{gravimetric} = \frac{N F}{M_w} \quad (1.1)$$

Where $C_{gravimetric}$ is the gravimetric capacity, N is the number of electrons transferred in the reaction, F is faradays constant and M_w is the molecular weight. Quinones have a unique advantage over most oxides in that their chemistry stores two electrons/ Li^+ and can be further enhanced by the addition of more carbonyl groups resulting in capacities in excess of 500 mAh g^{-1} .²¹

1.3.3 Monomeric Quinone Cathode Materials

The first reports of quinone cathodes for lithium ion batteries utilized monomeric materials in traditional carbon and binder containing composites.^{20c, 22} The inherent problem with utilizing monomeric organic materials, is they are soluble in many common organic solvents including those used for Li ion battery electrolytes. The result is rapid capacity fade and lack of practical utility of these materials. Monomeric materials do deliver on the promise of high gravimetric capacity with the highest performing material being Li Rhodizoate which has a first cycle capacity of 580 mAh g^{-1} .²¹ To overcome the problem of dissolution multiple solutions have been proposed including chemically linking monomers to the binder phase²³ or current collector²⁴. Both these

method are relatively new and underexplored. Polymerization of monomeric redox active Quinones has emerged as the premier solution to insolubility.

1.3.4 Polymeric Quinone Cathode Materials

Polymerization of monomeric redox active quinones can in theory decrease solubility and increase stability of organic quinone cathodes.^{22b} Additionally polymers hold the potential to impart favorable materials properties as they can be cast as free standing films²⁵ or increase the electrical conductivity of an electrode.²⁶ Polymeric quinones have delivered on their promise of increased stability with multiple examples of insoluble cathodes with multi-hundred cycle lifetimes with minimal fade.^{22b, 26b, 27} While polymerization has increased the stability of these cathodes, energy densities lag behind their monomeric counterparts due to incorporation of non-active mass in the polymer and remains an important challenge.

1.4 Thesis Outline

1.4.1 Chapter 2

Chapter 2 will cover the work I have done on polymer organic cathodes. It will begin with my synthesis and characterization of LiDHAQS a four electron redox quinone polymer with record breaking gravimetric capacity. This material exhibits outstanding battery performance and pushes the boundaries of what is possible for stable polymer organic cathodes. Chapter 2 will then cover an unpublished study of how polymerization methods affect the battery performance properties of various polymer cathodes. Finally, I will describe work done in conjunction with the Gewirth group on understanding stress and strain in PAQ Quinone cathodes. Importantly this will include my procedure for the synthesis of PAQ which, while similar to published procedure will include notes for increased success for anyone wishing to continue the study

1.4.2 Chapter 3

Chapter 3 will cover my work in collaboration with the Moore group on macroscopically solid electrolytes utilizing porous organic cages. These materials represent a novel class of electrolytes which exhibit great conductivity although suffer from poor thermal stability and low Li concentration preventing facile plating and stripping of Li

1.4.3 Chapter 4

Chapter 4 will cover my work in collaboration with the Gewirth group on alkyphosphonic acid coatings on metal oxide cathode materials. These coatings provide interesting insight into how cathode-electrolyte interfaces operate and exhibit interesting materials properties.

1.4.4 Chapter 5

Chapter 5 will discuss work on hybrid Li-S cathodes with increased stability in sulfur loading through adhesion to electrically conducting polymers. Once again a procedural guide to continuing this work will be described therein.

1.5 Figures

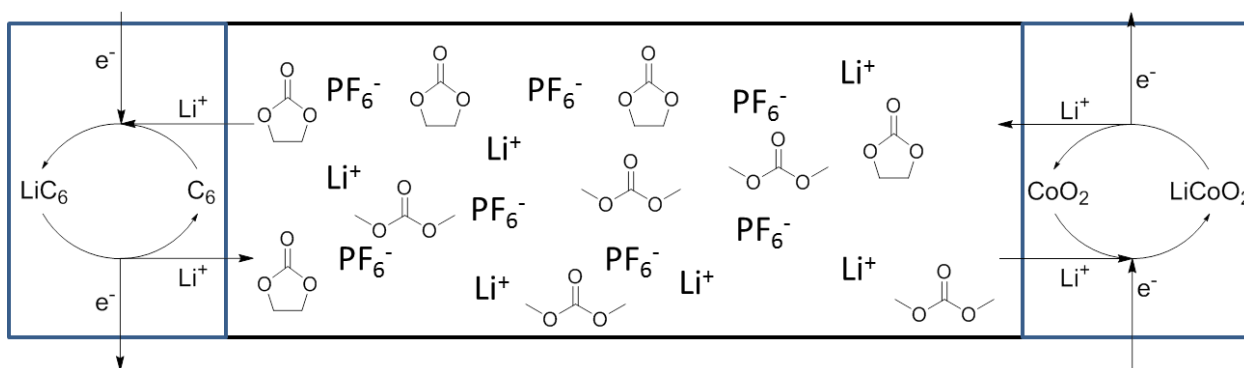


Figure 1.1. Typical Li ion cell chemistry

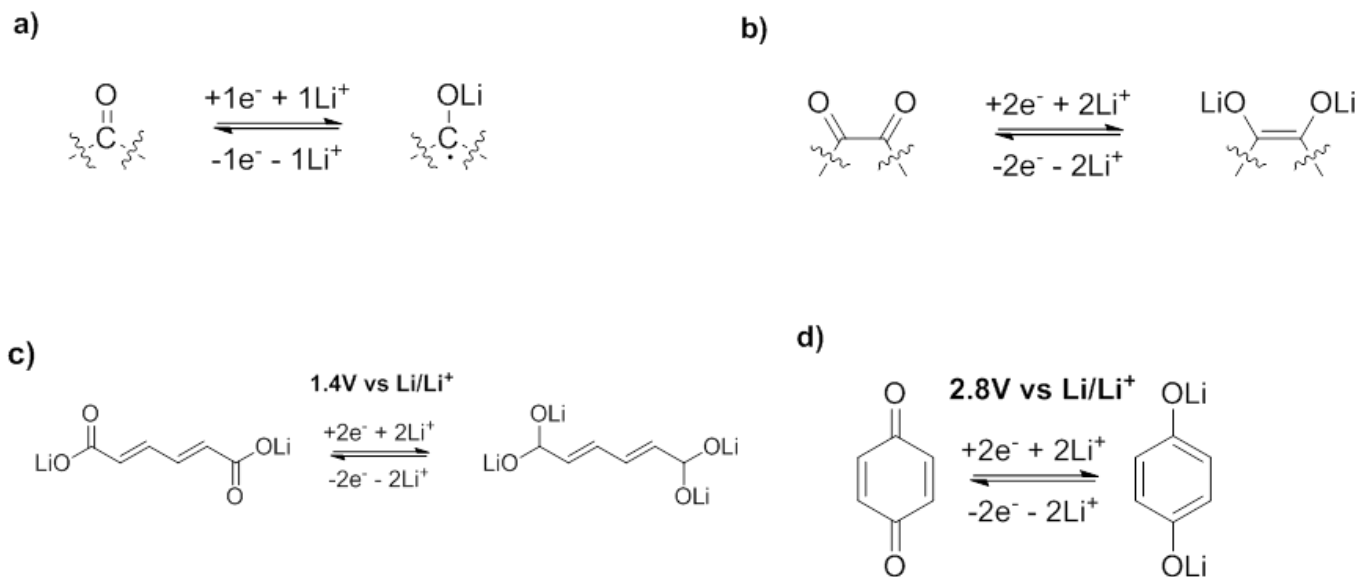


Figure 1.2. Fundamental reactions of carbonyl cathode molecules

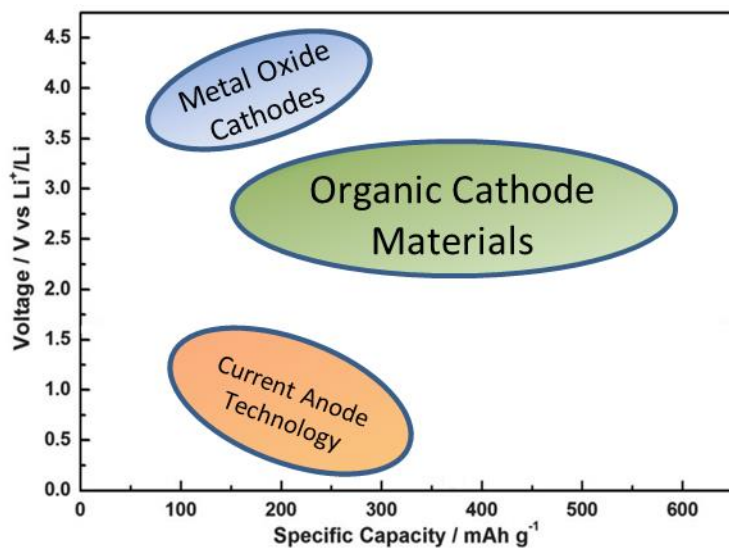


Figure 1.3. Performance space of anodes, metal oxide cathodes, and organic cathodes

Chapter 2

Polymer Organic Cathodes

2.1 Towards a Four-Electron Redox Quinone Polymer for High Capacity Lithium Ion Storage

2.1.1 Abstract

Despite recent advances, current polymeric organic cathode materials have failed to incorporate a high degree of lithium storage in a small molecular framework, resulting in low capacities relative to monomers. This report discloses the development of a lithium salt polymer of dihydroxyanthraquinone (LiDHAQS) capable of storing four Li^+ per monomer. The combination of storing four Li^+ per monomer and a low molecular weight monomer results in a capacity of 330 mA h g^{-1} , a record for this class of material. The additional redox events responsible for added Li^+ storage occur between 3.0-3.6 V vs Li/Li^+ resulting in an average discharge potential of 2.5 V vs Li/Li^+ . These metrics combined yield a high energy density of 825 W h kg^{-1} which is a 55% improvement over commercial lithium cobalt oxide (LCO). The high performance of LiDHAQS makes it a promising material for next generation Li^+ cathodes.

2.1.2 Introduction

Lithium-ion batteries are the focus of continual performance improvement efforts due to their utility in areas as diverse as portable electronics,⁶ transportation,⁵ and stationary energy storage.^{2b, 7}

A present-day lithium-ion battery consists of a graphitic anode, a lithium salt electrolyte in an organic solvent, and a metal oxide cathode. Anode technology has advanced tremendously over the past decade, and now boasts high capacities (300 mA h g^{-1} for commercial graphitic anodes and over 1000 mA h g^{-1} for more experimental technology) using inexpensive, abundant, and

environmentally benign elements such as C and Si.^{22a, 28} The performance capabilities of the corresponding metal oxide cathodes are much less impressive, affording practical capacities of 100-150 mA h g⁻¹ while relying on toxic and/or increasingly scarce elements for their synthesis.⁹ Anode and cathode capacities are typically matched in real batteries, this means that the full benefits of the higher capacity now achievable in the anode are not accessible. Consequently, substantial efforts are being expended to develop higher capacity cathode materials that might displace current commercial technologies with ones that are both robust in use and more environmentally benign over their service lifetime.

Organic cathodes are a promising class of materials as they hold the possibility of replacing metal oxides with less environmentally impactful materials, while also improving performance metrics.^{6a, 20b} Many different organic cathode chemistries have been explored and are the subject of recent reviews.²⁹ Organic carbonyl compounds have emerged as the most promising class of organic cathode material due to their high energy density and electrochemical stability.^{20c} Small molecule carbonyl based cathodes such as pyrene-4,5,9,10-tetraone³⁰ and lithium rhodizate²¹ can provide capacities of up to 580 mA h g⁻¹, yet frequently suffer from dissolution in common electrolytes leading to capacity fade. Recent reports have successfully addressed dissolution of monomers by chemical interactions with either the binder²³ or current collector phase²⁴, but these methods are not yet sufficiently developed to allow adoption in commercially relevant contexts.

Polymerization is a more general technique for preventing active material dissolution. Recent advances made in the synthesis of polymeric quinone cathodes as well as an exhaustive list of studied materials can be found in literature reviews.^{20c, 22b, 29} While the problem of quinone cathode dissolution has largely been solved by polymerization, polymer quinone cathodes have yet to achieve capacities similar to high performance monomers. The disconnect in performance

between monomeric and polymeric quinones stems mainly from the incorporation of only two Li^+ per monomeric unit in the polymers reported to date. The only reports of a quinone polymer cathode incorporating more than two Li^+ per monomer is the four-electron redox of polymer bound pyrene-4,5,9,10-tetraone^{27b} and the four-electron redox of poly(anthraquinone norbornene).³¹ In both examples of a four-electron redox quinone polymer, the large molecular framework of the monomer results in only modest capacities of the polymer (ca. 230 mA h g^{-1} for pyrene-4,5,9,10-tetraone^{27b} and 205 mA h g^{-1} for poly (anthraquinone norbornene)³¹). To our knowledge, the current record for highest capacity in a stable quinone polymer cathode is 275 mA h g^{-1} obtained using poly (benzoquinonyl sulfide) as the active material.³²

This report focuses on the synthesis, characterization, and electrochemical performance of a polymeric quinone cathode which can store four Li^+ in a small molecular framework. Lithiated poly (dihydroxyanthraquinonyl sulfide) (LiDHAQS) (**Figure 2.1**) is chosen as it contains a high degree of quinone functionality allowing four-electron redox from the fully oxidized poly (anthratetronyl sulfide) (ATQS) to the fully reduced lithiated poly (tetrahydroxyanthraquinonyl sulfide) (LiTHAQS) with concurrent storage of four Li^+ . This report demonstrates the effectiveness of incorporating a high number of redox active sites in a small molecular framework as a strategy for the design of high capacity cathodes.

2.1.3 Results and Discussion

2.1.3.1 Characterization of LiDHAQS and DHAQS

Table 2.1 reports the elemental analysis obtained for poly (dihydroxy-anthraquinonyl sulfide) (DHAQS), the protonated form of LiDHAQS. The table shows good agreement between the experimentally determined and predicted values for this material. Elemental analyses of

LiDHAQS were more problematic in consequence of the high Li content in quinone salt polymers, which causes interference during combustion analyses due to the formation of Li salts.³³

Figure 2.2a shows cross-polarization magic angle spinning (CPMAS) ¹³C solid state NMR data obtained from DHAQS. The figure shows the presence of peaks a-g which are associated with different C centers. While direct comparison with the monomeric 1,4-dihydroxy-5-mercaptoanthracene-9, 10-dione is not possible as its spectra is unavailable in the literature, assignment is made by reference to peaks in the solution spectra of monomeric dihydroxyanthraquinone (DHAQ).³⁴ Peaks d, e, and f in Figure 2a are all within 1.0 ppm of the corresponding peaks in the spectrum of the di-hydroxyanthraquinone monomer (**Table 2.2**). Peaks for carbon positions a, b, and c in the DHAQS monomer unit are expected to vary slightly relative to the equivalent carbons in the di-hydroxyanthraquinone monomer due to their proximity to the S³⁵ and are present as a broad resonance between 120-150 ppm. Peak g is also found in this region in the DHAQ monomer and is unresolved.

Figure 2.2b shows ⁷Li EchoMAS solid state NMR obtained from LiDHAQS. The spectrum exhibits a single broad peak with a maximum at 0.89 ppm. The single broad peak and small chemical shift are those anticipated for Li in a polymeric solid in a single environment.³⁶ Other possible sources of Li in our sample would be the LiCl left from the synthesis, or LiOH from contact with moisture in air. We can rule out LiCl and LiOH by comparison to spectra of LiCl and LiOH solid standards. (**Figure 2.6**)

Figure 2.2c reports the results of gel permeation chromatography (GPC) analyses of LiDHAQS and DHAQS. GPC shows that both polymers exhibit bimodal mass distributions centered around mass 2800 and 5300 Da. In LiDHAQS, these masses correspond to chain lengths of 10 and 19 monomers, respectively. Relative abundance of the 19mer, as compared to the 10mer,

drops when converting LiDHAQS to DHAQS, suggesting the polymer is cleaved by the HCl treatment. GPC shows masses as large as 25000 Da, which is equivalent to a polymer with 88 monomeric units. The molecular weight and chain length of the 10- and 19-mers in the LiDHAQS is larger than those reported for similar polymers which exhibited no dissolution of active material and long cycle life.^{33, 35, 37}

2.1.3.2 Cyclic Voltammetry of LiDHAQS and 1,4-PAQS

Figure 3a reports the cyclic voltammogram of first five cycles of LiDHAQS. The voltammogram shows two sets of broad, multi-featured redox waves, one at a lower (1.5 V-2.5 V vs. Li/Li⁺) and another at a higher (3.0 V- 3.6 V vs. Li/Li⁺) range of potentials. In an acetonitrile solution containing 0.1 M tetrabutyl ammonium perchlorate, monomeric anthraquinone (AQ) exhibits two distinct voltammetric peaks centered at -1.75 V and -1.2 V vs Ag/Ag⁺ corresponding to the AQ/AQ^{•-} and AQ^{•-} /AQ²⁻ redox couples respectively.³⁸ These potentials roughly scale to 1.8 V and 2.3 V vs. Li/Li⁺.³⁹ Slurry cast cathodes of monomeric AQ using typical Li⁺ containing electrolytes exhibit a single redox wave centered between 2.1-2.3 V vs. Li/Li⁺ (depending on electrolyte).^{35, 40} Dissolution of AQ, as is typically found with these slurries, results in additional features being seen in voltammograms of the monomer.⁴⁰ Polymerized anthraquinone typically exhibits a set of redox waves with multiple unresolved features centered between 2.1 V-2.3 V vs Li/Li⁺.^{25, 35} The multiple features in the voltammograms of the polymer are the result of both sample heterogeneity and electronic effects of the redox of one monomer unit on its neighbors.^{20c} Based on these literature precedents, the broad, multi-featured wave seen in our data between 1.5 V-2.5 V vs Li/Li⁺ is assigned to the anthraquinone-like redox of the b ring of LiDHAQS.

The LiDHAQS cathode material also exhibits redox waves at higher potentials. A slurry cast cathode of monomeric 5-amino-1,4-dihydroxyanthraquinone (ADHAQ) exhibits the typical

voltammetric peaks between 2.1 and 2.3 V vs. Li/Li⁺ described above for AQ and an additional two sets of peaks centered at 3.0 and 3.2 V vs. Li/Li⁺. The higher potential peaks are assigned to the additional redox made possible by oxygen functionality on the c ring.³⁷ Unfortunately, polymerized ADHAQ does not access this higher potential redox wave and cannot be used for comparison. A broadening of the peaks and the possible appearance of additional features, however, would be expected in analogy to the changes observed between monomeric and polymeric AQ. For this reason, the broad multi-featured redox wave between 3.0 V- 3.6 V vs. Li/Li⁺ in LiDHAQS is assigned to the additional redox centers on the c ring of LiDHAQS. To our knowledge, the redox of the c ring of LiDHAQS represents the highest voltage redox couple ever observed in a polymer quinone cathode.^{20c, 29a, 41} The high potential of this redox pair is attributed to the increase in local aromaticity, as described by Clar theory,⁴² upon reduction of the fully oxidized poly (anthraquinonyl sulfide) (ATQS) to the partially oxidized LiDHAQS. An increase in local aromaticity upon reduction has been shown in earlier reports to increase redox potentials in quinone cathode materials.⁴³

The first five cycles of the cyclic voltammogram of LiDHAQS exhibit little decay of activity for both the oxidation and reduction associated with the lower voltage redox couple (1.5 V-2.5 V vs. Li/Li⁺) and the reduction wave of the higher voltage couple (3.0 V- 3.6 V vs. Li/Li⁺). The oxidation wave of the higher voltage couple decreases in peak current density over the first five cycles. The decrease in oxidation peak current could be the result of irreversibility manifested in the sloping baseline or the presence of an apparent corrosive side reaction near the upper limit of the cyclic voltammogram.

Figure 3b reports the cyclic voltammogram of 1,4-poly(anthraquinonyl sulfide) (1,4-PAQS). The voltammogram shows a complex redox wave between 1.8 -2.4 V vs. Li/Li⁺

characteristic of an AQ polymer (vide supra). The absence of an additional high voltage redox couple suggests that the high potential wave in LiDHAQS is a result of the additional functionality on the c ring as that is the only chemical difference between the LiDHAQS and 1,4-PAQS monomer units. We note that other polyaniline type quinone polymers exhibit polymer backbone reactivity,^{27a, 37} and reported sulfur base polymers have not been cycled to such high potentials.^{33, 35, 44}

2.1.3.3 Galvanostatic Cycling of LiDHAQS

Figure 2.4a reports the galvanostatic cycling performance of a LiDHAQS half-cell at rate of 0.5 C. The Coulombic efficiency measured for the first cycle is 94% and increases upon cycling before stabilizing at 97%. The discharge capacities also increase upon cycling before reaching a maximum of 330 mA h g⁻¹ at cycle 31. The experimentally determined capacity of 330 mA h g⁻¹ is the largest reported discharge capacity for an organic polymer cathode and represents 87% of LiDHAQS theoretical capacity (380 mA h g⁻¹) or an average of 3.5 out of a possible 4 Li⁺ stored. Over more extended cycling, the discharge capacity slowly decays, reaching a final value of 263 mA h g⁻¹ at cycle 400. This decay represents a 20% loss over ca. 370 cycles corresponding to an average capacity loss of 0.05% per cycle. We believe that the capacity loss observed with cycling is closely related to Coulombic efficiency being below 100%. The Coulombic efficiency and capacity fade could be attributed to three possible phenomena. As seen from the voltammetry (Figure 2.3a) there may be slight irreversibility in the oxidation of LiDHAQS to ATQS. Alternatively the relatively low molecular weight of the polymer (Figure 2.2c) could fail to fully prevent dissolution of all oxidation states of LiDHAQS. Finally the side reactions involving the current collector could compromise the integrity of the cell over a long cycle life.

Figure 2.4b reports the charge and discharge curves at different cycles of a LiDHAQS half-cell cycled at a rate of 0.5C. After a minor change in charge and discharge profile from cycle 1 to cycle 10, the charge and discharge profile of LiDHAQS stays constant through cycle 400. LiDHAQS lacks a defined voltage plateau during both charge and discharge. Sloping charge and discharge curves have been observed previously in high performance polymer quinone cathodes, and are attributed to the electronic effect of one monomer unit on its neighbor upon redox.^{29b, 32, 45} The average discharge potential of LiDHAQS is 2.5 V, corresponding to a gravimetric energy density of 825 W h kg⁻¹. The 825 W h kg⁻¹ value is the highest gravimetric energy density yet found for a polymer cathode and represents a ca. 55% improvement over commercial lithium cobalt oxide (530 W h kg⁻¹).^{9a}

2.1.3.4 Long Term Cycling of LiDHAQS

Figure 2.5a reports the long term cycling behavior of LiDHAQS half cells at 1C and 2C. At both 1C and 2C, LiDHAQS exhibits an initial gravimetric capacity of 300 mA h g⁻¹. Over the first 500 cycles the cell ran at 1C decayed to 220 mA h g⁻¹ and the cell ran at 2C decayed to 210 mA h g⁻¹. These values correspond to 0.05% and 0.06% capacity loss per cycle at 1C and 2C, respectively. This rate of loss is virtually the same as obtained in the 0.5C cycling experiment.

Figure 2.5b reports the discharge capacity as a function of C-rate for a LiDHAQS half-cell. The LiDHAQS system displays an exceptionally high rate capability, with capacities of 350, 320, 294, 276, 260, and 236 mA h g⁻¹ at 0.25, 0.5, 1, 2, 5, and 10C, respectively. We further found that the LiDHAQS cathode recovers 83% (290 mA h g⁻¹) of the initial capacity (350 mA h g⁻¹) upon returning to a 0.25C rate. The loss of capacity over the 80 cycles reported in Figure 5a corresponds to an average loss of 0.2% per cycle, somewhat larger than that found when cycling

at 0.5C, suggesting that cycling at 5C and 10C yields a more hysteretic performance relative to that seen at the slower rates.

2.1.3.5 Discussion of the $4 e^-$, $4 Li^+$ Storage Mechanism of LiDHAQS

The strongest evidence for a $4 e^-$, $4 Li^+$ storage mechanism in LiDHAQS is the capacity obtained during galvanostatic charge and discharge. LiDHAQS delivers 330 mA h g^{-1} at 0.5C (Figure 2.4a) and 350 mA h g^{-1} at 0.25C (Figure 2.5b), which correspond to $3.5 Li^+$ and $3.7 Li^+$ stored per-monomer, respectively. The larger capacity of LiDHAQS as compared to anthraquinone-based polymers^{20c} is attributed to the additional redox event seen in the CV data between 3.0 V- 3.6 V vs. Li/Li⁺. As shown in Figure 3a and 3b, these data strongly suggest that the additional redox event in LiDHAQS is the result of the additional O functionality present in the c ring, findings that strongly support the $4 e^-$, $4 Li^+$ storage pathway described in Figure 2.1.

The experimentally determined $3.5 Li^+$ per monomer capacity is less than the ideal $4 Li^+$ capacity predicted from the monomer structure. The origin of this capacity drop could be the result of an inability to access the full mass of material upon charge and discharge, possibly due to the intrinsically poor electrical conductivity of the material. Additionally, ionic conductivity of Li^+ within the composite cathode may also be non-ideal with features of this transport limitation precluding access to the full $4e^-$ theoretical capacity of the storage process.

We note that a $3 Li^+$, $3e^-$ redox in LiDHAQS is unlikely as it would result in a free radical semi-quinone. It is well known that free-radical semi-quinones are unstable and readily disproportionate into quinone and hydroquinone species⁴⁶. In fact, the stabilization of semi-quinones is the subject of extensive research, requiring complex organometallic or metalloprotein scaffolds⁴⁶⁻⁴⁷. We therefore believe it is unlikely that our system invokes a 3-electron mechanism.

2.1.4 Conclusion

In conclusion we synthesized a polyphenyl sulfide polymer of 1, 4-dihydroxy-9, 10-anthraquinone (LiDHAQS) for use as a lithium-ion battery cathode material. We find that LiDHAQS is capable of undergoing redox on both the b and c ring of the monomer allowing storage of up to four lithium ions per monomer. Half-cell cycling of LiDHAQS shows this material is capable of 330 mA h g⁻¹ of reversible capacity with minimal fade over 400 cycles. The average discharge voltage of the LiDHAQS cell was 2.5 V vs. Li/Li⁺ which results in an energy density of 825 W h kg⁻¹. This represents a record high energy density for a long lived organic polymer cathode. These results taken together suggest LiDHAQS is a promising candidate for next generation cathode materials, and that increasing Li⁺ storage capability per monomer will be a valuable design principle moving forward with organic cathodes.

2.1.5 Experimental Section

2.1.5.1 Synthesis of LiDHAQS

All chemicals were purchased from Sigma Aldrich unless otherwise noted and were used as received. Reactions were carried out under dry, inert atmosphere unless otherwise noted. Synthesis of the lithium salt of poly (1, 4,-dihydroxyanthraquinonyl sulfide) (LiDHAQS) was carried out using a modified Philips method previously describe for related quinone polymers (**Scheme 2.1**). Inside an Ar filled glovebox, 5, 8-dichloro-1, 4-dihydroxyanthraquinone (DCIDHAQ) (0.250 g, 0.81 mmol) was added to 3.2 mL of anhydrous N-methyl pyrrolidinone (NMP) in a 10 mL round bottom flask with a stir bar. To this Li₂S (0.083 g, 1.8 mmol) was added and the flask was capped, removed from the glove box, and placed under N₂. The flask was then heated to 160 °C for 18 h. The reaction mixture was then cooled to room temperature and the resulting viscous liquid was poured into three centrifuge tubes each containing 10 mL of Et₂O. These tubes were then sonicated, cooled to 0 °C, and centrifuged. The Et₂O supernatant was

removed and the product washed with fresh Et₂O once more. The mixture was then washed twice with acetone after which a solid formed. The solid was washed with EtOH, H₂O, and then once with acetone. The solid was then dried in a vacuum oven overnight at 80 °C. The resultant solid was a dark blue brittle powder and yields were typically 80% or above. Poly (1, 4 anthraquinonyl sulfide) (1,4-PAQS) was synthesized by a similar procedure starting from 1, 4-dichloroanthraquinone and details are discussed in the Supplementary Information.

A few notes to experimentalists, the quality of Li₂S used in the reaction is paramount to its success. I have found that Li₂S present in our glovebox for prolonged periods produced inferior results. I never developed or worked on purification of the Li₂S and buying the salt in small samples then using it soon after opening provided consistent results. Additionally the “anhydrous” label of the NMP purchased from sigma is inconsistent and reliable results are best obtained with freshly dried and distilled NMP as described in the literature.⁴⁸ The washing steps involving ethanol and water are important to stability of the product. You will see a lot of blue supernatant washing away during these steps and washing should continue till the supernatant runs clear. (while not studied I always assumed this was soluble smaller oligomers) This washing in centrifuge tubes can go on for a while and become tedious and while I never revisited and optimized this procedure after gaining more experience with polymer purification I suspect a better method would be a prolonged stir of the resulting solid in a large quantity of ethanol followed by filtration and then a similar procedure with water

2.1.5.2 Conversion of LiDHAQS to DHAQS

To 100 mg of LiDHAQS, 2 mL of 1M HCl in H₂O was added and the mixture stirred under N₂ for 12 hours (**Scheme 2.2**). The resulting product is then washed three times with ice cold water

and once with acetone. The product is then dried at 80 °C in a vacuum oven overnight. The resulting solid was violet-red.

2.1.5.3 Elemental Analysis

C, H, N, S, Li, and Cl elemental analyses were carried out in the University of Illinois School of Chemical Sciences Micro-analysis Laboratory.

2.1.5.4 Solid State ^{13}C and ^7Li MAS NMR Spectroscopy

All ^{13}C and ^7Li solid-state NMR spectra were obtained in the SCS NMR facility using a Varian Unity Inova 300 NMR spectrometer (7.05 T) operating at a resonance frequency of ν_0 (^{13}C) = 75.47 MHz and ν_0 (^7Li) = 116.6 MHz at room temperature. A Varian/Chemagnetics 4 mm double-resonance APEX HX magic-angle spinning (MAS) probe was used for all experiments at a spinning rate of 10 kHz and two pulse phase modulation ^1H decoupling. Samples were ground in a mortar and pestle and packed into 4 mm zirconia rotors.

Experimental carbon chemical shift referencing, pulse calibration and cross-polarization condition were performed using powdered hexamethylbenzene (HMB), which has a chemical shift of 17.3 ppm (for the methyl peak) relative to the primary standard, trimethylsilane (TMS), at 0 ppm. For cross-polarization MAS (CPMAS) experiments, the ^1H 90 degree pulse width was 2.5 μs , the contact time was 8 ms, and the recycle delay was set to 2 s. 8000 scans were acquired with an acquisition time of 5 ms.

Experimental lithium chemical shift referencing, pulse calibration and setup were performed using 1M LiCl, which has a chemical shift of 0.00 ppm. Specific ^7Li pulse widths of 1.5 μs and recycle delays of 10 s were used, while 864 scans were acquired for the sample. The Hahn-echo pulse sequence ($(\pi/2)$ - τ - (π) - τ -acq, with τ =interpulse delays set to 100 μs for rotor-synchronization, i.e., the inverse of the spinning rate) was utilized as opposed to the regular one-

pulse sequence because this sequence yields spectra with a less distorted baseline due to the extra refocusing pulse.

2.1.5.5 Gel Permeation Chromatography

GPC analysis was carried out by Polymer Standards Service (Amherst, MA). Samples of LiDHAQS and DHAQS were dissolved in 0.01 M LiCl in NMP at 160 °C for 5 hours before being analyzed. The GPC system was equipped with PSS SECcurity 1260 HPLC-pump, a PSS SECcurity 1260 refractive index detector, and a set of PSS Gram 10 μm columns (30 Å, 100 Å, and 300 Å, 8 mm x 300 mm) The samples were analyzed at a concentration of 3 mg mL⁻¹ at a flow rate of 1.0 mL min⁻¹ at 80 °C.

2.1.5.6 Potentiostatic Evaluations of LiDHAQS and 1,4-PAQS

Cathodes were prepared by grinding with a mortar and pestle equal parts by weight LiDHAQS powder and conductive carbon (Super-P Li, Timcal Inc). The resulting powder was then ground with 10 wt% polytetrafluoroethylene (PTFE) in a mortar and pestle and the resulting material pressed onto an Al mesh current collector. Typical loading was ~1 mg cm⁻².

Potentiostatic experiments were performed in a cell made of a modified Swagelok tube fitting inside a glove box. The cell was assembled by layering Li metal (counter/ reference electrode), Whatman glass fiber paper (GF/F) as a separator, and electrolyte (1M bis(trifluoromethane)sulfonimide lithium salt (LiTFSI) in 2:1 v: v dioxolane: dimethoxyethane) before finally adding the cathode and sealing the cell. The experiments were conducted by using a CH Instruments (Austin, TX) electrochemical workstation. Cyclic voltammograms for LiDHAQS were conducted between 1.5-3.8 V vs. Li/Li⁺ at a scan rate of 1.0 mV s⁻¹. Cyclic voltammograms for 1,4-PAQS were conducted between 1.7-3.75 V vs. Li/Li⁺ at a scan rate of 1.0 mV s⁻¹.

2.1.5.7 Galvanostatic Evaluations of LiDHAQS

Cathodes were prepared similarly to section 4.6 with two notable changes. First, the type of carbon used was Ketjenblack (EC-600JD, AkzoNobel). Second, in place of hand grinding, carbon and polymer were mixed by planetary ball mill for 30 minutes.

Galvanostatic experiments were made using CR2032 coin cells obtained from MTI Corp. (Richmond, CA). The cell was assembled by first placing a 0.5 inch diameter circular piece of lithium in the base of the cell. A Whatman glass fiber paper (GF/F) was then placed on the lithium as separator and soaked in electrolyte (1M LiTFSI in 2:1 v:v Dioxolane : dimethoxyethane). The cathode was then placed on top of the separator and a stainless steel disc is placed on top as a spacer before placing a spring (MTI stainless steel wave spring for the CR2032 case) and the top cap. The cell was then sealed closed using an MTI hydraulic crimper. An MTI cycler (Richmond, CA) was used to cycle the cells. C rates were calculated using the mass active material in the cathode composite, assuming a working capacity of 330 mA h g⁻¹. Capacities are reported as a function of active material in the cathode. Blanks of carbon and PTFE were run to evaluate the contribution of carbon to the capacity and that value (typically 20-30 mA h g⁻¹) was subtracted from the overall capacity to obtain the reported results. Galvanostatic experiments were run between 1.6 V and 3.8 V vs Li/Li⁺. The lower limit was chosen as the galvanostatic curves exhibit a steep increase in slope indicative of full discharge. We note that a similar change in slope is not present for the charging cycles. 3.8V was chosen as a practical limit, as above this potential significant background reaction of the solvent occurs.

2.2 Evaluating Polymerization Methods Effect on Electrochemical Properties of Anthraquinone Polymer Cathodes

2.2.1 Abstract

The high capacity nature of polymeric quinone based organic cathode materials requires a deeper understanding of design principals for high performance materials. This report focuses on polymerizing the same redox active monomer (anthraquinone) by three different methods and evaluating the activity of each as a Lithium ion cathode. We find that Nickle catalyzed polymerization provides the best performance in terms of both capacity and stability.

2.2.2 Introduction

Quinone based cathodes for Li^+ batteries have attracted great interest due to their high gravimetric capacities.^{20a, b, 22} The general focus for the research has been increasing the energy density of these materials⁴⁹ while maintaining practically useful stability. The result has been individual reports been polymers generated by a variety of methods including polythioethers^{32-33, 49}, polyanilines^{27a, 37}, poly aromatics²⁵, polyimides⁵⁰, and alkyl side chain bound polymers^{27b, 30}. While all these polymers present interesting advances in the field, the reports are conducted by different labs with differing experimental conditions making direct comparison difficult. Herein we polymerize an anthraquinone monomer by three different polymerization methods (**Scheme 2.3**) and compare their performance as Li^+ cathodes.

2.2.3 Results and Discussion

2.2.3.1 Galvanostatic Cycling of Polyamino Anthraquinone (PAQN) Polyphenylanthraquinonyl Sulfide (PAQS) and Polyanthraquinone

Figure 2.7 displays the galvanostatic cycling of PAQ, PAQS, and PAQN. PAQ exhibits an initial capacity of 237 mAh g^{-1} and exhibits 102% of this capacity after 50 cycles. This intial

increase in capacity is consistent with the literature report for this polymer²⁵. PAQS exhibits an initial capacity of 223 mAh g⁻¹ and retains 69% of this capacity after 50 cycles. We note this is a high degree of capacity loss as compared to literature examples^{32-33, 49} of poly phenyl sulfide polymers. PAQN exhibits an initial capacity of 231 mAh g⁻¹ and retains 83% of this capacity after 50 cycles. This is consistent with literature reports of polyaniline based quinone cathodes.

It is apparent from a cycling standpoint, that the direct C-C linkage of PAQ is superior both in terms of overall gravimetric capacity, and capacity retention. As the polymerization method used to synthesize PAQ does not incorporate any additional atoms (and consequently non-active mass) into the monomer it makes sense that PAQ should have the highest gravimetric capacity. What is less clear is why this polymerization method yields the most stable cycling, but can possibly be attributed to the increased stability of C-C vs C-N or C-S bonds.

Figure 2.8 displays the charge and discharge curves of the final cycles of PAQ, PAQS, and PAQN. PAQ exhibits an average discharge potential of 2.2 V vs Li/Li⁺ and has the flattest discharge plateau of the three polymers studied. PAQS exhibits an average discharge voltage of 2.2 V vs Li/Li⁺ and exhibits a multi-feature charge and discharge curves. PAQN exhibits an average discharge voltage of 2.1V and displays a single voltage plateau.

The multi-feature nature of the PAQS can be attributed to the redox of a single center effecting neighbors as has been previously observed³², but may also indicate greater heterogeneity in synthesis products. It is unclear as to why PAQS and PAQS have such flat discharge curves as many polymer cathodes tend to redox across a wide range of voltages⁴⁹.

2.2.3.2 Galvanostatic Rate Studies of Polyamino Anthraquinone (PAQN) Polyphenylanthraquinonyl Sulfide (PAQS) and Polyanthraquinone

Figure 2.9 displays the galvanostatic cycling of PAQ, PAQS, and PAQN at different C rates. The fading behavior of PAQS and PAQN make comparison of capacity loss with increase of rate difficult, but we find that the rate performance of all materials similar .

2.2.4 Conclusions

While this section by no means constitutes a complete study on the different effects that polymerization methods have on cathode performance it represents a useful starting points. It is clear the Ni catalyzed direct C-C bond forming polymerization offer both the highest capacity, stability, potential, and rate capability, but the reason as to why remain unclear. This section can serve as an interesting starting point for future work.

2.3 Understanding Stress Behavior in Poly-Anthraquinone Cathodes

2.3.1 Abstract

In this section we synthesise literature reported PAQ. We demonstrate that PAQ-SuperP-CMC cathodes can be successfully cast on cantilevers and stress measurements obtained. We obtain data for stress cycling the cell in a Li based system and show the competence of the cathode in a NA based system. Most importantly the experimental section will include details of how to synthesize these polymers and cast the cathodes for any future students wishing to continue the project.

2.3.2 Introduction

The majority of research surrounding Quinone cathodes has focused on their outstanding battery performance and practical application. Little is known about the fundamental underpinning of their storage mechanisms or materials properties. Electrochemical stress is an analytical technique which has proved a rich source of information for probing a variety of battery systems.⁵¹ The

organic quinone cathodes provide an interesting system to study through stress as their materials properties and storage mechanism should be substantially different than the previously studied metal oxides. Additionally unlike metal oxides the storage in quinone polymers is Ion nonspecific so for the first time it should be possible to study the stress response of intercalating different cations into the same system.

2.3.3 Results and Discussion

Figure 2.10 displays cyclic voltamograms of PAQ-SuperP-CMC cathodes run at 1 mV/s in using two different cations. Figure 2.10a shows a system using a Li metal counter/reference electrode and 1M LiTFSI electrolyte and Figure 2.10b shows a system using a Na metal counter/reference electrode and 1M NaTFSI electrolyte. The difference of redox potential of $\sim 0.5V$ ($2.2 V$ vs Li/Li^+ and $1.5 V$ vs Na/Na^+) between the two systems. From the standard reduction potentials of the two reference electrodes ($-3.045 V$ vs NHE for Li and $-2.714 V$ vs NHE) we would expect a difference $0.33V$ meaning there is $\sim 170mV$ of unexplained shift suggesting a less facile reduction in the Na system. This is further supported by the greatly increased over potential between reduction and oxidation observed in the Na system ($800mV$) than in the Li system ($100mV$). Additionally we observe a splitting of the reduction peak in the NA reduction wave and repeatable noise in the oxidation wave. We do not have a current explanation for the noise. We hypothesize that the redox is less facile in the Na system as Na^+ are much alrge than Li^+ and as such their incorporation into higher order polymer sturcutres may be more difficult. The difficulty in Na incorporation may also cause increase differentiation in energy levels of the each of the one electron reduction which constitute the reductive wave resulting in the observed second feature.

Figure 2.11 Displays Voltamograms, electrochemical stress, and electrochemical stree derivative measurements in the Na and Li PAQ cathode systems. In the Li System (2.11a) we

observe the stress derivative being synchronous with the voltametric peaks. In the Na system there is asynchronicity between the stress derivative and the voltammetry suggesting mechanical change in the polymer does not directly corelated with Faradaic processes. While the oxidative wave is difficult to interpret due to its poor resolution, in the reduction it is clear that there is significant stress evolution prior to reduction. We hypothesize that this is due to the fact that unlike in the case of Li^+ where the small ionic radii allows a simple expansion of the native polymer conformation to acomidate the cation, the bulkier Na^+ requires significant conformation change and therefor a mechanical event must preceed reduction and Ion incorporation.

Figure 2.12 Displays stress studies of PAQ cathode in a LiTFSI system vs Li Counter/Reference at 1 mV/s and 0.05 mV/s. We observe that at slower scan rates we can differentiate thte two one electron processes in the reductive wave but still result in one wave in the oxidative case. Further there appears to be increased asynchronicity in the oxidative stress as compare to voltammetry and while the voltammetry at slower scan rates displays multiple reductive featuers there is only one reductive stress derivative feature.

2.3.4 Conclusions

While more studies must be conductive we have clearly shown some initial results that the PAQ cathode system can accommodate both Na and Li ions and successfully run stress on both systems. There significant differences between he Na and Li systems in both stress and voltammetry although the exact cause is yet unknown. Imporant additional experiments include, understanding the origin of the oxidative noise in the Na system, additional system containing another cation for comparison, and spectroscopic evidence for the proposed mechanical events which may occur when incorporating the larger Na^+ cation.

2.3.5 Experimental

Stress, and Voltametry are run using the standard instrumentation and setup as can be found in previous reports.^{51b}

Synthesis of PAQ

The synthesis of PAQ was done following previously reported procedure²⁵. A detailed account and helpful guidelines for synthesis follows:

Prior to starting the reaction an oil bath equipped with a thermometer and near a shlenk line is brought to 60 C.

A flame dried flask, stir bar, and septa is brought into an Ar filled glovebox. In the glove box to the flask in order is added 40mL of anhydrous DMF, 1.1grams of bis(1,5-cyclooctadiene)nickel(0) Ni(COD)_2 [0.004mol] , 0.625g [0.004mol] of 2,2'-bipyridine, 0.37mL [0.003mol] of 1,5-cyclooctadiene (COD), and 0.831g [0.003mol] of 1,4-Dichloroanthraquinone. An additional 10mL of DMF is used to wash down the sides of the flask of any solids which have stuck there.

Still in the glovebox the flask is then capped and brought out of the box and placed under dry N_2 line before being immersed in the 60C bath and allowed to stir for 48 hours.

(Notes for setup the Ni(COD)_2 should be bright yellow. If it is brownish yellow or has significant black quantities contact supplier and express you are not happy with the as received catalyst. Anhydrous DMF purchased from sigma works unreliably and should be distilled and dried before use.)

After 48 hours turn off the oil bath and allow the reaction flask to cool to room temperature. The

reaction is then poured into 50mL of 0.5M HCl and a yellow precipitate is generated. The solid is then separated from liquid by filtration and washed with DMF, 0.05M HCl, H₂O, and methanol. The solid is then dried at 80C for 6-12 hours. The resulting solid is dissolved in a minimal amount of chloroform. An equal amount of methanol is then layered on top of the chloroform by addition down the side of the flask and that biphasic mixture allowed to stand for 1-2 hours. The phases are then mixed and filtered and the solid dried at 80C under vacuum.

(Notes for workup don't get lazy with the molarities of listed HCl using too concentrated can compromise the reaction. The DMF wash is perhaps the most important since it you will get some amount of yellow color dissolving here (presumably lower order oligomers). Keep washing with DMF until the filtrant runs clear. This can also help if the reaction went poorly and didn't polymerize as well as it can lower yield but get rid of undesirable smaller chains. Perform the recrystallization as noted addition of the chloroform solution into a methanol solution results in an undesirable polymer skin which makes future processing difficult.)

2.4 Figures, Schemes and Tables

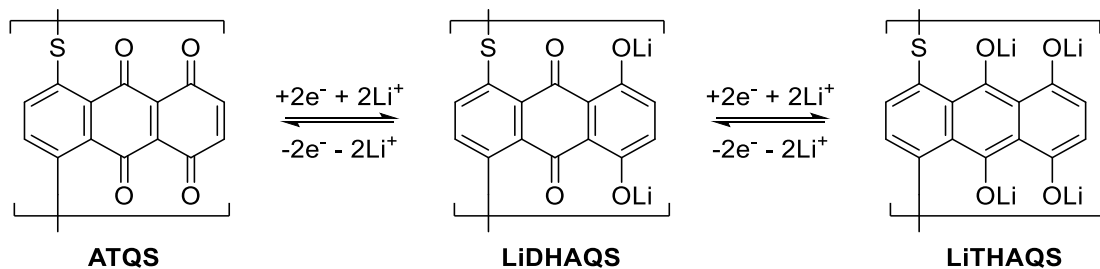


Figure 2.1. Four-electron redox pathway of LiDHAQS polymer

Table 2.1. Elemental analysis of DHAQS

Element	Theoretical Mass (%)	Observed Mass (%)
C	62.22	62.8
H	2.24	2.28
N	0	0.48
S	11.86	11.1
Li	0	0
Cl	0	0

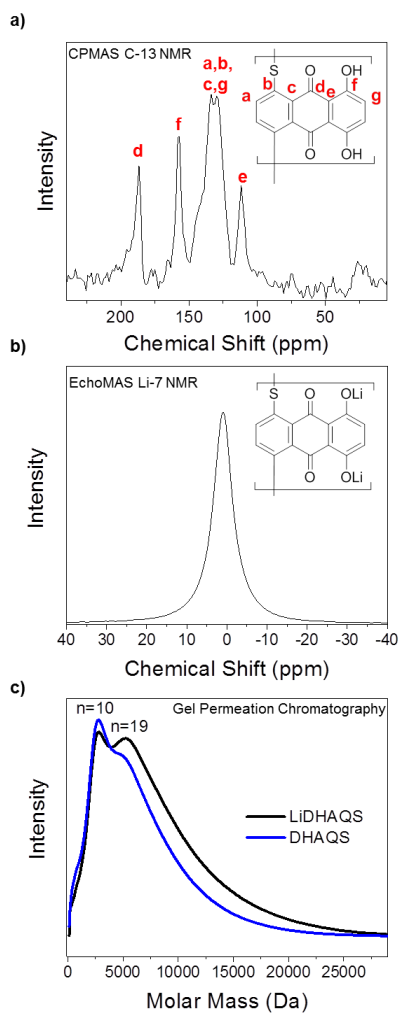


Figure 2.2. a) CPMAS ^{13}C NMR of DHAQS, b) EchoMAS ^7Li NMR of LiDHAQS, c) GPC analysis of both polymers (n = number of monomers in chain)

Table 2.2. Comparison of ^{13}C NMR of DHAQS and DHAQ

Carbon	Chemical Shift in DHAQS (ppm)	Chemical Shift in DHAQ (ppm) ^[21]
a	120-150 (broad)	134.5
b	120-150 (broad)	127.0
c	120-150 (broad)	133.4
d	186.9	186.9
e	111.7	112.7
f	157.0	157.8
g	120-150 (broad)	129.4

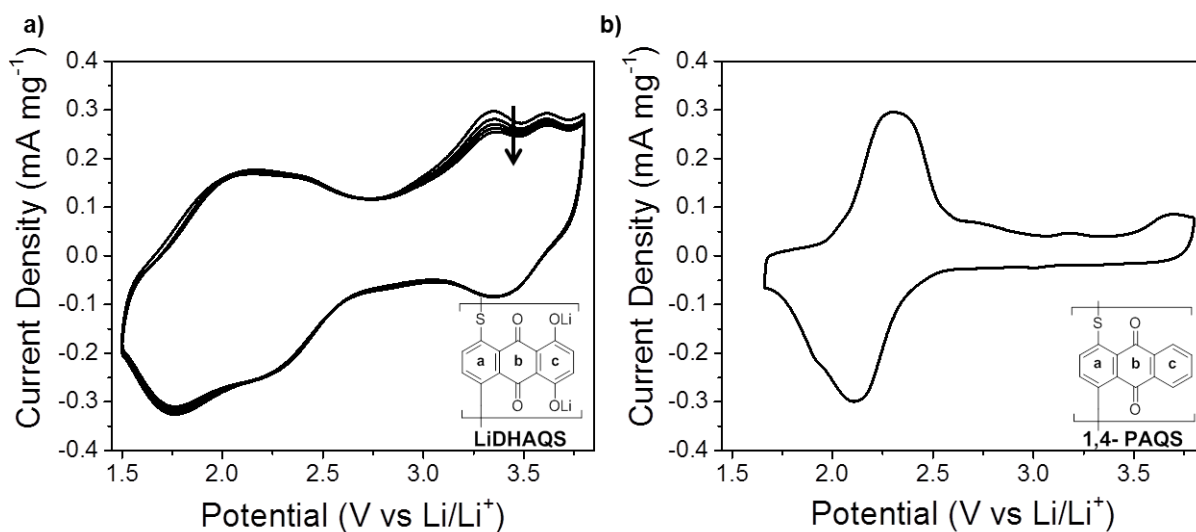


Figure 2.3. a) Cyclic voltammogram of LiDHAQS, b) Cyclic voltammogram of 1,4- PAQS

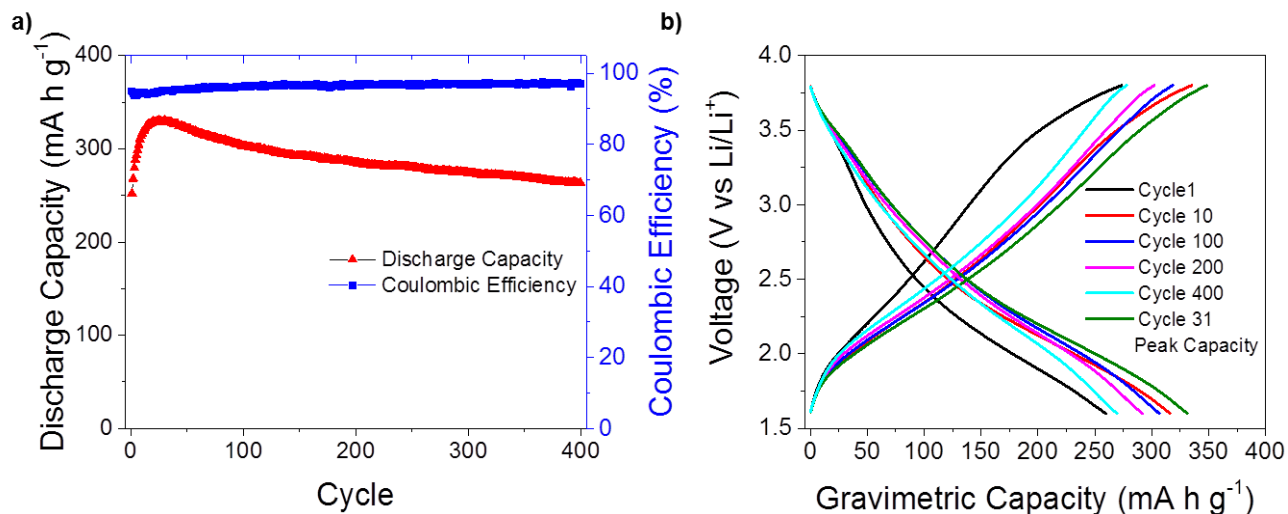


Figure 2.4. a) Galvanostatic charge and discharge of LiDHAQS cathode at 0.5C, b) Charge and discharge curves for various cycles at 0.5C

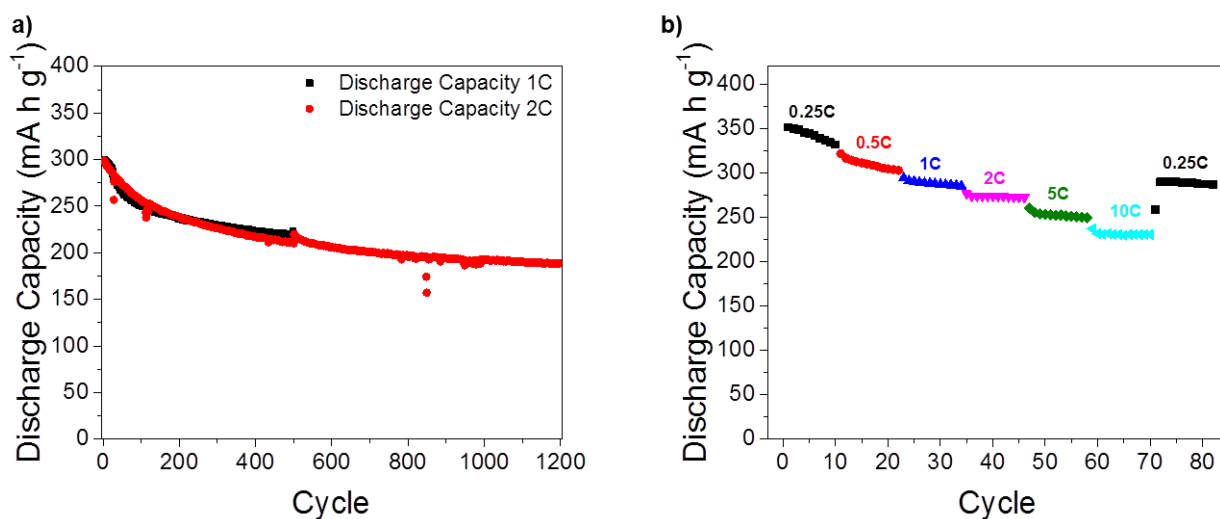
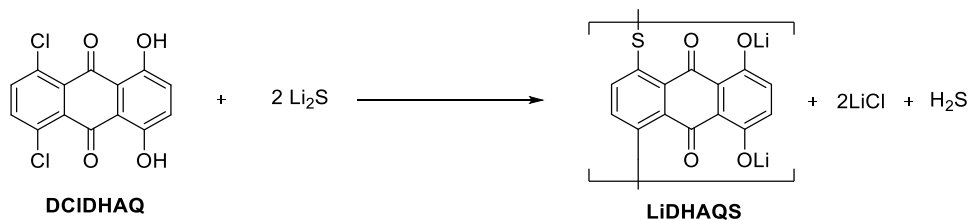
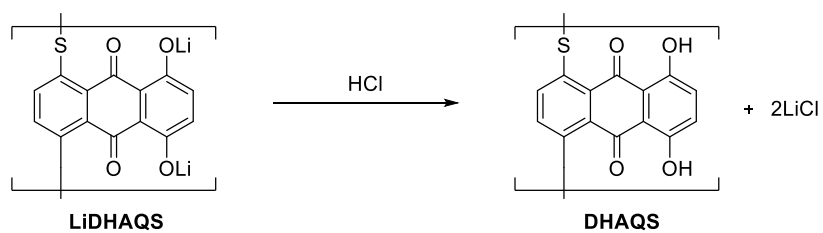


Figure 2.5. a) Long-term cycling of LiDHAQS at 1C and 2C, b) Galvanostatic charge and discharge of LiDHAQS cathode at various rates



Scheme 2.1. Synthesis of LiDHAQS from DCIDHAQ



Scheme 2.2. Conversion of LiDHAQS to DHAQS

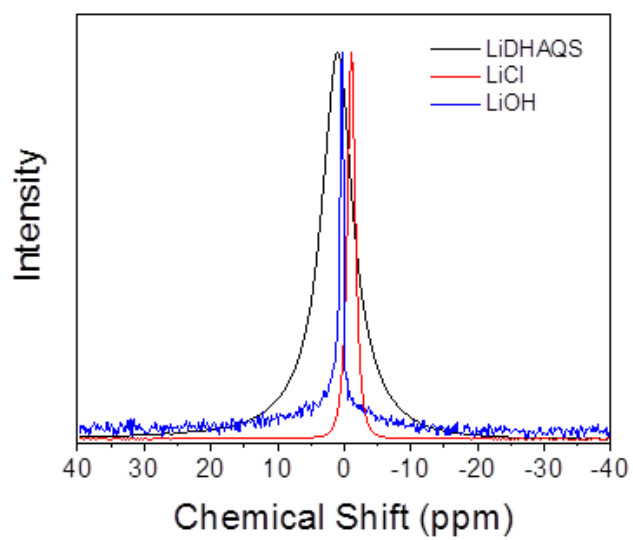
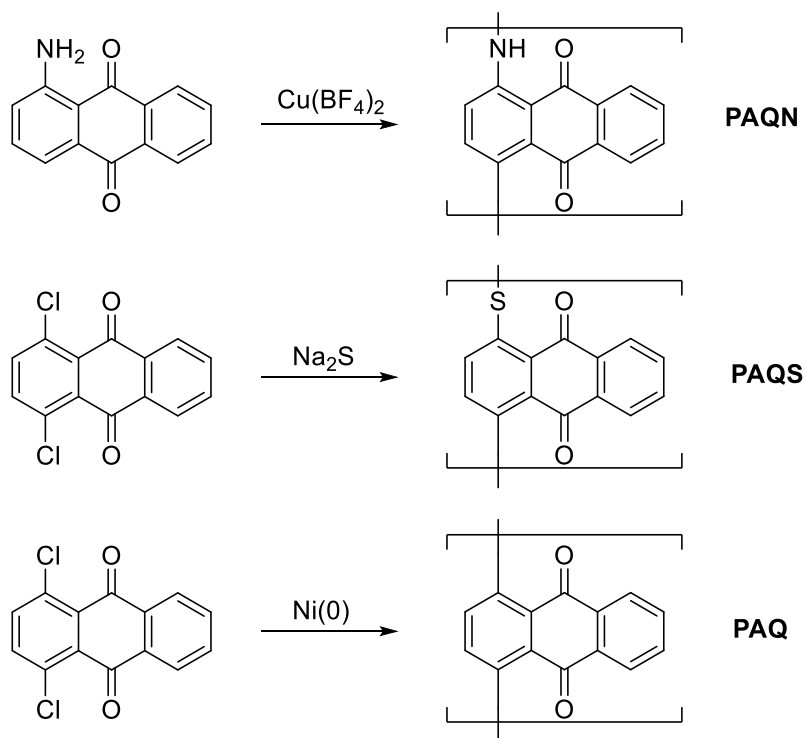


Figure 2.6. Normalized ^7Li NMR of LiDHAQS, LiCl, and LiOH



Scheme 2.3. Polymers studied in this report polyamino anthraquinone (PAQN) polyphenylanthraquinonyl sulfide (PAQS) and polyanthraquinone

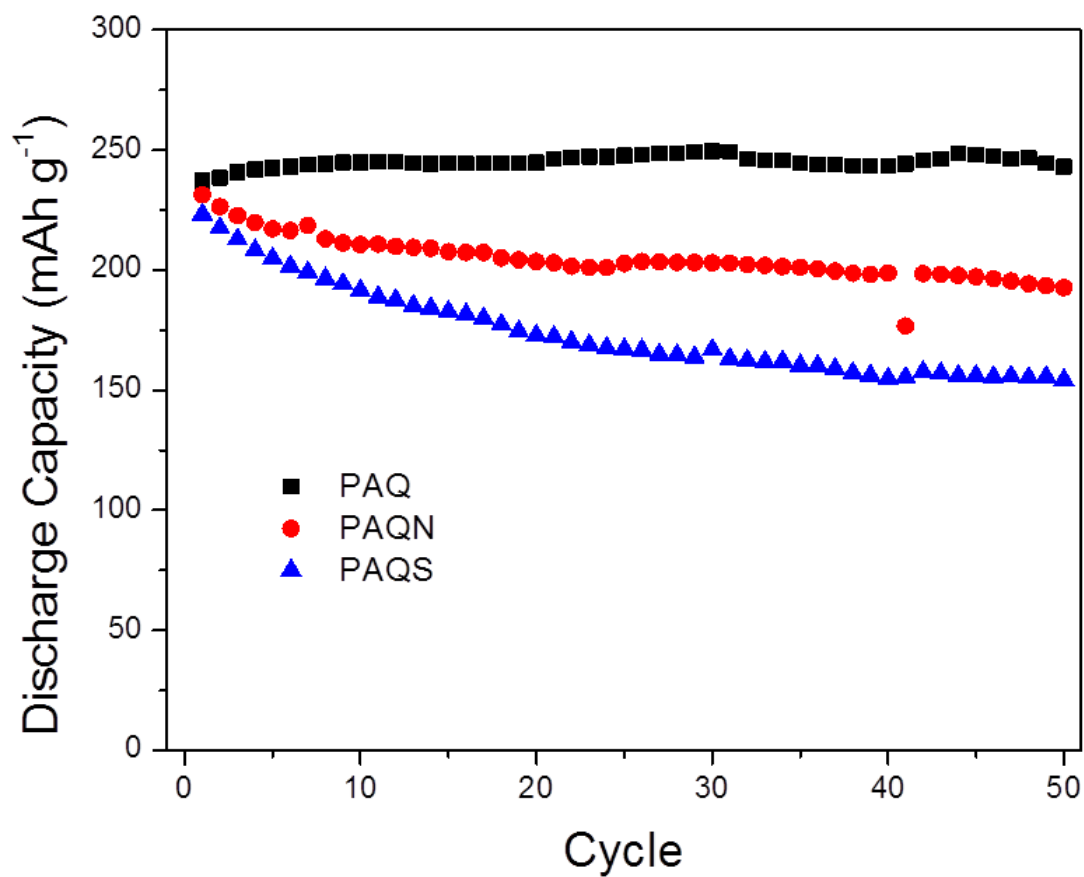


Figure 2.7. Galvanostatic cycling of PAQ, PAQN, and PAQS at 0.5C between 1.6 and 3.0 V vs Li/Li⁺

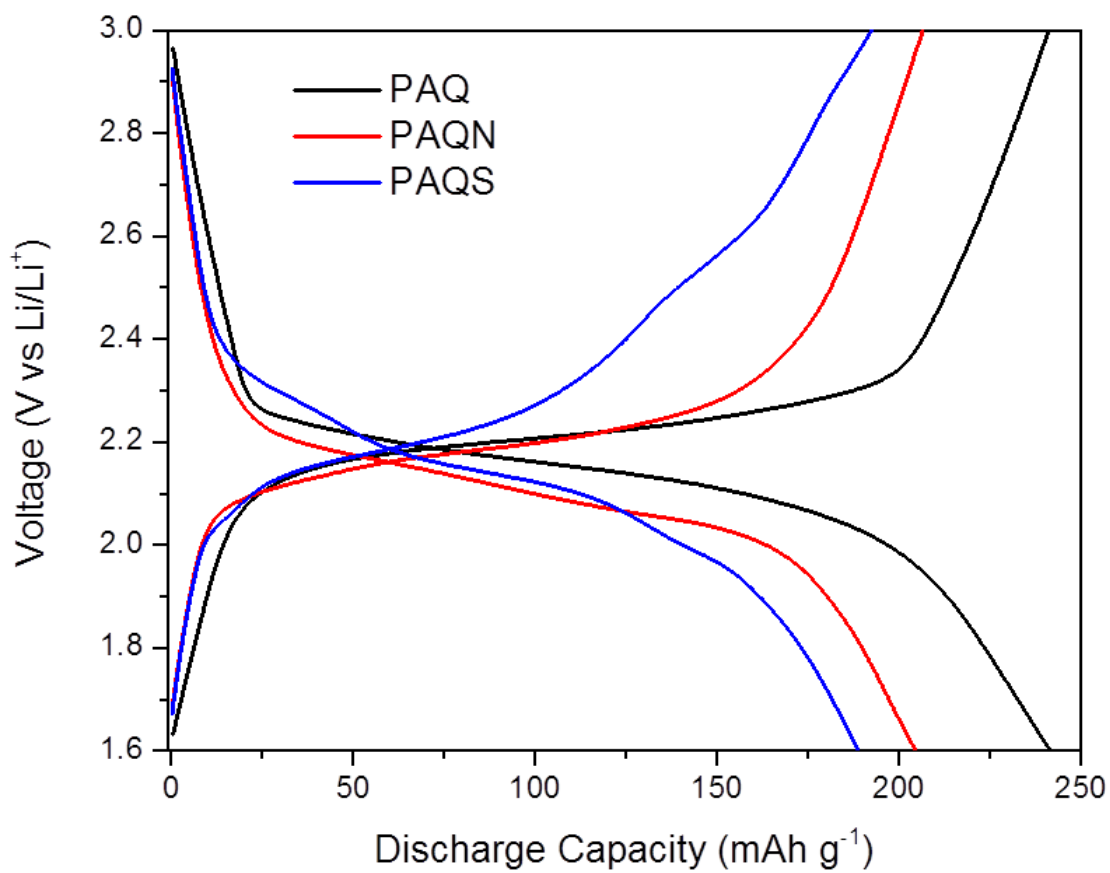


Figure 2.8. Charge and Discharge Curves of PAQ, PAQN, and PAQS at 0.5C between 1.6 and 3.0 V vs Li/Li⁺

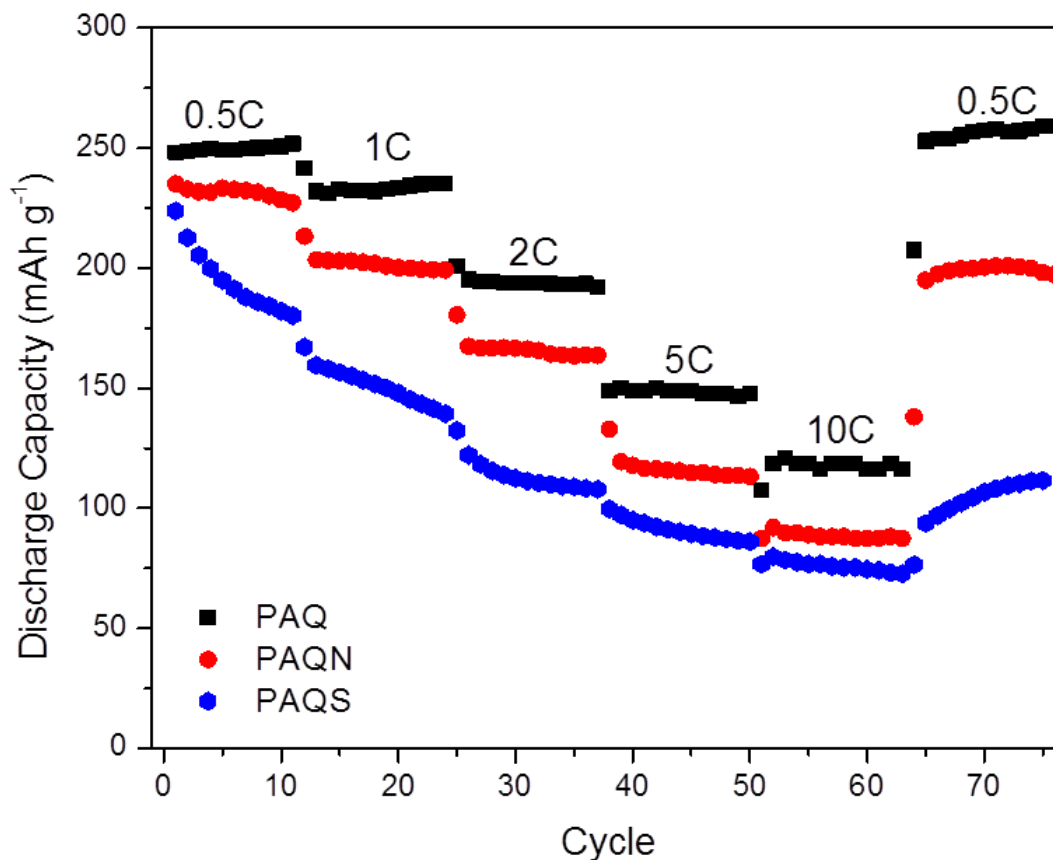


Figure 2.9. Galvanostatic rate studies of PAQ, PAQN, and PAQS at 0.5C between 1.6 and 3.0 V vs Li/Li⁺

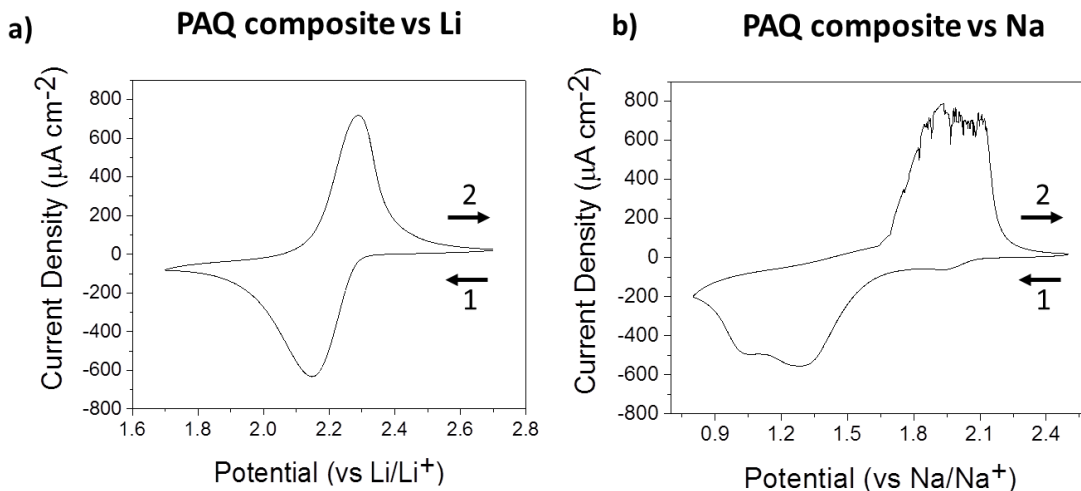


Figure 2.10. Voltammetric studies of PAQ cathode at 1 mV/s in a) LiTFSI system vs Li Counter/Reference and b) NaTFSI system vs Na Counter/Reference

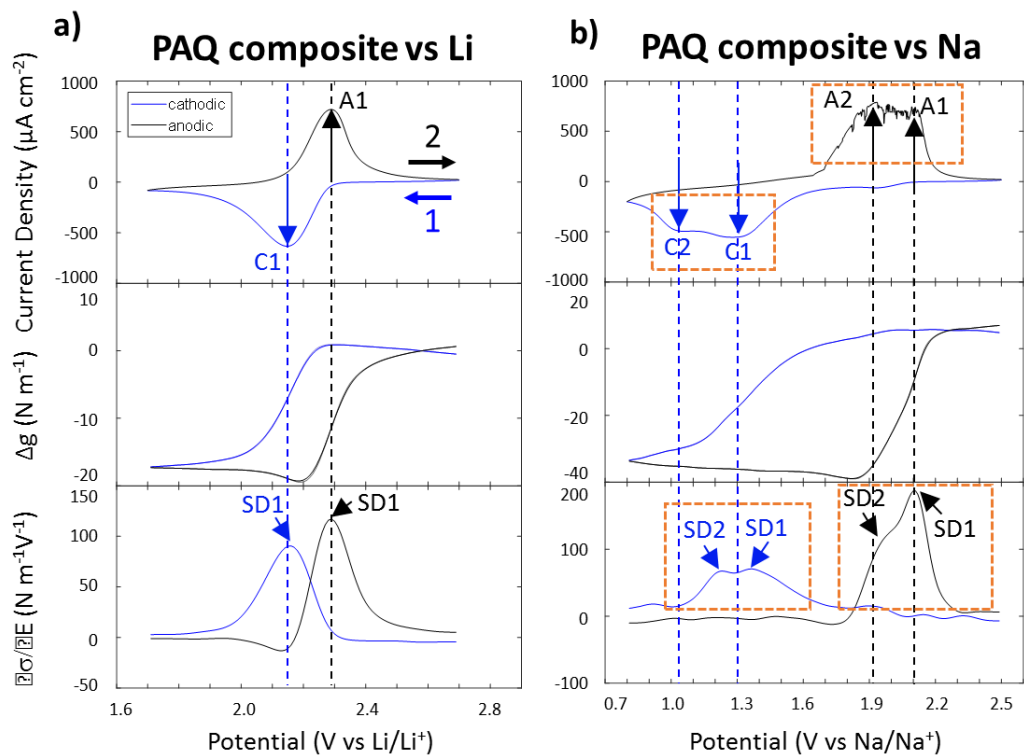


Figure 2.11. Stress studies of PAQ cathode at 1 mV/s in a) LiTFSI system vs Li Counter/Reference and b) NaTFSI system vs Na Counter/Reference

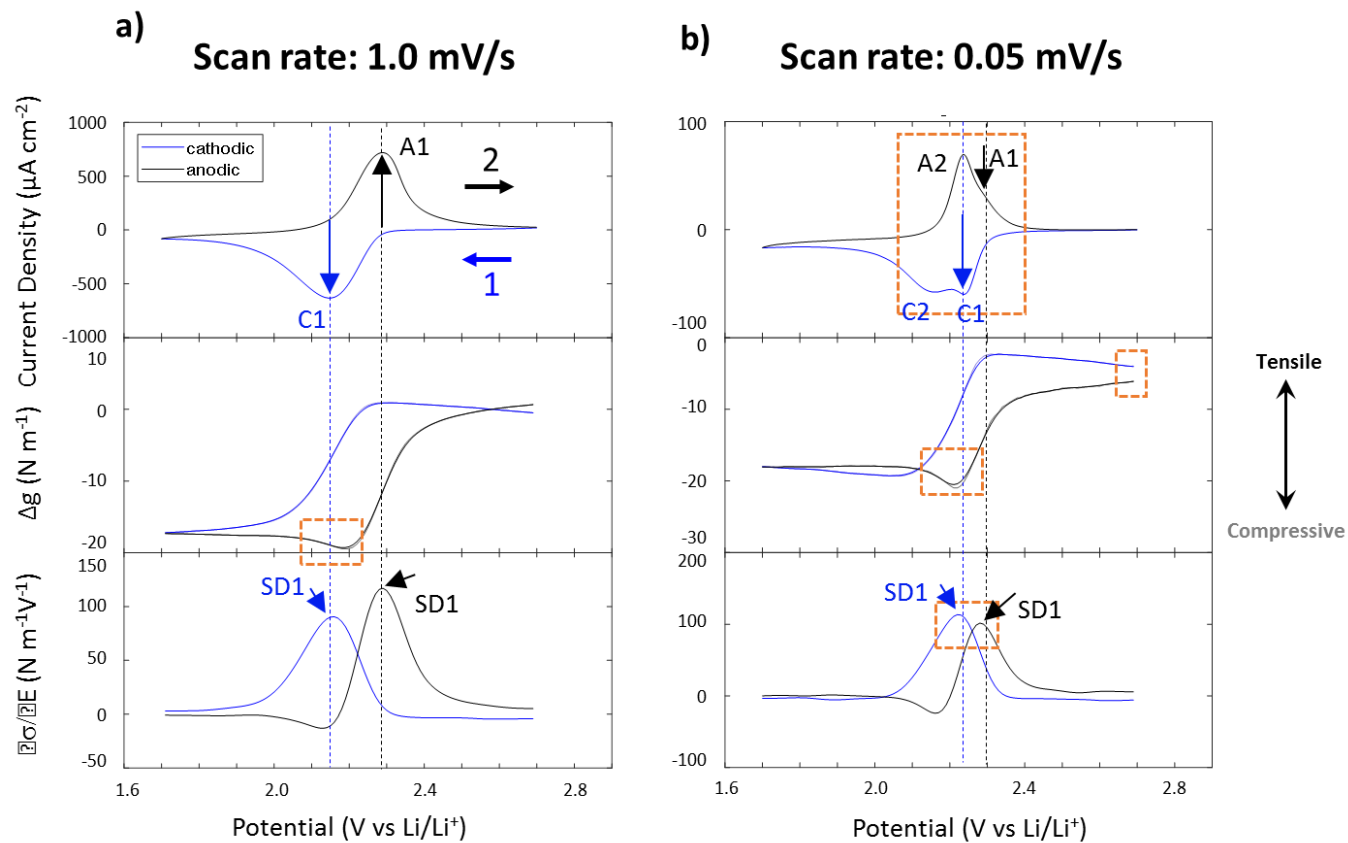


Figure 2.12. Stress studies of PAQ cathode a in LiTFSI system vs Li Counter/Reference at 1 mV/s and 0.05 mV/s

Chapter 3

Solid-Liquid Lithium Electrolyte Nanocomposites Derived From Porous Molecular Cages

3.1 Abstract

We demonstrate that solid-liquid nanocomposites derived from porous organic cages are effective lithium ion electrolytes at room temperature. A solid-liquid electrolyte nanocomposite (SLEN) fabricated from a LiTFSI/DME electrolyte system and a porous organic cage exhibits ionic conductivity on the order of $1 \times 10^{-3} \text{ S cm}^{-1}$. With an experimentally measured activation barrier of 0.16 eV, this composite is characterized as a superionic conductor. Furthermore, the SLEN displays excellent oxidative stability up to 4.7 V vs. Li/Li⁺. This simple three-component system enables the rational design of electrolytes from tunable discrete molecular architectures.

3.2 Introduction

The development of lithium ion batteries (LIBs) represents one of the most significant technological advancements for energy storage in recent history due to their high energy density and operating voltage⁵². Although LIBs hold tremendous promise and are used widely in handheld devices, they typically suffer from substantial practical limitations that restrict their widespread implementation in larger devices^{9b, 52a, 53}. In a practical sense, many of these limitations arise from the use of conventional liquid electrolytes as charge carriers^{5, 53-54}. While liquid electrolytes provide high conductivity and fast ion mobility, both anodic and cathodic instability can lead to cell degradation. Concurrently, liquid electrolytes pose the threat of dendritic lithium deposition at the anode - a phenomenon that inevitably leads to short-circuiting and prevents the use of the Li metal anode^{16b, 55}. Consequently, a major research thrust in the field of LIBs involves fabricating

solid-state electrolytes that transport lithium ions, yet eliminate the issues involved with using liquid electrolytes.

Materials comprised of lithium salts dissolved in organic polymers such as poly(ethylene oxide) were among the first solid-state electrolyte materials studied⁵⁶. Despite extensive research efforts for this class of materials, performance remains low, with lithium ion conductivities typically less than $1 \times 10^{-4} \text{ S cm}^{-1}$ at room temperature. Other inorganic ceramic materials have demonstrated exceptional conductivities, yet are often unstable at both the anode and cathode with few exceptions^{54, 57}. These complications severely limit application of solid-state electrolytes, since electrolytes for LIBs must retain high conductivities (at least $1 \times 10^{-3} \text{ S cm}^{-1}$) while remaining stable at both electrodes.

Recently, researchers have demonstrated the use of porous materials as charge carriers for solid-state electrolytes. Porous materials including MOFs⁵⁸, COFs⁵⁹, polymer networks⁶⁰ and molecular solids⁶¹ have all been utilized as a medium to conduct lithium ions at room temperature, with conductivities as high as $3.1 \times 10^{-4} \text{ S cm}^{-1}$ ⁵⁸. A relatively new class of materials, porous organic cages (POCs), have generated increasing interest due to their unique pore topologies⁶², host-guest chemistry⁶³, and solution processability⁶⁴. While only one report has shown proton conductance within porous molecular cage solids⁶⁵, there have been no reports investigating lithium electrolyte activity within such materials. Toward this end, we hypothesized that nanocomposites constructed from an electrolyte solution and the open pore structure of a porous organic cage are efficient lithium electrolytes at room temperature. Herein, we test this hypothesis by formulating and characterizing solid-liquid electrolyte nanocomposites (SLENs) derived from a POC previously synthesized by our group. In this contribution we describe a SLEN system derived from a porous organic cage (POC) that exhibits high ionic conductivity at room temperature ($1 \times 10^{-3} \text{ S cm}^{-1}$), a

low activation energy barrier for conduction (0.16 eV), and high oxidative stability (up to 4.7 V vs Li/Li⁺). We anticipate that results from this study will lead to a search for novel organic ion conducting composites with tunable environments that are precise in molecular design.

3.3 Results and Discussion

A solid-liquid electrolyte nanocomposite was formulated from a POC previously synthesized by our group, Td_A,⁶⁶ (**Figure 3.1**) resulting in a white, free-flowing powder (**Figure 3.2**). Briefly, 35 mg of Td_A powder prepared by a literature method^{66b} was added as a suspension to a 1M bis(trifluoromethane)sulfonamide lithium salt (LiTFSI) solution of 1,2-dimethoxyethane (DME) and stirred overnight in a argon-filled glove box (**3.2**). The mixture was then centrifuged, the supernatant was removed, and the collected solid was dried under vacuum at 60 °C for 24 hours. The composition of the resulting SLEN material was examined via FTIR spectroscopy. **Figure 3.3a** displays the fingerprint region of the FTIR spectra for samples of a 1M LiTFSI DME solution, Td_A, and SLEN. The spectra show that the SLEN has a high molar concentration of LiTFSI, resembling the 1 M LiTFSI soaking solution used for fabrication. Characteristic peaks of Td_A are observable at ca. 1520 cm⁻¹ and ca. 920 cm⁻¹, indicating that the material is indeed a mixture of Td_A, DME, and solubilized LiTFSI. In addition to FTIR, the thermal stability of the SLEN was investigated using thermal gravimetric analysis (TGA). As shown in **Figure 3.3b**, the material exhibits a gradual decrease of mass, likely associated with the loss of DME. This type of TGA behavior has been observed in MOF-based solid lithium electrolyte materials⁵⁸. The sharp decrease in mass (ca. 40 %) at 350 °C is attributed to decomposition of LiTFSI in the composite.

To gain further insight into the environment of the Li⁺ ions in the nanocomposite, we probed the SLEN using solid state magic angle spinning (SSMAS) ⁷Li NMR. As shown in **Figure 3.3c**, the SLEN exhibits a narrower linewidth, which is attributed to the more liquid-like chemical

environment of the Li^+ allowing more motion and a larger degree of dynamic averaging⁶⁷. The spectra of the SLEN exhibits additional side peaks at -1.9 ppm and -2.1 ppm which we attribute to additional chemical environments made possible by association with Td_A .

Imaging the SLEN via scanning electron microscopy (**Figure 3.3d**) reveals the morphological characteristics of the material. The surface of SLEN particles appear rough, resembling the rapidly precipitated solid of Td_A as shown previously^{66b}. Energy dispersive spectroscopy (EDS) of the material exhibits the presence of C, N, O, F, and S atoms attributed to Td_A , DME, and LiTFSI, along with Au and Pd atoms due to sputtercoating with Au/Pd. EDS mapping (**Figure 3.4**) indicates the material is not phase separated on length-scales greater than the mapping's resolution.

Figure 3.3e displays the ^1H NMR spectrum of the SLEN upon dissolution in $\text{THF-}d_8$. The ^1H NMR spectrum of pure Td_A in $\text{THF-}d_8$ (**Figure 3.5**) confirms that the peaks at δ 7.49, 7.04, 4.16, 2.44, and 1.13 ppm correspond to Td_A . The peaks at δ 3.47 and 3.25 ppm are from DME present in the material⁶⁸. We attribute the peak at δ 3.08 ppm to hydration of the lithium salt within the composite. From the ratio of integrals the molar ratio of Td_A :DME in the composite is determined to be 1:11. Combining the NMR analysis with elemental analysis (**Table 3.1**), the molar ratio of components in the composite is approximately Td_A :DME:LiTFSI 1:11:8.

The molar ratio of 11:8 DME:LiTFSI (mol:mol) is analogous in composition to a 7 M solution and has 2.75 DME coordination sites per Li^+ . To our knowledge there are no extensive studies of the coordination environment of LiTFSI-DME systems, although coordination studies of LiTFSI-Acetonitrile (ACN)⁶⁹ systems and applied studies of concentrated dioxolane/DME-LiTFSI systems have been reported⁷⁰. In a LiTFSI-ACN system, coordination numbers of 2.88 and 2.65 are observed for 1:5 and 1:4 LiTFSI:ACN solutions respectively⁶⁹. Additionally in 1:1 dioxolane:DME (v:v) solvent, solubility up to 7 M has been observed⁷⁰. Despite reports suggesting

formation of a 7 M solution of LiTFSI in DME should be possible, our own attempts at forming such a solution resulted only in a saturated solution with persisting undissolved salt. As we observed no phase separated LiTFSI salt throughout our composite, we performed solid state ^{13}C NMR studies to understand the composition of matter present in the SLEN.

Figure 3.6 displays the solid state ^{13}C NMR studies of the SLEN and various reference systems. A solid state ^{13}C NMR DPMAS spectrum of LiTFSI salt taken on a 300 MHz spectrometer (green) exhibits a single broad peak at 119.8 ppm. A solution ^{13}C spectrum of 11:8 molar mixture of DME:LiTFSI (saturated solution, *vide supra*) taken on a 500 MHz spectrometer is displayed in orange. The spectrum exhibits two peaks (59.1 ppm and 71.0 ppm) which correspond to DME and a quartet centered at 120.5 ppm with a $^1J_{\text{C-F}} = 321$ Hz corresponding to LiTFSI in agreement with literature⁷¹. A ^{13}C NMR CPMAS solid state spectrum of Td_A taken on a 300 MHz spectrometer is displayed in black. The observed peaks show good agreement with those reported in solution^{66b} although resolution of all the aromatic peaks is obscured by the large line width. A ^{13}C NMR DPMAS solid state spectrum of the SLEN taken on a 300 MHz spectrometer is displayed in blue. By comparison to our spectrum for Td_A, we assign the peaks at δ 13.3, 22.4, 32.9, 88.3, 120.3, 126.5, 130.2, and 140.1 ppm to Td_A. We assign the peaks at δ 57.2 and 69.0 ppm to DME and note that they exhibit a significant upfield shift as compared to those in solution. Two additional peaks are present in the SLEN spectra: one at δ 112.6 and one at 116.7 ppm. We considered two possible assignments for these peaks. First, the two peaks could be part of a quartet with the remaining signals obscured by the signal for Td_A. We discount this possibility based on the separation of the two signals which, if coupled, would have $J=307$ Hz which is significantly different than that observed for LiTFSI. Based on chemical shift, we assign these two peaks instead as two singlets from different chemical environments of LiTFSI. We note both peaks are upfield

to the peak observed in the solid LiTFSI sample. In the SLEN the peaks for LiTFSI and DME both appear more upfield than the corresponding peaks in the 11:8 DME:LiTFSI sample or the solid LiTFSI sample. We attribute this chemical shift difference to interaction between each component and the cage.

To investigate the utility of the SLEN as a solid-state lithium electrolyte, electrochemical impedance spectroscopy (EIS) was performed. **Figure 3.7a** displays the electrochemical impedance spectroscopy (EIS) of the SLEN at various temperatures. In typical EIS measurements of ionically conducting solids, the complex impedance plot exhibits a half circle followed by a sloped line, with the diameter of the half circle corresponding to bulk resistance⁷². In the frequency range used here, only a sloped line is observed, except at lower temperatures (black). The same phenomenon has been observed in gel-polymer electrolytes⁷³, and is attributed to the liquid-like environment of the charge carriers, which allows fast dielectric relaxation and prevents dielectric capacitance throughout the material⁷⁴. The resistance is derived from the intercept of the line with the real axis (Z'). At room temperature, the measured conductivity was $1.0 \pm 0.1 \times 10^{-3} \text{ S cm}^{-1}$ for the SLEN material. To our knowledge, this conductivity exceeds that of known MOF ($3.1 \times 10^{-4} \text{ S cm}^{-1}$)⁵⁸, COF ($2.6 \times 10^{-4} \text{ S cm}^{-1}$)^{59a}, and porous organic ($1.0 \times 10^{-4} \text{ S cm}^{-1}$)⁷⁵ based SLENs.

Figure 3.7b displays the Arrhenius plot of the temperature dependent conductivity of the SLEN. The material exhibits linear Arrhenius-like behavior over the temperature range probed (-10 to 35 °C). From the slope of the plot, the activation energy of conduction was determined to be 16 kJ mol⁻¹ (0.16 eV). This exceptionally low barrier is consistent with the SLEN being a superionic conductor⁷⁶.

We note that reliable impedance data could not be obtained for temperatures higher than 40 °C due to material instability, as evidenced by TGA of the SLEN material. The thermal instability of

this composite is a significant hindrance to its practical application. Future studies will seek to address this by investigating other compositions of matter that eliminate the solvent component of the composite by covalently attaching coordination sites on the cage framework.

It is also important to note that applying the same electrolyte preparation to the synthetic precursor of the cage (P_{carb} , **Figure 3.8**) results in significantly higher resistance. Taken together, the unique salt environments enabled by the SLEN as observed by NMR, the increased conductivity seen in the cage composite as compared to the precursor composite, and the thermal instability suggest that both the cage and trapped solvent contribute to the conduction in the composite. The exact role and contribution of each component will be the subject of future work.

Figure 3.9a displays a linear sweep voltammogram of a Pt/SLEN/Li cell. The voltammogram exhibits no significant oxidative current in excess of 4.7 V vs Li/Li⁺ demonstrating excellent oxidative stability of the SLEN. We attribute the oxidative stability of the SLEN to the ratio of DME to LiTFSI (11:8) present as high concentration of salt can prevent oxidative decomposition⁷⁷.

Figure 3.9b displays cycles 28-33 of cyclic voltammetry run on a Cu/SLEN/Li cell. These cycles are the point at which the electrochemistry stabilizes. Initial cycles (**Figure 3.10**) as well as tabulated coulombic efficiencies (**Table 3.2**) can be found in the supporting information.

The cell exhibits two sets of redox pairs. The first, with a reductive wave at 0.6 V and oxidative wave at 1.0 V, is assigned to the underpotential deposition and stripping of Li on copper, in analogy to the behavior seen on Ni.⁷⁸ We assign the redox couple at more negative potentials to the bulk deposition and stripping of Li on the substrate.

In initial cycles of the cell, the bulk deposition and stripping exhibit poor coulombic efficiency (**Table 3.2**), and the deposition peak gradually shifts from normal linear behavior to the diffusive regime exhibited in figure 5b. Coulombic efficiencies increase with cycling before stabilizing at

>98% at cycle 23. Current densities are variable between cycles but stabilize at cycle 28. We note that the current densities for the plating and stripping reactions are lower than those seen for ceramic solid electrolytes including β -Li₃PS₄, which has a ionic conductivity lower than the SLEN (ca. 10^{-4} S cm⁻²)⁷⁹. Literature reports often utilize faster sweep rates than that used in this experiment (ca. 250 μ V s⁻¹), which results in larger current densities^{55, 76b, 79-80}. The SLEN does not reversibly deposit Li⁺ at higher scan rates, a phenomenon we attribute to its low concentration of Li⁺. Additionally, we believe the low Li⁺ concentration plays a role in the diffusive behavior observed in later cycles, as poor stripping efficiencies can create depletion layers in the low Li⁺ concentration material.

3.4 Conclusion

In conclusion, we have fabricated a SLEN system utilizing a porous molecular cage and LiTFSI-DME electrolyte solution. The SLEN exhibits exceptional room temperature conductivity of 1×10^{-3} S cm⁻¹ with a low activation energy of 16 kJ mol⁻¹. Cyclic voltammetry demonstrates the excellent oxidative stability of the composite up to 4.7 V as well as the anodic stability upon cycling. Materials characterization indicates that the material presents as a solid, and enables highly coordinated environment of DME and LiTFSI which contribute to its excellent stability. The exceptional electrolyte properties of this material combined with the novel application of porous cages as functional materials makes future studies of this system of great interest.

3.5 Experimental Methods

3.5.1 General

All air or moisture-sensitive manipulations were performed under an atmosphere of nitrogen using standard Schlenk techniques or in an argon-filled glove box. All metathesis reactions were set up in an argon-filled glove box and run under an inert atmosphere. Reaction vessels were 20

mL I-CHEM vials fitted with PTFE/Silicone septa purchased from VWR International unless specified otherwise.

3.5.2 Materials

Unless otherwise stated, all starting materials and reagents were purchased from Sigma Aldrich and used without further purification. The following compounds were prepared according to literature procedure: 1,3,5-Tris(4-propynylbenzyl)-2,4,6-triethylbenzene (P_{Carb}),¹ Td_A ,¹ molybdenum(IV) propylidyne precatalyst [Mo].^{2,3}

3.5.3 Characterization

3.5.3.1 Solution NMR Spectroscopy

¹H and ¹³C NMR spectra were recorded on a Varian Unity 400 MHz (298 K). All spectra were recorded in chloroform-*d* or tetrahydrofuran-*d*8 unless specified otherwise. Chemical shifts are reported in δ (ppm) referenced on tetramethylsilane (TMS) or residual solvent peaks (CDCl₃: 7.26 for ¹H, 77.16 for ¹³C; THF-*d*8: 1.72 and 3.58 for ¹H). Coupling constants (J) are expressed in Hertz (Hz). Splitting patterns are designated as: s (singlet), d (doublet), t (triplet), or m (multiplet).

3.5.3.2 Solid State ⁷Li MAS NMR Spectroscopy

⁷Li solid-state NMR spectra were obtained in the School of Chemical Sciences (SCS) NMR facility at the University of Illinois at Urbana-Champaign using a Varian VNMRS 750 MHz NMR spectrometer (17.6 T) operating at a resonance frequency of ν_0 (⁷Li) = 291.2 MHz at room temperature. A Varian 4 mm triple-resonance HXY T3 narrow-bore (NB) magic-angle spinning (MAS) probe was used for all experiments at a spinning rate of 15 kHz and two pulse

phase modulation (TPPM) ^1H decoupling. Samples were packed into 4 mm zirconia rotors in a glove box to avoid exposure to moisture.

Experimental lithium chemical shift referencing, pulse calibration and setup were performed using 1M LiCl, which has a chemical shift of 0.00 ppm. Specific ^7Li pulse widths of 6.0 μs and recycle delays of 2 s were used, 168 scans were acquired for the SLEN sample and 40 scans for the LiTFSI sample.

^{13}C solid-state NMR spectra were obtained in the SCS NMR facility using a Varian Unity Inova 300 NMR spectrometer (7.05 T) operating at a resonance frequency of $\nu_0 (^{13}\text{C}) = 75.47$ MHz and $\nu_0 (^7\text{Li}) = 116.6$ MHz at room temperature. A Varian/Chemagnetics 4 mm double-resonance APEX HX magic-angle spinning (MAS) probe was used for all experiments at a spinning rate of 10 kHz and two pulse phase modulation ^1H decoupling. Samples were packed into 4 mm zirconia rotors.

Experimental carbon chemical shift referencing, pulse calibration and cross-polarization condition were performed using powdered hexamethylbenzene (HMB), which has a chemical shift of 17.3 ppm (for the methyl peak) relative to the primary standard, trimethylsilane (TMS), at 0 ppm. For LiTFSI sample 668 scans were used, for SLEN sample 1932 scans were used, and for the Td_A sample 2584 scans were used.

3.5.3.3 Thermogravimetric Analysis

TGA was performed on a TA Instruments Q50 analyzer. Samples were heated to 600 $^\circ\text{C}$ in a platinum crucible at a rate of 10 $^\circ\text{C}/\text{min}$ under a nitrogen atmosphere.

3.5.3.4 SEM and EDS

Characterization of materials was carried out in the Microscopy Suite at the Beckman Institute for Advanced Science and Technology at the University of Illinois at Urbana-Champaign. Prior to imaging, the samples were prepared by mounting on a stub using carbon tape and sputter coated with gold-palladium using a deposition current of 20 mA and a deposition duration of 70 s. The samples were imaged using a FEI Quanta FEG 450 ESEM operating at 10.0 kV at a working distance of 10 mm, accelerating voltage of 10.0 kV, extracting voltage of 5.1 kV, emission current of 10 μ A, probe current set to high, and ultrahigh resolution mode.

3.5.3.5 Fourier transform infrared spectroscopy (FTIR)

Spectra were recorded on a Nicolet Nexus 670 spectrometer with a DRIFTS attachment.

3.5.3.6 Elemental Analysis

C, H, N, Li, and F elemental analyses were carried out in the University of Illinois School of Chemical Sciences Micro-analysis Laboratory

3.5.4 Preparation of SLEN:

In an Ar-filled glovebox, 35 mg of Td_A cage is added to 0.6 mL of a 1M solution of LiTFSI in DME. The resulting mixture is stirred overnight in the glovebox. After stirring, the mixture is transferred to a centrifuge tube with 0.3 mL of DME as a wash. The centrifuge tube is capped and wrapped in Parafilm before being transferred outside of the glovebox and centrifuged at 3300 RPM for 2 minutes. The tube is then transferred back into an Ar-filled glovebox and the supernatant is removed. The centrifuge tube is then capped with a septum and transferred outside the glovebox. The septum is pierced with a needle and quickly transferred into a vacuum oven

where it is dried under vacuum at 60 °C for 24 hrs. (Note: we have observed under higher temperature and pressure we can remove all of the solvent from the composite at the cost of decreased ionic conductivity.) The material is then transferred back into a glovebox where it is pressed by hand (typical pressure between 0.5-0.7 MPa) between 2 stainless steel (SS) disks in a 0.5 in diameter pellet die. We note that high pressured pelletization (>7 MPa) results in decreased conductivity. In experiments where electrodes rather than the stainless steel disks are desired, the pressing is done with Al foils rather than steel disks as they are easier to remove. Additionally while the pellets can be made and manipulated as described, doubling the preparation produces a large and more mechanically robust pellet.

3.5.5 Potentiostatic Electrochemical Impedance Spectroscopy of Cage SLEN

The resulting SS/SLEN/SS pellet is placed in a cell made of a modified Swagelok tube fitting. Potentiostatic electrochemical impedance spectroscopy (PEIS) was conducted using a Biologic (Seyssinet-Pariset France) SP150 potentiostat/galvanostat. PEIS was run between a frequency of 1 MHz and 1Hz at 0 V vs. working electrode and with a perturbation amplitude of 20 mV. Temperature was controlled by protecting the cell and electrochemical leads in a thin plastic layer before submerging in a bath of the appropriate temperature and thermally equilibrating for 1 hr.

The same procedures are used on the synthetic precursor to Td_A (P_{carb}) as a control and the results of the conductivity measurement are shown in figure S6. Its characterization of the resulting composite is listed below.

3.5.6 Potentiostatic Evaluation of Anode Reaction Using Cage SLEN as Electrolyte

The samples were prepared as described above, but Cu or Pt foil was used in place of stainless steel discs. One piece of foil is peeled off the SLEN pellet with a razor blade and replaced with a piece of Li foil. Potentiostatic experiments were performed in a cell made of a modified Swagelok tube fitting inside a glove box. The experiments were conducted by using a CH Instruments (Austin, TX) electrochemical workstation. Cyclic voltammograms for the anode reaction were conducted between -0.4 V and 2.0 V vs. Li/Li⁺ at a scan rate of 0.25 mV s⁻¹ with Cu foil as the working for the evaluation of the Li plating and stripping reactions. For oxidative stability, a Pt working was used and linear sweep voltammetry was run from 2.0 V to 5.0V vs Li/Li⁺ at a scan rate of 0.5 mV s⁻¹.

3.6 Figures and Tables

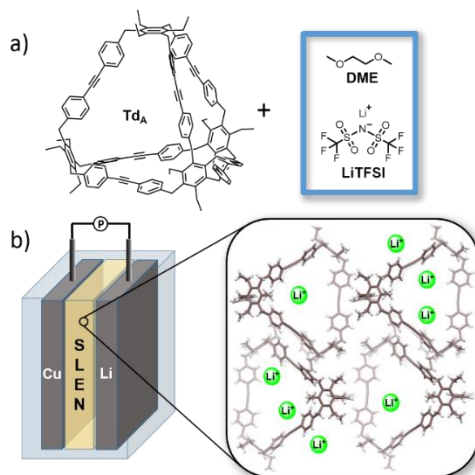


Figure 3.1. Conceptual representation of molecular cage based SLEN a) Molecular structures of SLEN components. b) Visual representation of SLEN half-cell configuration.

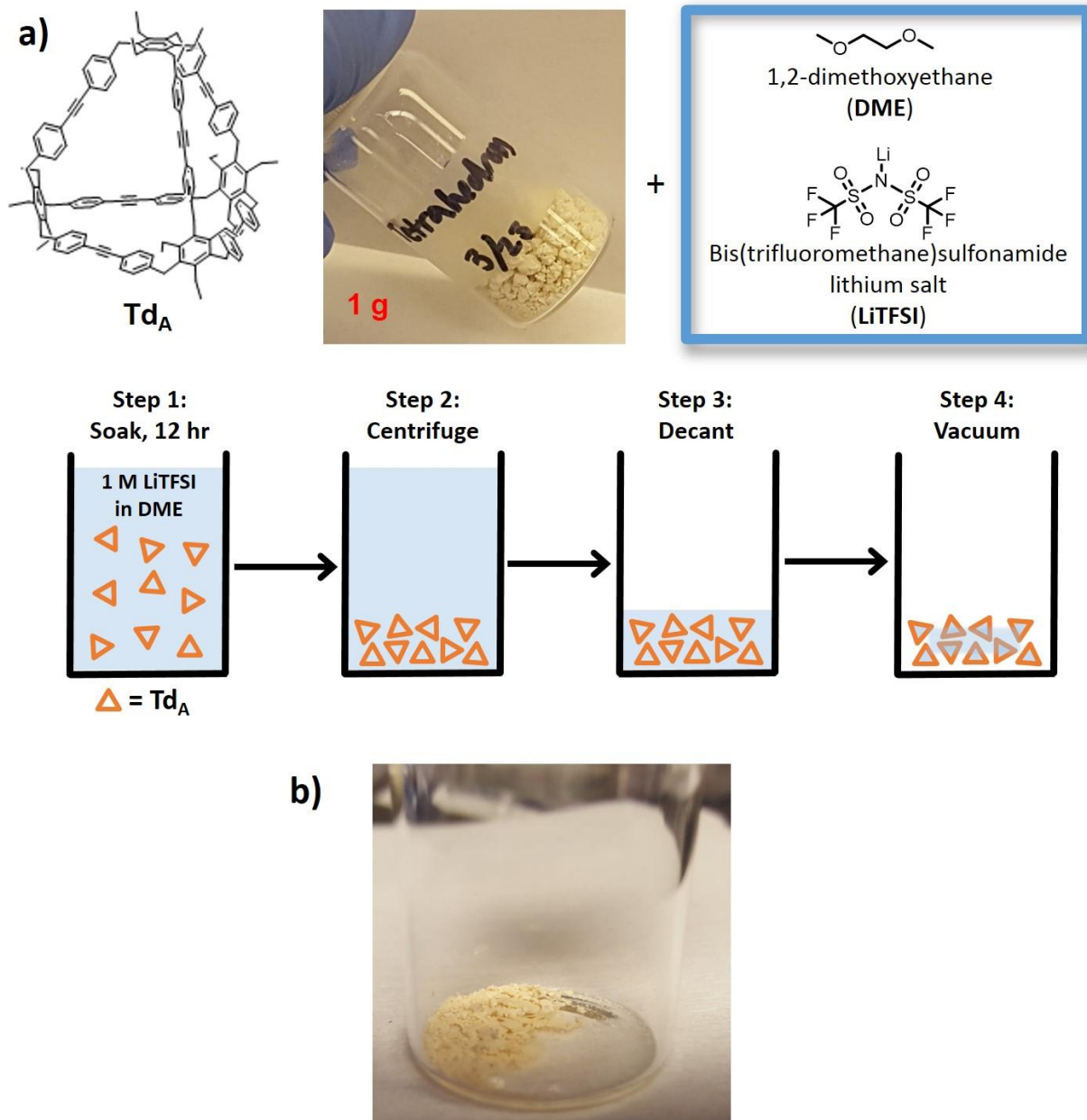


Figure 3.2. a) Preparation of SLEN material b) Image of SLEN in a sealed vial.

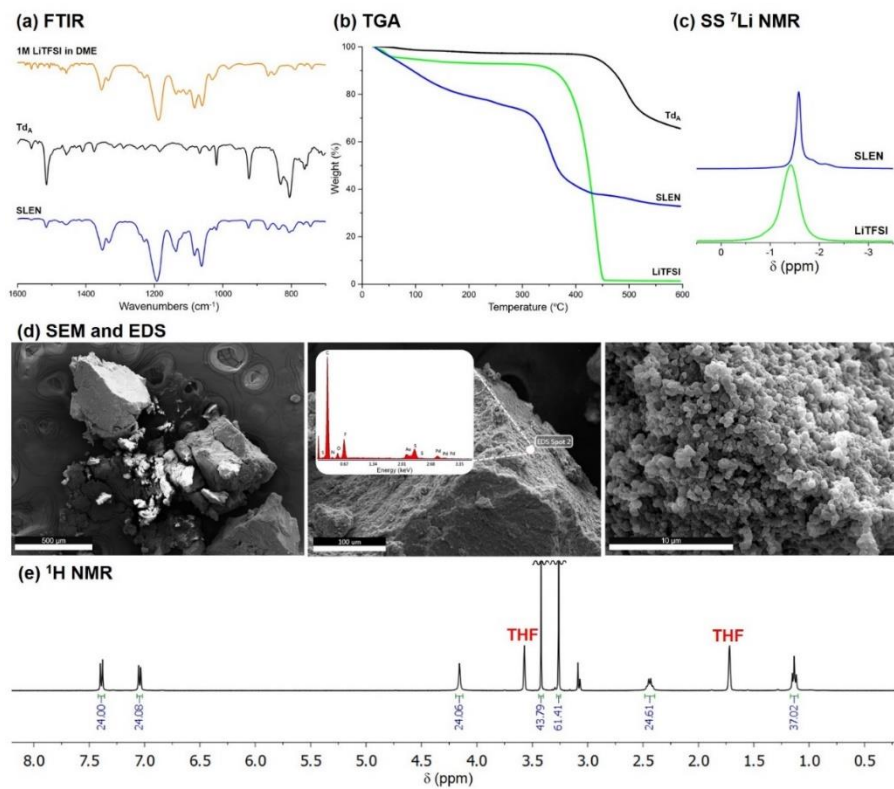


Figure 3.3. Characterization of the SLEN a) FTIR of 1 M LiTFSI DME solution (orange), Td_A (black), and SLEN (blue) b) TGA of LiTFSI (green), Td_A (black), and cage SLEN (blue) c) ⁷Li SS MAS NMR of LiTFSI (green) and SLEN (blue) d) SEM and EDS of SLEN e) ¹H solution NMR of SLEN in THF-d₈.

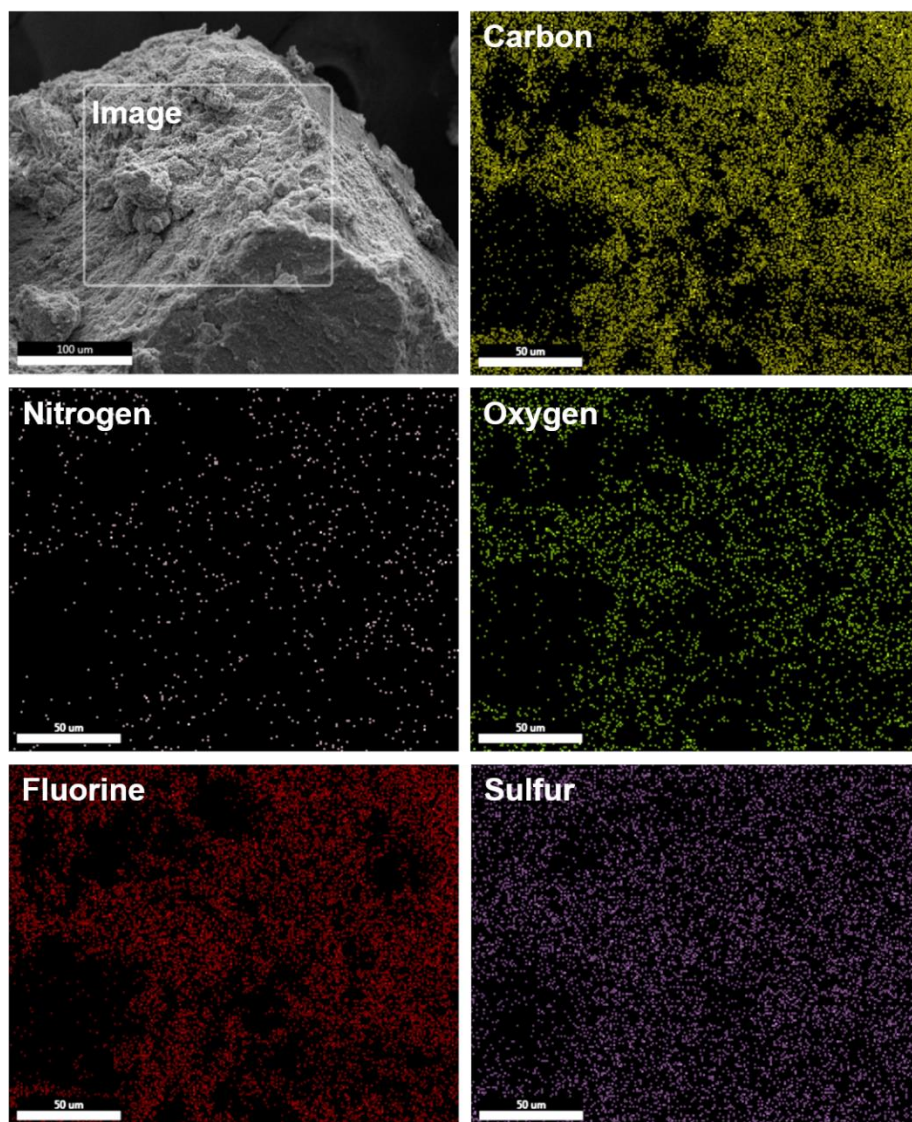
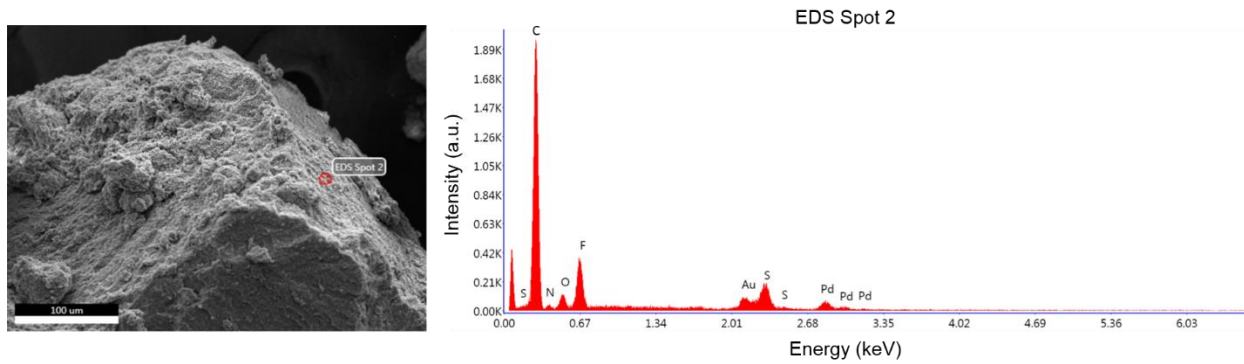


Figure 3.4. EDS and EDS mapping of the SLEN

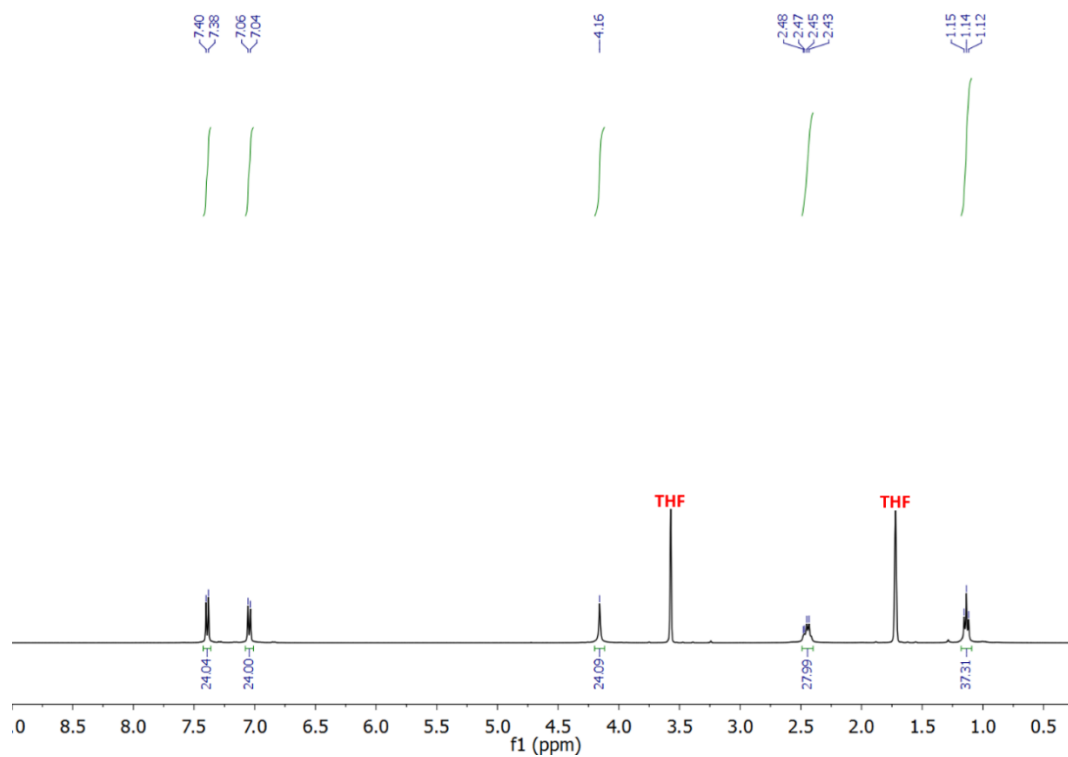


Figure 3.5. ^1H NMR of Td_A (400 MHz, THF-d_8).

Table 3.1. Elemental analysis results of the SLEN

Element	Wt. %
H	4.83
Li	1.01
C	43.95
N	2.30
F	17.59

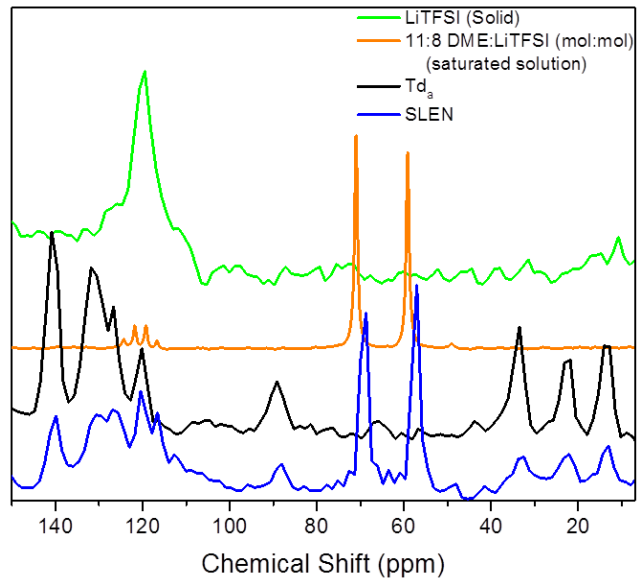


Figure 3.6. Solid state ^{13}C NMR studies of solid LiTFSI (green), saturated 11:8 (mol:mol) mixture of DME and LiTFSI (orange), solid Td_A (black) and SLEN (blue)

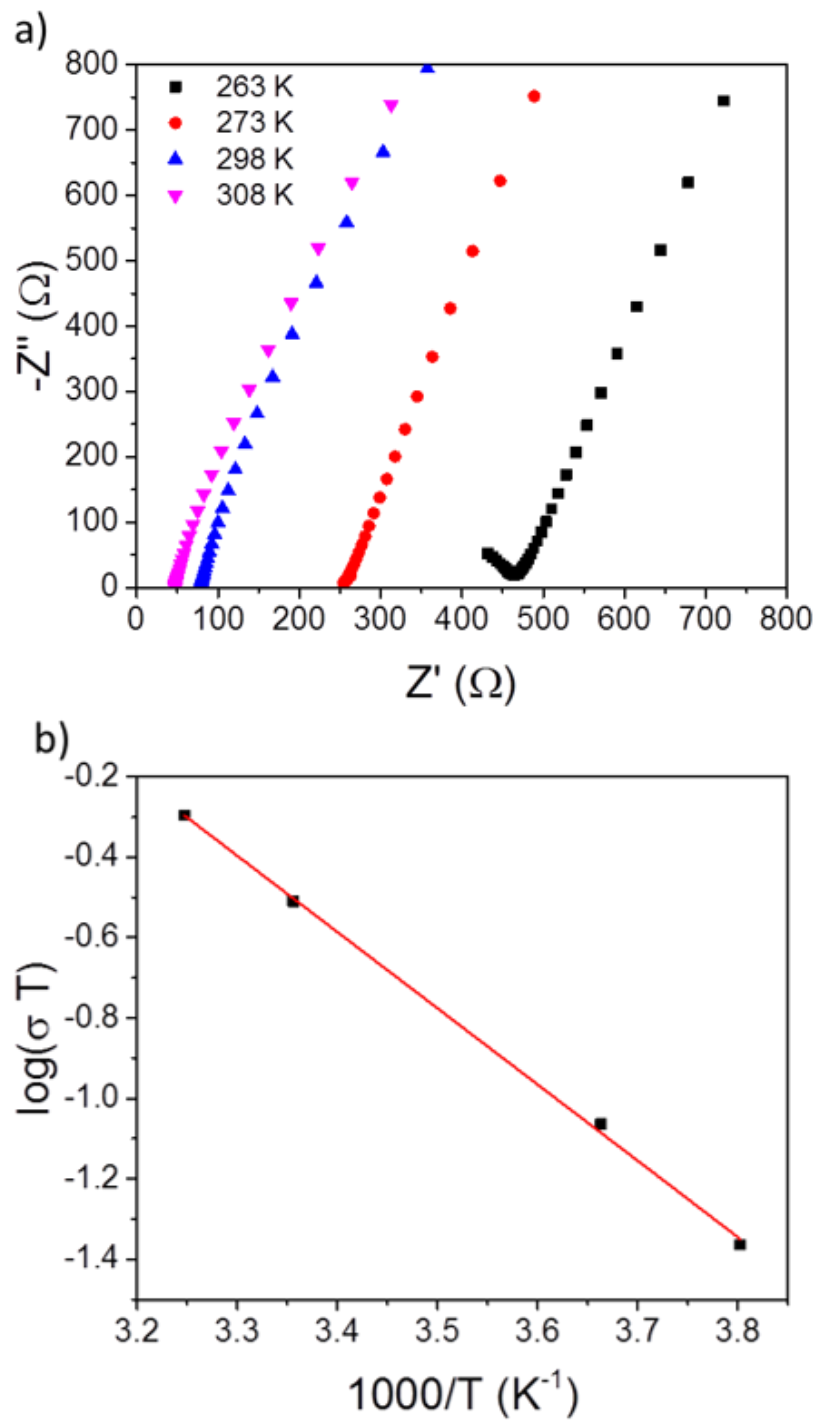


Figure 3.7. Temperature dependent electrochemical impedance spectroscopy (EIS) of the SLEN. a) Complex impedance of the SLEN at various temperatures. b) Arrhenius plot of the temperature dependent EIS

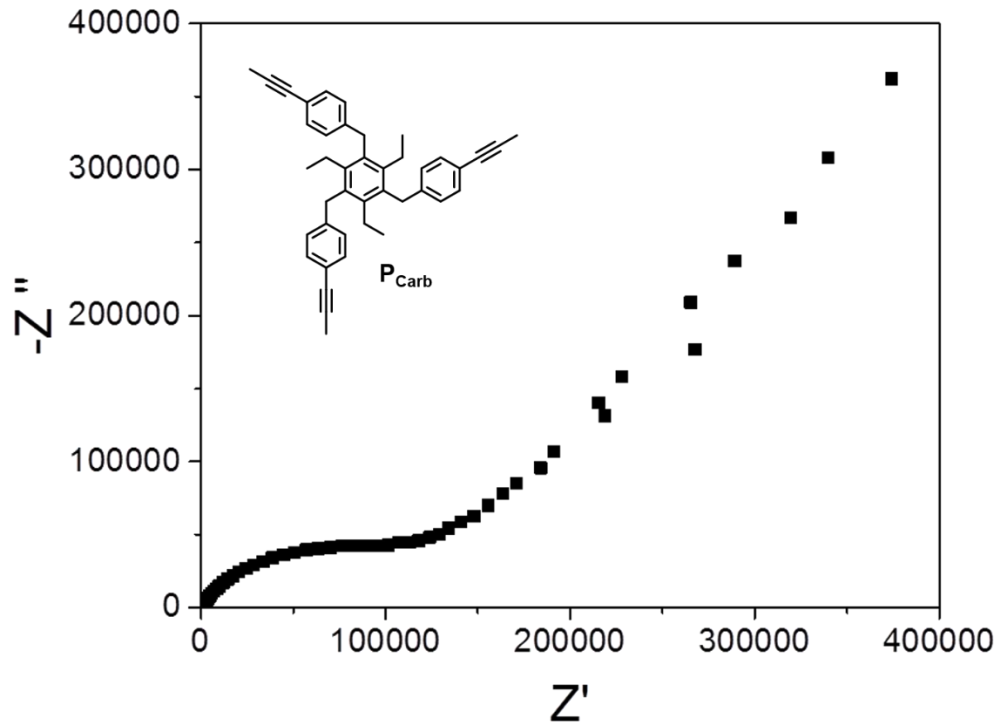


Figure 3.8. Complex impedance spectra of a composite fabricated from P_{Carb} subjected to the same preparatory conditions as the SLEN

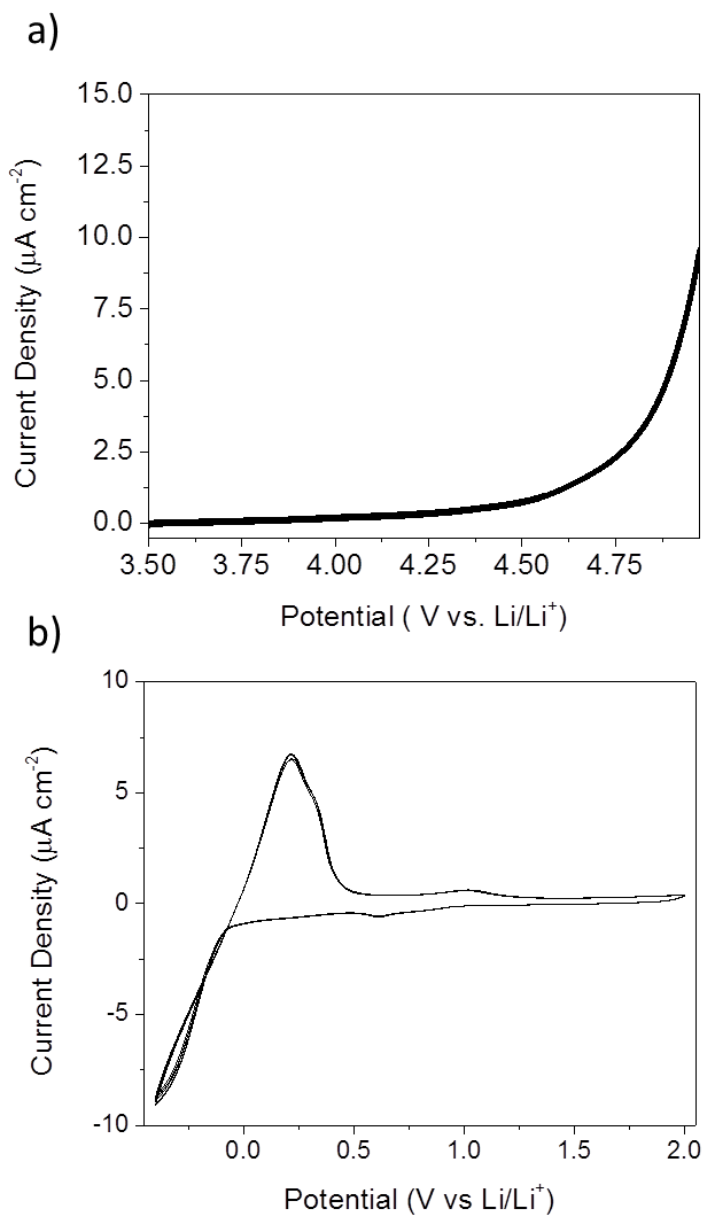


Figure 3.9. Voltammograms of SLEN full cells. a) Linear sweep Voltammogram of Pt/SLEN/Li cell at 500 uV s^{-1} b) Cyclic voltammetry cycles 28-33 of a Cu/SLEN/Li cell cycled between -0.4 V and 2.0 V vs Li/Li^+ at 250 uV s^{-1}

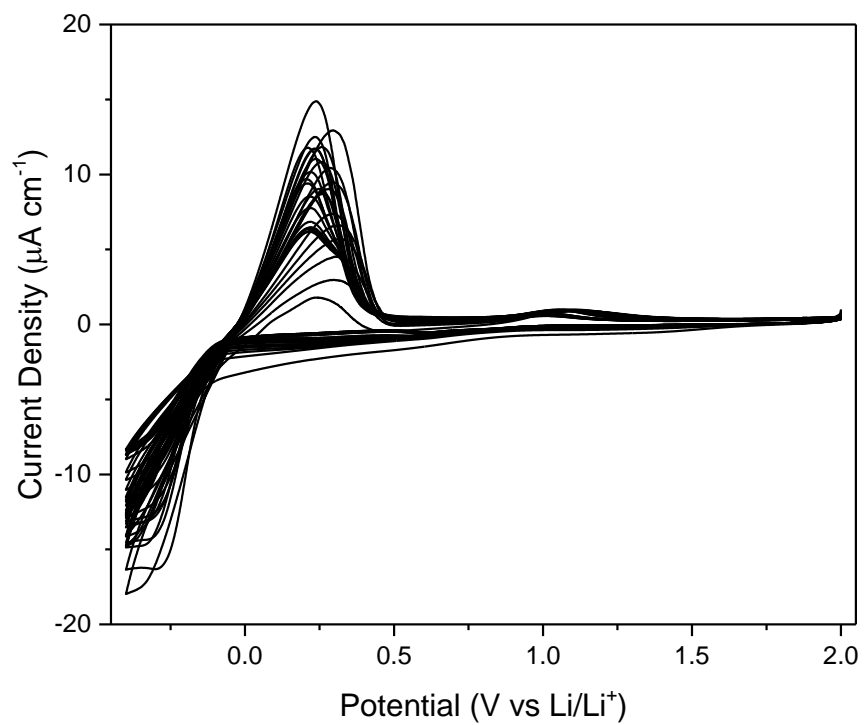


Figure 3.10. Cyclic voltammogram of a Cu/SLEN/Li cell cycled between -0.4 V and 2.0 V vs. Li/Li⁺ at 250 $\mu\text{V s}^{-1}$ (cycles 2-33)

Table 3.2. Coulombic efficiencies of SLEN cell cycling

Cycle	Coulombic Efficiency	Cycle	Coulombic Efficiency
2	66%	18	79%
3	81%	19	91%
4	84%	20	91%
5	95%	21	90%
6	88%	22	95%
7	85%	23	99%
8	81%	24	98%
9	76%	25	98%
10	83%	26	94%
11	90%	27	97%
12	89%	28	99%
13	86%	29	98%
14	82%	30	99%
15	92%	31	98%
16	84%	32	99%
17	85%	33	98%

Chapter 4

Controlling Interfacial Properties of Lithium-Ion Battery Cathodes with Alkylphosphonate Self-Assembled Monolayers

This work was reproduced with minor modification with permission of the authors

4.1 Abstract

In this work, we report the preparation and characterization of modified LiMn_2O_4 (LMO) cathodes utilizing chemisorbed alkylphosphonic acids to chemically modify their surfaces. We utilize electrochemical methods to study ionic and molecular mobility through the alkylphosphonate self-assembled monolayers (SAMs) for different alkyl chain compositions, in order to better understand their impact on the lithium-ion electrochemistry. Electrochemical trends for different chains correlate to trends observed in contact angle measurements and solvation energies obtained from computational methods, indicating that attributes of the microscopic wettability of these interfaces with the battery electrolyte has an important impact on ionic mobility. The effects of surface modification on Mn dissolution is also reported. The alkylphosphonate layer provides an important mode of chemical stabilization to the LMO, suppressing Mn dissolution by 90% during extended immersion in electrolytes. A more modest reduction in dissolution is found upon galvanostatic cycling, in comparison to pristine LMO cathodes. Taken together, the data suggest that alkylphosphonates provide a versatile means for the surface modification of lithium-ion battery cathode materials allowing the design of specific interfaces through modification of organic chain functionalities.

4.2. Introduction

Over the past three decades, Li-Ion batteries (LIB) have become the most important energy storage technology adopted by the portable electronics and electric vehicle industries due to their high capacity, stability, and high voltage when compared to other batteries.⁵³

One feature which allows the lithium-ion battery to achieve stable operation at high voltages is the formation of the so-called solid electrolyte interphase (SEI). The SEI, whose importance is well established for the anode of LIBs,⁸¹ forms as a result of degradation reactions occurring between the electrode and the electrolyte.⁸¹ At the anode, these reactions result in the formation of a thin, electrically insulating, Li⁺-conductive material. This electrically insulating layer provides kinetic stability to the battery system.⁸¹ At the cathode, these reactions also yield a protective coating, the nature and function of which depends on specific battery chemistry.⁸¹ For example, it has recently been shown that the cathode interphase can incorporate Mn ions released from a Li_xNi_{0.5}Mn_{1.5}O₄ (LMNO) cathode into its structure, in the form of complexes with organic carbonates,⁸² thus preventing Mn migration to the anode where it negatively impacts battery performance.⁸³

The SEI is composed of two different components: a hard, inorganic layer and a soft, organic layer. The inorganic interphase is believed to be composed of lithium fluoride, lithium oxide, and carbonate salts formed from the decomposition of the inorganic salts (LiPF₆, LiBF₄, LiClO₄, etc.) and organic carbonates (propylene carbonate (PC), ethylene carbonate (EC), dimethyl carbonate (DMC), etc.).^{81, 84} The organic part of this layer comprises organic polymers, believed to be a mixture of polycarbonate and polyether molecules.^{84a} Attempts at controlling growth and composition of the SEI have been made through use of different electrolytes, or by incorporation of additive molecules.⁸¹

Although the natural SEI affords kinetic stability to the lithium-ion battery system, other degradative pathways are still present, particularly at the cathode. For example, in lithium manganese oxide (LMO) cathodes, capacity fade is related to the release of Mn^{2+} into the electrolyte.⁸⁵ Several different modifications of the LMO surface have been developed to prevent this dissolution, including surface oxides,⁸⁶ thin gold shells,⁸⁷ and graphene sheets.⁸⁸ In the current work, we examine the use of SAMs comprised of covalently attached alkylphosphonate adsorbates as a means to tune the surface and interfacial chemistry of LMO cathode materials to provide specific functionality.

The modification of metal oxide surfaces with SAMs has been widely investigated with notable exemplars utilizing molecules such as silanes, amines, carboxylic acids and alkylphosphonic acids.⁸⁹ Out of these different classes of molecules, phosphonic acids have been utilized extensively in the past to coat metal oxide surfaces (TiO_2 and ITO) used in devices such as sensors and light emitting devices.⁸⁹⁻⁹⁰ A previous study utilized a fluoroalkyl silane molecule to modify lithium manganese nickel oxide (LMNO).⁹¹ Here we use the flexibility attendant the alkylphosphonate platform to investigate the effect of different functionalities on LMO battery properties.

In this work we examine different properties of the LMO surface chemistry including wettability, electronic, and lithium ion conductivity. We tune that behavior by utilizing a series of alkylphosphonates with increasing chain size (butyl phosphonic acid (BPA), decyl phosphonic acid (DPA) and hexadecyl phosphonic acid (HDPA), or by utilizing a series of alkylphosphonates of similar chain lengths but different functional groups: DPA, 3,3,4,4,5,5,6,6,7,7,8,8,9,9,10,10,10-heptafluorodecylphosphonic acid (DFPA), and (2-(2-(2-Methoxy)-Ethoxy)-Ethoxy)-

alkylphosphonic acid (G3PA). The structures of the alkylphosphonates utilized in this work can be found in **Table 4.1**.

4.3. Results and Discussion

4.3.1. Surface Modification and Characterization of Model Alkylphosphonate Supported on Lithium Manganese Oxide

4.3.1.1 Effect of Surface Modification on LMO Cyclic Voltammetry

In order to characterize the phosphonate-modified LMO interface, we performed cyclic voltammetry (CV) measurements in an electrolyte containing ferrocene (Fc). Fc is a probe reporting on the electrochemical accessibility of the electrode.⁹² **Figure 4.1** shows a series of CVs obtained from thin LMO film cathodes immersed in a solution consisting of 1 M LiClO₄ + 3 mM Fc in PC. The CVs exhibit two features. The first, in the region marked 1, is associated with the 1 e⁻ transfer which converts Fc (at ca. 3V) to Fc⁺ at more positive potentials. For LMO, the peak splitting between the anodic and cathodic waves was ca. 140 mV, with larger splitting seen with different coatings. The second, in the region marked 2, is associated with the lithiation and delithiation of the LMO. The figure shows that different surface coatings lead to different behavior in the voltammogram in both regions 1 and 2.

We first address changes in the voltammogram with different surface coatings in region 1. **Figure 4.2** reports on the changes in anodic peak potentials (Figure 2a) and splitting (Figure 2b) for the Fc probe on the bare and modified LMO surface. Figure 2a shows that the anodic peak potential associated with the Fc/Fc⁺ couple in this solvent/electrolyte system occurs at 3.27 V vs. Li/Li⁺ for LMO or a control glassy carbon electrode, and 3.28 V on Au controls (**Figure 4.3a**).

The plots in Figure 2 demonstrate that as the alkyl chain length increases, the anodic peak potential becomes more positive and its magnitude increases as well. The magnitude of the

splitting seen in the Fc/Fc⁺ voltammetry correlates with the kinetic barrier of the electron transfer event.⁹³ Slowing the scan rate 10x leads to electron transport dynamics across the alkylphosphonate layer that more closely resemble that associated with a reversible redox couple (**Figure 4.3b**). We note that, even without an alkylphosphonate layer, the peak splitting is ca. 140 mV, which is considerably larger than the 59 mV expected for this one-electron couple. This larger splitting suggests that electron transfer is intrinsically inhibited within the LMO film itself, consistent with the high resistivity (ca. 5 MΩ) measured in the as-prepared thin film. This high resistivity is due to the insulating properties of LMO, in which conduction occurs via thermally-activated polaronic hopping between Mn³⁺ sites.⁹⁴ In contrast, peak splitting seen for the Fc couple at Au and glassy carbon interfaces are closer to the expected (ideal) values (80 mV and 65 mV, respectively). The origin of the larger split on Au is ascribed to the strong interactions that occur between the Au electrode and components of the organic electrolytes (which form a blocking layer inhibiting electron transfer).⁹⁵

The electrochemical properties of thin film Au electrodes modified with alkane thiol SAMs have been extensively studied.^{93, 96} The peak splitting of Fc is known to vary in alkane thiol modified electrodes as a function of alkane chain length (n).⁹³ A perfectly crystalline SAM grown on an atomically flat surface with chain lengths greater than 14 methyl groups leads to full suppression of Fc electrochemistry.^{96a} This suppression arises because Fc cannot closely approach the Au electrode through a defect-free SAM of that chain length, for which the through-chain electron tunneling rate is low. The Fc redox activity is not suppressed, however, on electrodes consisting of SAMs grown on rougher surfaces due to the presence of defects which allow direct approach of the Fc to the Au surface. In this case, increasing chain length does not result in fully

suppressed Fc electrochemistry. Nonetheless, the presence of the SAM does impact the Fc redox activity, which becomes less facile as chain length increases.⁹³

The thin film LMO surfaces utilized in this work exhibit a roughness (peak to valley) of ca. 50 nm (**Figure 4.4**). Roughness of this magnitude would preclude the formation of densely-packed phosphonate monolayers, and would allow Fc oxidation to occur in the presence of a SAM. We note in support of this that there is little change seen in either the peak splitting or the anodic onset potential between alkyl chains with $n = 10$ and 16. The current data does not discriminate whether it is intrinsic defects in the LMO thin film or more complex conformational dynamics in the SAMs that mediate these structure-property correlations.

Also provided in Figure 4.2 are data for the effect of LMO surface modification by phosphonate SAMs comprised of fluorinated and polyether chains. For similarly-sized alkyl chains (C_{10} alkyl, fluoroalkyl and C_7O_3 polyether), the Fc/Fc⁺ couple exhibits greater reversibility for the polyether relative to the alkyl chain, with the fluorinated chain exhibiting a somewhat intermediate effect. The possible origins of this behavior will be discussed below.

Figure 4.5a shows a plot of the peak splitting measured for the first lithium intercalation redox pair for both the bare and modified LMO surfaces (i.e., region 2 in Figure 1). The peak splitting value obtained for the bare LMO surface is similar to that previously reported for thin films deposited via RF magnetron sputtering.⁹⁷ As with the Fc/Fc⁺ case, an increase in alkylphosphonate chain length results in an increase in peak splitting up until $n = 10$. As with the Fc probe, there is little difference in peak splitting found for SAMs prepared using chain lengths between $n = 10$ and 16, likely for reasons similar to those discussed above.

Further chemical modifications of the chain structure result in behavior comparable to that observed for Fc. The phosphonate SAMs comprised of C₁₀ fluorinated chain (DFPA) exhibits a reversibility for lithiation similar to that found with the alkyl chain of the same length. The polyether variant, however, exhibits a lithiation activity similar to that of the pristine LMO surface. We note with interest that the main constituent of the organic speciation of the cathode solid-electrolyte interphase is in fact poly(ethylene glycol) dimethyl ether formed via an electrochemically mediated oligomerization process involving the EC solvent. Such moieties are similar in composition to the long polyether chain.^{84a}

4.3.1.2 Impedance Measurements

The interfaces of the modified LMO films were further characterized with Electrochemical Impedance Spectroscopy. Figure 4.5b shows Nyquist plots of the measured impedance for different modified interfaces, obtained at open circuit potential, prior to cycling. The impedance spectrum obtained for the pristine LMO surface is in agreement with values observed for LMO cathodes in the past.⁹⁸ Figure 4.5 shows that in most cases, surface modifications by the SAMs result in an increase in the measured impedance. The exception to this trend is the surface modified with a G3PA SAM, which shows behavior very similar to the uncoated LMO. The impedance spectra were fit to a simplified Randles circuit (see Figure 4.5b inset) and resistivity values were obtained for each modified interface. The resistivity of lithium battery cathodes in the frequency range utilized (1 MHz to 10 Hz) is typically attributed to conductivity of both electronic and ionic (Li⁺) components through the interface as well as through the solid-electrolyte interphase.⁹⁹ The simplified Randles circuit is usually augmented by more sophisticated models;^{99a} the fits made here are utilized to obtain trends. In the case of an uncycled cell with an open circuit potential (OCP) lower than the potential of oxidation of the PC solvent,¹⁰⁰ the resistivity values are

associated mainly with electronic and ionic conduction at the interface. The values obtained for R_{CT} for pristine LMO, DPA, DFPA, G3PA and HDPA were 230 Ω , 550 Ω , 870 Ω , 270 Ω , and 960 Ω , respectively. As expected, the R_{CT} increases with an increase in the length of the alkyl chain.¹⁰¹ The difference in R_{CT} seen between the similar chain length compositional series exhibits a trend similar to the results observed for the lithium intercalation dynamics (Figure 4.5a): the polyether chain presents the least resistivity, the alkyl chain an intermediate value, and in this case, the fluoroalkyl chain presents the highest resistivity.

4.3.1.3 XPS Measurements

The data presented above show that the electrochemical properties of the SAM-modified LMO substrates exhibit a dependence on both the chain length and composition of the modifying phosphonate adsorbate. The quantitative behaviors seen there likely arise from changes in the structure/adsorbate coverage as a result of different phosphonate adsorbates. Such differences likely lead to the different interface permeabilities noted for the Fc and Li^+ electrochemical probes studied above.

We carried out XPS studies to independently establish and correlate the association of modifications of the electrochemistry of the LMO surfaces with the surface coverage of the alkylphosphonates present in the SAM. Exemplary XPS data are shown in **Figure 4.6a-c** that allow an analysis on this basis. To facilitate comparison, the y-axes of these spectra have been offset and normalized to reflect the relative atomic concentration of the three elements (see the SI). Figure 4.6a shows the Mn 2p region characteristic of $LiMn_2O_4$ ¹⁰² and is consistent with Mn present as a mixture of Mn^{3+} and Mn^{4+} .¹⁰³ The C 1s spectra, shown in Figure 4.6b, indicates the presence of core level peaks expected for the distinct molecular structure of each alkylphosphonate adsorbate:

C-C (285.0 eV), C-O (286.6 eV), CF₂ (291.4 eV), and CF₃ (293.7 eV).¹⁰⁴ The suggested assignments of O-C=O (288.9 eV) and C-O peaks in the HDPA spectrum suggest the presence of a minor surface impurity within that SAM (likely in part due an adventitious uptake of CO₂ as a carbonate moiety). The P 2*p* spectra shown in Figure 4c establishes that the phosphorous present is in fact bound as a phosphonate (132.8 – 133.2 eV).¹⁰⁴⁻¹⁰⁵

In order to evaluate the surface coverages of the various adsorbates, the thicknesses of the monolayers were estimated using a procedure similar to that described previously in the literature.¹⁰⁶ This 2-layer model simplifies the properties associated with a thin attenuating overlayer (the SAM chain, which is assumed to be thin compared to the mean free path at the relevant photoelectron energies) to evaluate the intensities of the P 2*p* and Mn 2*p* signals, in order to extract the molecular density of a phosphorus containing SAM adsorbate standing on top of a quasi-infinite layer of manganese bound within the LMO substrate. This approximation is sufficient to provide a good qualitative measure of adsorbate related structure/property trends seen between the different SAM coatings.

Coverage estimates determined using the two-layer model are shown in Figure 4.6d and summarized in **Table 4.2**. Within the range of the errors, the adsorbate coverages estimated for all coatings are within the same order of magnitude, falling within the mid-range of 10¹³ molecules/cm². By way of comparison, alkylphosphonate coverages reported in other studies range from coverages of 10¹¹ to 10¹³ molecules/cm².^{106b-d} From these data we conclude that the differences seen in the electrochemical properties of the variously SAM-modified LMO electrodes cannot be simply ascribed to differences in the coverage of the alkylphosphonate adsorbates. This suggests that, while the SAMs do function as a barrier layer, other features/dynamical effects may also play a role in mediating the structure/rate and structure/property correlations seen.

4.3.1.4 Contact Angle Measurements

We made contact angle measurements to provide information about how the various SAMs impact the interaction of the LMO substrate with representative LIB electrolytes.¹⁰⁷ The data in **Figure 4.7** represent the contact angles measured for each of the SAMs in two different electrolyte systems: 1M LiClO₄ in PC solvent and 1M LiPF₆ in EC:DMC (1:1) solvent. The images in Figure 5a show representative profiles of electrolyte sessile droplets standing on the same films utilized for the XPS measurements.

Figure 4.7 b shows a plot of the contact angle (θ_s) values obtained with a PC/LiClO₄ electrolyte on the SAM modified LMO cathodes. The observed θ_s values range from 27° (G3PA, indicating wetting affinity for the surface) to 90° (DFPA, indicating non-wetting condition). The data in Figure 5b indicates that the contact angle increases as the length of the alkyl chain increases up to $n = 10$, which exhibits nearly the same contact angle as the $n = 16$ SAM. The similarities between the latter two in wetting behaviors mirror those in their CV data in this electrolyte.

Figure 4.7 c shows the values of θ_s measured for the EC:DMC electrolyte system. The contact angles measured in this case range from 30° (G3PA, highest wettability) to 75° (DFPA, lowest wettability). Again, θ_s (Figure 4.7 c) increases with chain length, albeit to a smaller degree than with PC/LiClO₄. It is important to note, however, that in EC:DMC, an increase in the alkyl chain from $n = 10$ to 16 results in an increase in contact angle and consequently a decrease in electrolyte affinity with the surface.

The contact angles measured show a good correlation with the trends observed in Figures 2 and 3, which suggests that electrolyte affinity with the modified LMO substrate is an important factor defining the permeability of electroactive species through the barrier-layer SAMs, as

proposed above. Attentive structure-property/structure-rate correlation would associate poorer wettability with less effective transport of electroactive species present in the electrolyte, including Li^+ ions.

4.3.1.5 Computational Studies of Alkylphosphonate Modified LMO

We used atomistic and first principles modeling to provide further, more quantitative insight into the formation, stability and wettability of LMO surfaces coated with alkylphosphonate SAMs. Because the solubility of the phosphonates in the electrolyte determines the relative stability of the SAM on the oxide surface upon electrochemical cycling, we computed their solvation free energies in PC with 1M LiClO_4 for comparison. Classical molecular dynamics (MD) simulations were employed to sample the possible conformations of the chains. Snapshots of the alkylphosphonate geometry from the classical MD trajectory were then computed within density function theory (DFT) incorporating a continuum solvation model to represent the instantaneous configuration of the PC electrolyte

Figure 4.8 and **Table 4.3** show the calculated solvation energies for different alkylphosphonates as a function of chain composition. The solvation energy of the phosphonic acid form of the adsorbate is computed for reference. Figure 6a shows that an increase in chain length from $n = 4$ to 10 (BPA to DPA) results in a decrease in stabilization of the respective alkylphosphonic acid solute due to an increasing cost of forming a cavity in the liquid of the size of the solute. From $n = 10$ to 16 (DPA to HDPA), the solvation energy remains roughly constant since the additional conformations available to the longer chain cause a decrease in energy which counteracts the increased energetic cost of cavity formation.¹⁰⁸ With respect to alkylphosphonic acids of the same length, Figure 6a shows that the fluoroalkylphosphonic acid (DFPA) has a similar

electrolyte affinity to the regular alkyl chain. Alternatively, the polyether based phosphonic acid (G3PA) shows the lowest solvation energy of all alkyl phosphonic acids simulated, and therefore the highest electrolyte affinity. These solvation energy results are in good agreement with the trends observed in the contact angle measurements and electrochemistry reported above. These results further support the important role electrolyte affinity plays in the modulation of electrochemical properties of LMO cathodes with the addition of alkylphosphonic acid based SAMs.

Figure 4.8b shows two stable binding conformations of phosphonic acid on energetically favorable (001) LMO surfaces.¹⁰⁹ Two different cases are shown: lithium poor surfaces and lithium rich surfaces. In the case of lithium-poor surfaces, two covalent bonds are formed between manganese atoms and the oxygens belonging to the phosphonate (-1.9 eV), with a third, weak O-H-O bond slightly stabilizing the configuration. In the case of a lithium-rich surface, a slightly less stable configuration (-1.6 eV) can also form, consisting of a covalent bond between a lithium atom and the oxygen atom belonging to the phosphonic acid and a strong O-H-O bond. Independent of surface lithium concentration, Figure 4.8b shows that phosphonic acid will attach to the LMO surface through a bidentate or tridentate bond consisting of one or two covalent metal-O bonds and an O-H-O bond. When a second covalent metal-O bond forms, one of the hydrogen atoms is found to dissociate from the phosphonic acid and adsorb on an LMO surface oxygen atom. The binding energies of the phosphonic acid on the surfaces are computed from the expression

$$E_{bind} = E_{LMO+PA} + nE_{LMO+H} - E_{PA} - (n+1)E_{LMO} \quad (\text{Eq. 4.1})$$

where n is the number of H atoms which dissociate from the phosphonic acid. The energies E_{LMO} , E_{LMO+H} , and E_{LMO+PA} are computed for the LMO surface with no adsorbates, adsorbed H, and

adsorbed phosphonic acid, respectively. The energy E_{PA} represents the energy of phosphonic acid in its reference state, either in vacuum or in solution. This expression for binding energy is similar to the one presented in the literature,¹¹⁰ except hydrogen on the LMO surface was chosen as a reference state rather than H₂ gas, due to presence of the electrochemical environment.

Table 4.4 reports the binding energies of phosphonic acid in vacuum and in solution, as well as the bond lengths for the configurations shown in Figure 6b. The solvation energies for the alkylphosphonates in LiClO₄/PC range from -0.5 to -0.8 eV (Table 4.3), indicating that phosphonic acid in electrolyte is less stable than phosphonic acid bound to the LMO surface. These results indicate that SAMs formed from bonding of phosphonic acids to LMO are stable in lithium-ion battery electrolytes, and that the stability is robust (i.e., able to fully saturate the adsorption isotherm) regardless of the amount of lithium on the surface. Similar results were also observed when calculating the solvation energies of alkylphosphonates in EC:DMC (1:1)/LiPF₆, where the energies ranged from -0.7 to 0.8 eV (Table 4.3), indicating that these SAMs are stable regardless of the electrolyte of choice.

The above alkylphosphonate binding conformations and energies are in reasonable agreement with previous results for alkylphosphonate association with indium tin oxide (ITO) and other materials.^{89, 110-111} Alkylphosphonate association with ITO is found to occur through oxygen-indium bonds of length 2.2-2.3 Å, with additional O-H-O bonds of length 1.37-1.6 Å. These M-O bond lengths are somewhat larger than those reported in Table 3. Binding energies of phosphonates on ITO range -1.6 to -1.7 eV, independent of coverage and particular binding configurations¹¹⁰. Both the shorter metal-oxygen bonds and the more stable binding energy for phosphonic acid on the LMO surface relative to ITO indicate that the ligands are more strongly bound on LMO. Though it has been found that as coverage increases, the most likely binding configuration may

change from bidentate to tridentate, the binding energies on ITO are remarkably constant.¹¹⁰ This limited role of intermolecular interactions in stabilizing the adsorbate provides support for the approximation to consider only one phosphonic acid per surface LMO unit cell (this coverage is also still within reasonable agreement with the XPS estimated values above).

When taken together, the calculations suggest that: 1) the stability of the monolayer in the electrolyte increases as a function of chain length and 2) stable binding configurations for phosphonate on LMO do exist, similar in type to those found previously for ITO; 3) the binding energies are sufficient to lead to high adsorbate coverage in the SAM.

4.3.2 Effect of Surface Modification on Battery Behavior

We next evaluate the effects of LMO surface modification with the alkylphosphonic acids on battery performance. Such coatings may be adventitious for a number of reasons. The coating may stabilize or alter the SEI. It may also stabilize the electrode material. Lithium-ion batteries utilizing LMO as a cathode are known to fade in capacity upon galvanostatic cycling.⁸⁷⁻⁸⁸ This capacity fade is attributed to both chemical corrosion by HF species formed from hydrolysis of LiPF_6 and the release of Mn^{2+} species into the electrolyte as the crystal lattice of LMO expands upon discharge. The Mn^{2+} species in the electrolyte interact with the SEI on the anode and/or plate on the anode itself, causing performance degradation.⁸⁵

4.3.2.1 ICP-MS Studies of Mn Dissolution

Table 4.5 shows the concentration of Mn in recovered electrolyte following 72 h immersion of modified LMO particles in 1 M LiPF_6 electrolyte in EC:DMC (1:1) solvent at room temperature.

Table 4.5 shows that the Mn concentration in the recovered electrolyte decreases drastically with an increase in the chain length of the decorating alkylphosphonate. We suggest that the longer chain length leads to less exposure of the LMO surface to the solvent, essentially terminating it as an insoluble metal oxide phosphonate complex and thus diminishing the amount of Mn^{2+} that can be dissolved. Interestingly, the contact angle measurements showed a similar trend, with longer alkylphosphonates yielding higher contact angles. All the alkylphosphonate-modified particles dissolve less Mn relative to the bare material, with the exception of the G3PA. Apparently, G3PA enhances Mn dissolution, albeit only slightly. This effect may be due to the increased solvent accessibility through this material, discussed above. Interestingly, DFPA blocks Mn dissolution to the same extent as the same chain length DPA, while contact angle measurements suggest that DFPA decoration leads to minimal solvent exposure. As we posit that Mn^{2+} dissolution in the SAM-modified LMO is a defect driven process, in that single sites are the locus of Mn dissolution activity, the contact angle measurements reflect more on the overall passivation of the substrate towards its interactions with the electrolyte solvent. This result suggests that the defect density in the DFPA SAMs is likely to be similar to those present in the DPA system.

4.3.2.2 Galvanostatic Cycling

We also compare the behavior of surface modified LMO in a lithium-ion half cells during galvanostatic cycling. This allows us to observe the impact of surface modification on battery operation, as well as test the Mn retention observed in the previous section by observing the change in capacity following 100 battery cycles. **Figure 4.9a** shows capacity retention curves obtained from galvanostatic cycling experiments for half-cells utilizing composite cathodes containing the modified LMO particles. Figure 4.9a shows that the maximum capacity obtained from these modified cathodes is altered by the presence of any alkylphosphonate coating. Uncoated LMO

exhibits the highest overall capacity, while BPA-, DFPA-, DPA-, and G3PA-modified LMO exhibit lower capacities. The lowest overall capacity was obtained for the 16-member alkylphosphonate (HDPA). Clearly the HDPA is most effective at blocking Li^+ access to LMO. The other phosphonates all block Li^+ access to some degree.

Figure 4.9 also shows the impact of cycling rate on the capacity of cathodes modified with alkylphosphonates of similar chain length. The magnitude of the capacity loss with increasing cycling rate is related, in part, to the permeability of the different artificial interfaces. Figure 7b shows that in the case of galvanostatic cycling, permeability is (most strikingly) higher for fluoroalkylphosphonates and lower for polyether modifications. Figure 4.9c shows the galvanostatic discharge capacity as a function of rate for surfaces coated with alkylphosphonates of different chain length. HDPA and DPA coated surfaces show similar rate performance compared to the pristine surface. The particles coated with BPA showed the highest improvement in capacity at a rate of 10 C.

The galvanostatic cycling data indicates that although surface modification will lead to an overall loss of capacity, one somewhat correlated to the alkylphosphonate chain length, it can also lead to improvements in other aspects of battery performance, such as allowing fast charging and discharging of a battery.

Table 4.6 shows the effect of surface modification on the capacity retention upon battery cycling. After 50 cycles (at a rate of 0.5 C), capacity loss can be observed for all the different systems studied. We show that there are differences between the capacity retention of pristine LMO and alkylphosphonate covered LMO. Capacity fade upon cycling was observed independent of which coating was utilized. The pristine LMO particles show the largest capacity fade after 100

cycles, with a capacity retention of 82%. The coated LMO particles show slightly improved capacity retention. The capacity fade observed for all coated particles is reduced by ca. 5% compared to uncoated LMO, independent of the ligand type.

Comparing these results to those observed in Table 4.5, it is apparent that although the coatings provide substantial protection from chemical etching, with a reduction in Mn dissolution of up to ca. 90%, their effects on capacity retention upon long-term cycling is rather more modest.

4.4 Concluding Remarks

This work shows that the interfacial properties of LMO cathodes are tunable by the decoration of the metal oxide surface with different alkylphosphonates. We showed that the wettability of the alkyl chain by the solvent plays a key role in facilitating the transport of molecules and ions through the phosphonate layer. Interfaces crafted from polyether-based alkylphosphonates allow Li^+ ion transport similar to that seen with unmodified thin film LMO. The transport of ions is influenced by the chain length of the alkylphosphonate and the presence of defects in the film.

DFT calculations show that phosphonic acid association with the LMO surface mimics that found when these molecules decorate other oxides such as ITO. A bidentate Mn-O bond, further stabilized by an O-H-O bond, seems to be the most likely configuration out of those studied in this work. When compared to the solvation energies of the precursor alkylphosphonic acids, the binding energies obtained suggest that the phosphonic acid modified LMO should be stable when immersed in the battery electrolyte, consistent with experiment.

Battery cycling studies show that the presence of hydrophobic chains at the surface of LMO leads to decreased Mn dissolution. During galvanostatic cycling, we found improved rate

performance for one coating (15-60% higher capacity at 5-10 C), and up to 5% improvement in capacity retention at 100 cycles for all coatings, compared to the pristine particles.

In conclusion, we demonstrated that modifying LMO cathodes enable interfacial property tuning through changes in the functional groups present in the precursor molecules. We suggest that, with careful design choices, it may be possible to create SAMs that further improve rate performance or capacity retention.

4.5 Experimental Section

Decoration of LiMn_2O_4 films and particles with Alkylphosphonate SAMs: Thin film LiMn_2O_4 (LMO) cathodes were prepared via RF Magnetron sputtering using a modification of a previously-reported methods.^{97, 112} A stoichiometric lithium manganese oxide plate (LTS Research Laboratories, Inc.) was used as the target. Pure argon was utilized to generate a plasma at a chamber pressure of 5 mTorr. The RF power applied to the target was 75 W. Polished 0.5-inch-diameter stainless steel discs were used as substrates for samples utilized in electrochemical experiments. The stainless steel acts as a current collector and provides a smooth, albeit disordered, surface for deposition. RF sputtering deposition of LMO on the stainless-steel substrate took place for a period of 16 hours. The amorphous films obtained were then annealed at a temperature of 700 °C for 1.5 hours. The resulting polycrystalline films were evaluated by profilometry and scanning electron microscopy. Films exhibited thicknesses of approximately 300 nm and surface roughness on the order of 30 nm.

Thin films of LMO and LMO particles (Sigma-Aldrich, electrochemical grade) were coated with alkylphosphonate self-assembled monolayers (SAMs). Alkylphosphonic-modified surfaces were prepared by immersion of LMO (films and particles) in 10 mM ethanol solutions of phosphonic acids for a period of 12 hours. The samples were then recovered and washed with

copious amounts of ethanol in order to remove any physisorbed molecules from the surfaces. The resulting modified LMO was then dried under vacuum at of 70 °C. Phosphonic acids used were: butyl phosphonic acid (BPA, Sigma-Aldrich, 98%), decylphosphonic acid (DPA, Sigma-Aldrich, 97%), hexadecylphosphonic acid (HDPa, Sigma-Aldrich, 98%), 3,3,4,4,5,5,6,6,7,7,8,8,9,9,10,10,10-Heptafluorodecylphosphonic acid (DFPA, Sigma-Aldrich, >95%), and (2-(2-(2-Methoxy)-Ethoxy)-Ethoxy)-alkylphosphonic acid (G3PA, Sikemia, >97%).

Electrochemical characterization: Cyclic Voltammetry (CV) experiments were conducted utilizing a CH Instruments electrochemical workstation (Model 1020C, Austin, TX). The three-electrode cell configuration utilized the thin film LMO cathodes as working electrode and lithium foil (Alfa-Aesar) as the counter/reference. A 1 M lithium perchlorate solution in propylene carbonate was chosen as the electrolyte to minimize the formation of natural solid-electrolyte interphase.^{81, 100, 113} CV experiments were carried out in an argon atmosphere glovebox, where both oxygen and water concentrations were ca. 1 ppm.

Potentiometric electrochemical impedance spectroscopy (PEIS) experiments were carried out utilizing a BioLogic electrochemical station (model SP-150). These experiments utilized an airtight Swagelok cell configuration, prepared in the glovebox, where the thin film LMO discs were utilized as working electrodes and lithium foil discs as counter/reference electrodes.¹¹⁴ 1 M LiClO₄ in PC electrolyte was utilized in these experiments. The sealed Swagelok cells were removed from the glovebox prior to PEIS experiments and the integrity of the cell was evaluated by CV.

Galvanostatic experiments were run in CR2032 coin cells obtained from MTI Corp. (Richmond, CA). The cell was assembled by first placing a ½ inch diameter circular piece of lithium in the base of the cell. A Whatman glass fiber paper (GF/F) was then placed on the lithium as separator and soaked in electrolyte (1 M LiPF₆ in 1:1 EC/DMC). The cathode was prepared by grinding the modified LMO particles with 10 wt% PTFE and 20 wt% Ketjen Black carbon in a mortar and pestle and the resulting material was pressed onto an Al mesh current collector. Typical loading was ~ 1 mg/cm². The cathode was then placed on top of the separator and a stainless-steel disc is placed on top as a spacer before placing a spring (MTI stainless steel wave spring for the CR2032 case) and the top cap. The cell was then sealed closed using an MTI hydraulic crimper. An MTI cycler (Richmond, CA) was used to cycle the cells. C rates were calculated using the mass active material in the cathode composite, assuming a working capacity of 130 mAh/g. Capacities are reported as a function of active material in the cathode.

Characterization of Modified LMO Surfaces: XPS measurements were made using a Kratos Axis Ultra X-ray photoelectron spectrometer (Kratos Analytical, Inc., Manchester, UK) using monochromatic Al K_α radiation (1486.6 eV) at 210 W (15 mA, 14 kV). The samples were affixed onto the sample holder using double-sided copper tape. High-resolution spectra were collected at an emission angle of 0° and a pass energy of 40 eV. The binding energy scale was referenced to the aliphatic C 1s signal at 285.0 eV. Quantitation was done using CasaXPS version 2.3.15 by determining the area under the curve after applying a Shirley background. Sensitivity factors were supplied by the instrument manufacturer. Further details regarding the quantification method can be found in the SI.

Computational Details: Classical molecular dynamics (MD) simulations using the LAMMPS software¹¹⁵ were used to sample the possible configurations of phosphonate molecules in the electrolyte solution. The construction of the simulation boxes, the non-reactive pair potentials used to represent the short-range interatomic forces, and the procedure for computing long-range electrostatic interactions are described in the SI. The systems were brought to mechanical and thermal equilibrium at 330 K using the NVT ensemble of N ose and Hoover.¹¹⁶ The systems were simulated using the Verlet algorithm¹¹⁷ and a 0.5 fs time step for a series of runs of time 0.5 ns until the system temperature and pressure could be verified, then the production run consisted of 2 consecutive simulations of time 1 ns to obtain reliable statistics.

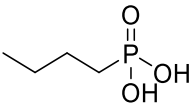
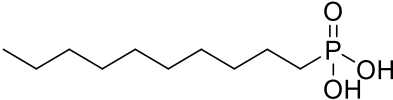
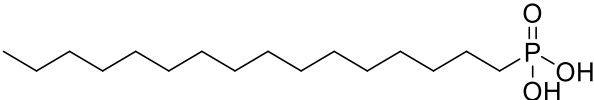
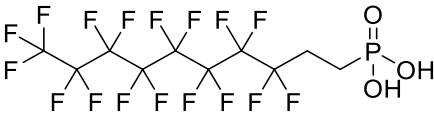
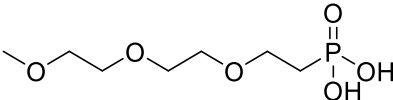
To compute solvation free energies of the phosphonates, 64 snapshots were randomly chosen from the 1 ns classical MD trajectory for each solute in the PC and EC:DMC electrolytes. The energy of each solute conformation was then evaluated using plane-wave density-functional theory (DFT) calculations in vacuum and with a continuum description of the surrounding electrolyte, using the JDFTx software and methodology described in the SI. DFT calculations in the presence of liquid electrolyte were performed within the framework of joint density-functional theory,¹¹⁸ using an implicit solvent approximation to the full theory known as Nonlinear PCM (with parameterizations described in Section 1.3 of the SI). This polarizable continuum-like solvation approach replaces the fluid by a local dielectric response and can account for dielectric saturation of the solvent due to high electric field.¹¹⁹ The solvation energy for each molecule was then computed by determining the difference in total energy between the molecule in liquid and the molecule in vacuum taking an average over the 64 snapshots.

DFT optimization of phosphonate binding to the LMO surface was conducted by placing a phosphonic acid on the low surface energy terminations.¹⁰⁹ A Hubbard U self-interaction

correction¹²⁰ to the PBE exchange correlation functional^{103a} was employed for the manganese *d* orbitals with $U=3.5$ eV. We constructed a slab supercell of LMO within periodic boundary conditions (as described in the SI). The phosphonic acid was placed on one side of the slab and the atoms on the other side of the slab were fixed to their bulk-like positions. The positions of the free atoms were optimized until total force was less than 10 meV/Å.

4.6 Figures and Tables

Table 4.1. Alkylphosphonate structures

Abbreviation	Name	Molecular Structure
BPA	Butyl Phosphonic Acid	
DPA	Decyl Phosphonic Acid	
HDP	Hexadecyl Phosphonic Acid	
DFPA	(3,3,4,4,5,5,6,6,7,7,8,8,9,9,10,10,10-Heptafluorodecyl) Phosphonic Acid	
G3PA	(2-(2-(2-Methoxy)-Ethoxy)-Ethoxy)-alkyl Phosphonic Acid	

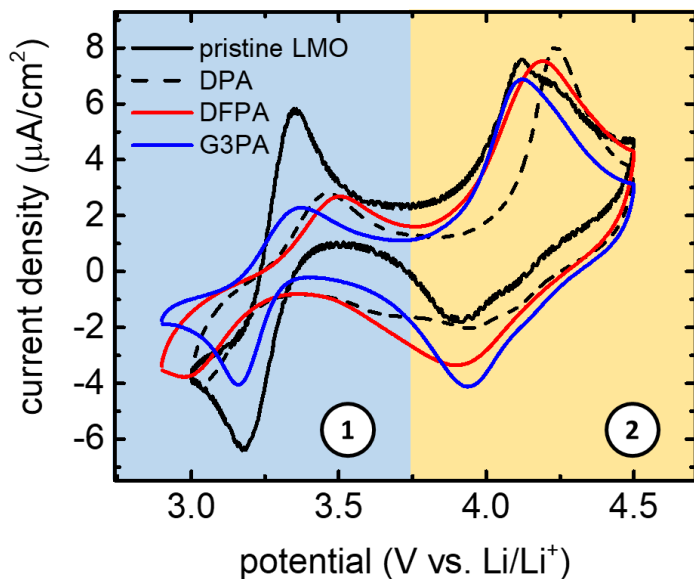


Figure 4.1. Cyclic voltammetry measurements of alkylphosphonate-modified LiMn_2O_4 thin films in 1 M LiClO_4 in PC electrolyte (with added 3 mM ferrocene) measured at a scan rate of 0.2 mV/s. Two different redox pairs are observed, containing information about the ferrocene oxidation (region 1) and lithiation/delithiation (region 2).

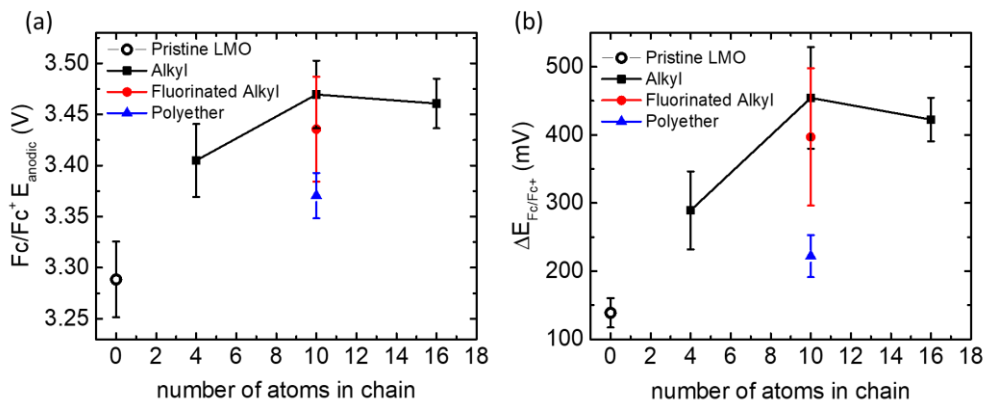


Figure 4.2. Effect of the alkylphosphonate SAMs on the Fc/Fc^+ oxidation (a) potential and (b) peak splitting, obtained from the CVs of coated LiMn_2O_4 thin films in 1M LiClO_4 in PC electrolyte, measured at scan rate of 0.2 mV/s, as a function of the ligand's chain length.

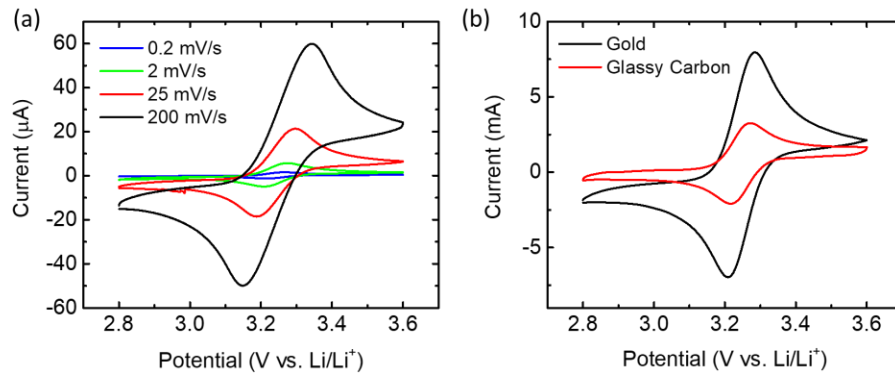


Figure 4.3. (a) Cyclic voltammogram of Fc/Fc⁺ probe in PC/LiClO₄ (1M) on a gold electrode (black) and a glassy carbon electrode (red), at a rate of 2 mV/s. (b) Cyclic voltammogram of Fc/Fc⁺ probe in PC/LiClO₄ (1M) on a gold electrode as a function for different cycling rates.

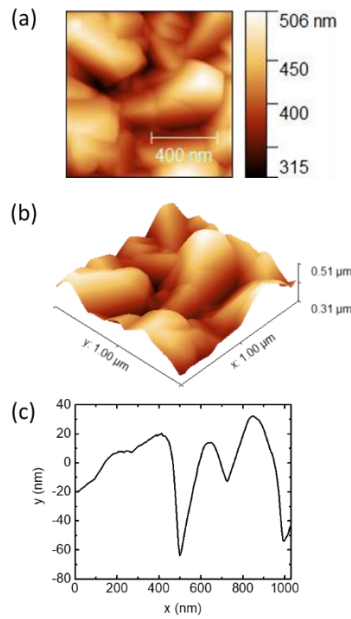


Figure 4.4. a) 2D AFM image of a 1 μm x 1 μm area of sputtered LMO sample. b) 3D representation of LMO surface as obtained by AFM. c) Typical height line profile used to obtain the average peak to valley roughness, calculated from line profiles of the entire measured area.

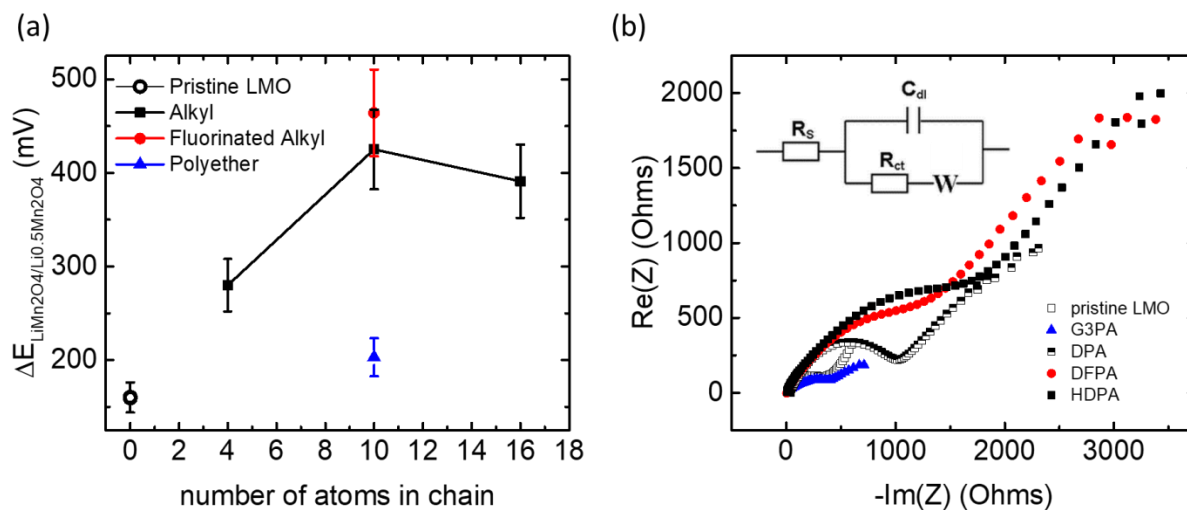


Figure 4.5. (a) Effect of alkylphosphonate SAMs on the lithium intercalation reaction peak splitting, obtained from the CVs of coated LiMn_2O_4 thin films in 1 M LiClO_4 in PC electrolyte, measured at scan rate of 0.2 mV/s. (b) Impedance measurement results for different coated interfaces and the Randles circuit (inset).

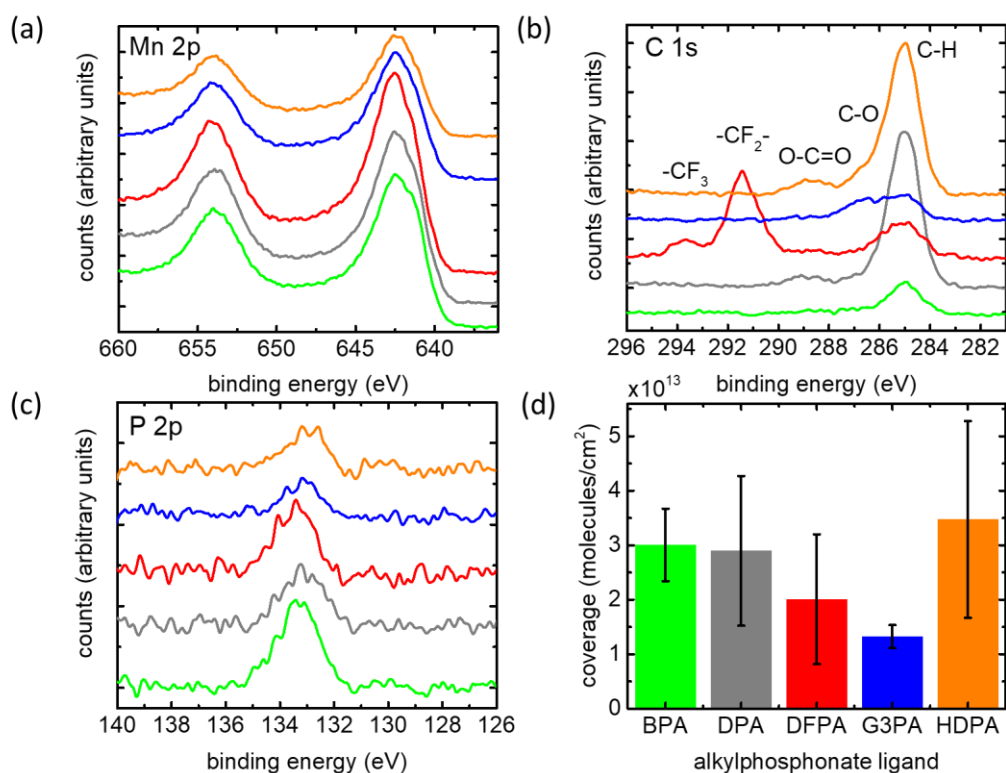


Figure 4.6. XPS of (a) Mn 2*p*, (b) C 1*s*, and (c) P 2*p* data from the principal elements of the alkylphosphonate monolayer surfaces stacked vertically in the following order: BPA-green (bottom), DPA-gray, DFPA-red, G3PA-blue, and HDPA-orange (top). (d) Alkylphosphonate monolayer surface coverage as determined using the two-layer model.

Table 4.2. XPS peak area, relative atomic concentration, and deduced coverage.

Alkylphosphate	Peak Area, count-eV/s			Atomic Concentration, %			Coverage
	I_{Mn}	I_C	I_P	N_{Mn}	N_C	N_P	(10^{13} molecules/cm ²)
BPA	16148. 2	604.8	273. 1	68.9 ± 5.7	24.7 ± 6.1	6.4 ± 1.9	3.0 ± 0.6
DPA	15910. 4	2612. 8	259. 5	37.6 ± 1.1	59.1 ± 1.4	3.4 ± 1.7	2.9 ± 1.4
DFPA	20160. 5	2341. 8	227. 6	46.0 ± 2.8	51.1 ± 2.9	2.8 ± 1.9	2.0 ± 1.2
G3PA	12728. 6	700.2	94.6	63.8 ± 5.2	33.6 ± 5.4	2.6 ± 0.6	1.3 ± 0.2
HDPa	8973.0	2770. 9	175. 3	24.6 ± 0.6	72.7 ± 1.2	2.6 ± 1.4	3.5 ± 1.8

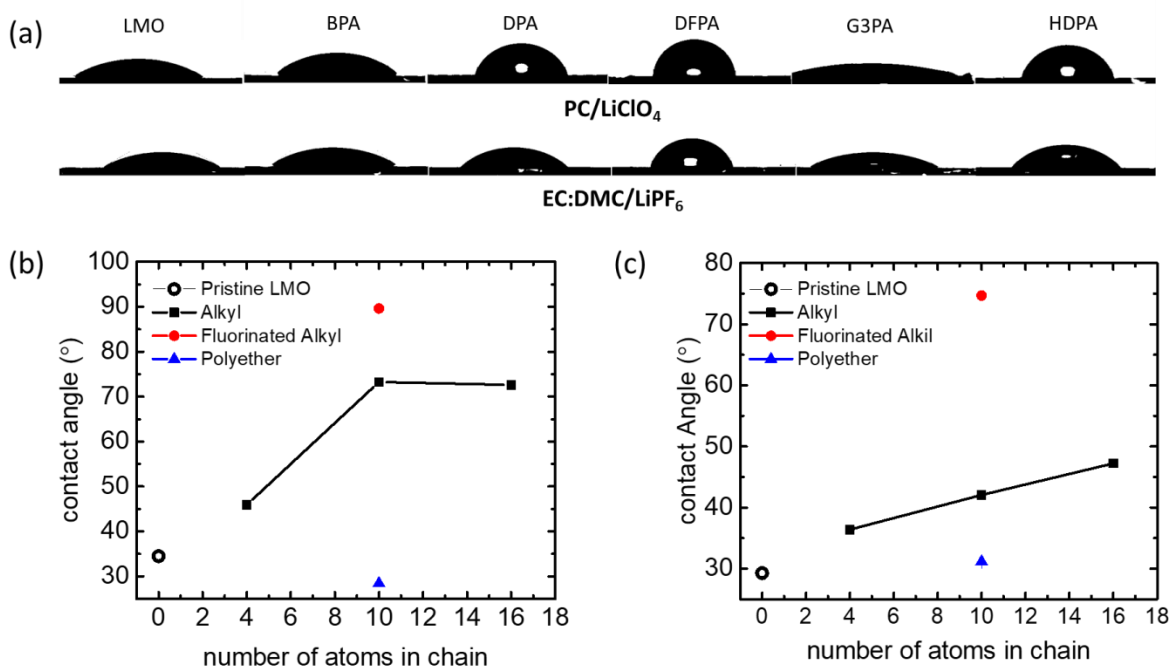


Figure 4.7. Contact angle measurements on coated LMO thin films in two different electrolyte systems: 1M LiClO₄ in propylene carbonate and 1M LiPF₆ in ethylene carbonate/dimethyl carbonate 1:1 solvent. (a) Recorded image of solvent droplets resting on SAM-modified LMO surfaces; fitted contact angle parameter by the Rame-Hart software for (b) LiClO₄/PC and (c) LiPF₆/EC:DMC.

Table 4.3. Solvation energies calculated via a combined classical MD and DFT approach for different phosphonic acids in PC/LiClO₄ and EC:DMC/LiPF₆ (also shown in Figure 6b)

Alkyl Phosphonic Acid	Solvation Energy in PC/LiClO ₄	Solvation Energy in EC:DMC/LiPF ₆
	eV	eV
H ₂ PO ₃	-0.67	-0.73
BPA	-0.63	-0.66
DPA	-0.55	-0.62
HDPA	-0.53	-0.59
DFPA	-0.57	-0.56
G3PA	-0.80	-0.93

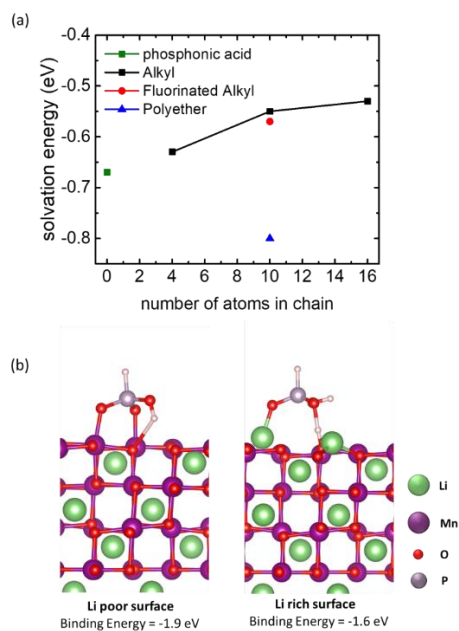


Figure 4.8. (a) Calculated solvation energy of different alkylphosphonate species in PC/LiClO₄ electrolyte, as determined by DFT. The line is provided as a guide for the eye. (b) Binding modes and energies of phosphonic acid on (001) lithium manganese oxide surfaces as determined by DFT calculations. Two different surface conditions, lithium rich (right) and lithium poor (left) are simulated.

Table 4.4. Phosphonic acid geometries and binding energies for Li-rich and Li-poor LMO (001) surfaces. Reference states for phosphonic acid in vacuum and solvated in PC/LiClO₄ are both considered.

Surface	Binding Energy Vacuum	Binding Energy in PC/LiClO ₄	Binding Mode	Bond length	Bond Angle
				Å	Degrees
Li-rich LMO (001)	-1.6	-1.0	1 Li-O	1.85	n/a
			1 O-H-O	2.53	176°
Li-poor LMO (001)	-1.9	-1.2	2 Mn-O	1.95,1.96	n/a
			1 O-H-O	2.84	120°

Table 4.5. Room temperature Mn dissolution study via ICP-MS

Alkyl Phosphonic Acid	Amount of Mn detected (ng/L)	% Less Mn dissolved relative to pristine LMO
		%
Pristine LMO	146	--
BPA	117	20
DPA	100	32
HDPA	13	91
DFPA	104	29
G3PA	163	-11

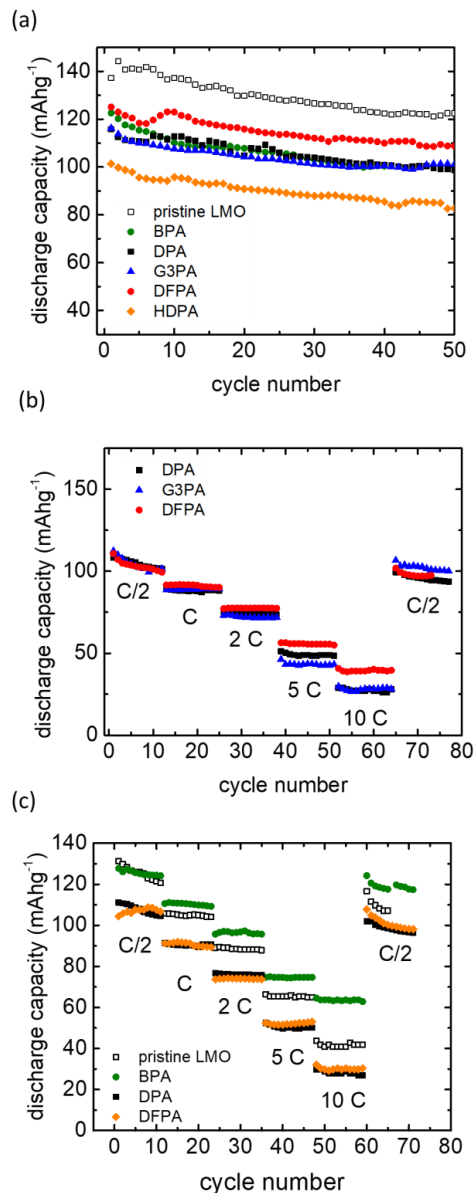


Figure 4.9. (a) Cycling experiments on lithium-ion half cells. Cathodes comprised of pristine LMO, and phosphonic acid (DPA, DFPA, HDPA, and G3PA) coated particles. All cells were cycled in 1M LiPF₆ in EC:DMC electrolyte at a rate of 0.5 C. (b) Cycling behavior of three different SAMs with the same chain length (DPA, G3PA and DFPA) as a function of cycling rate. (c) Cycling behavior of three different SAMs of different chain length (BPA, DPA and HDPA), as well as behavior of uncoated LMO as a function of cycling rate.

Table 4.6. Discharge capacities and capacity retention of the lithium-ion cells for pristine LiMn₂O₄ and coated cathode materials

Cycle Number	LMO	BPA	DPA	DFPA	G3PA	HDP A
	Discharge Capacity	Discharge Capacity	Discharge Capacity	Discharge Capacity	Discharge Capacity	Discharge Capacity
	(mA h /g)	(mA h / g)	(mA h /g)	(mA h /g)	(mA h /g)	(mA h /g)
5	141	115	111	118	110	96
50	122	100	99	109	101	83
100	115	--	94	102	95	82

Chapter 5

Li-S Conductive Polymer Hybrid Cathodes for Li-S Batteries

5.1 Abstract

Li-S Batteries are of great interest due to their high theoretical gravimetric and volumetric capacities. An inherent problem in these materials is that sulfur is insulating and intermediate reduction products are soluble in common electrolytes. Herein we explore how the chemical cross linking of poly sulfides with conductive polymers can both increase cycle stability and sulfur loadings in Li-S cathodes

5.2 Introduction

In the pursuit of revolutionary technologies such as grid scale storage and long range electric vehicles, there is a consensus that moving developing technologies radically different than traditional Li^+ batteries, so called “beyond Li^+ technologies” will be necessary to make the radical improvements in capacity needed. In addition to this technological leap there is a desire to move away from the use of metal cathodes which have high environmental impact and can be costly.¹²¹ Li-Sulfur cathodes have the potential to fulfil these needs as the material has an inherent energy density of 1670 mAh g^{-1} ¹²¹ and is fabricated from elemental sulfur and inexpensive byproduct of petrol refining.

Figure 5.1 shows the net reaction of proposed Li-S cathode. In theory this is ideal cathode chemistry as both the cyclic S_8 allotrope and the reduction product Li_2S are stable at the working potentials of the chemistry and in common electrolytes¹²¹. In practice a concerted 16 electron mechanism is improbable and instead the realized chemistry involves opening of the ring and reduction and reductive scission of individual sulfur units¹²². While the reduction

products are stable, the resulting long chain poly sulfides are soluble in most common electrolyte solvents. This is a problem from the perspective of active material loss, and also can cause issues through migration to the anode at which they are not stable.^{121a, 123} Additionally the inherently resistive nature of Sulfur necessitates high conductive additive loading contributing to non-active mass and cutting down of realized gravimetric and volumetric energy densities.¹²⁴

Recent strategies developed to increase Li-S stability by decreasing solubility is the so-called inverse vulcanization method.¹²⁵ In this process elemental sulfur is heated above 165°C to induce radical ring opening(**Figure 5.2a**). Left alone the sulfur would polymerize into long chain poly-sulfides, but with the addition of allyl containing organic molecules cross linking can occur (**Figure 5.2b**). It is theorized that the strong C-S bond acts as an anchor during redox and indeed Simmonds et al observe greatly increased stability.

In their initial report Simmonds et al use the organic cross linking component purely as a structural element to stabilize dissolution. In this project we theorize that the organic component of this process can be an electrically conductive polymer (polyaniline) that these cathodes will not only exhibit excellent stability, but enable high energy densities by minimizing non active conductive additives. We propose synthesizing polyaniline, functionalizing it with an allyl containing side chain via nucleophilic reactions, then using that functionalized polyaniline as a cross linker for inverse vulcanized Li-S cathodes (**Figure 5.3**)

5.3 Results and Discussion

Synthesis

Detailed procedure for the synthesis of each step including various conditions attempted will be given in the experimental section

Synthesis of EB (Polyaniline Emeraldine Base)

Synthesis of EB was routine and well documented in the literature. Successful synthesis is gauged by elemental analysis and comparison with literature IR spectrum.

Synthesis of AEB (Allylated Emeraldine Base)

Synthesis of AEB was carried out under various conditions to see their effect on the percent functionalization of repeat units (**Table 5.1**). As the starting material does not contain sulfur, the %S of the resulting compound by elemental analysis is used to determine functionalization percent.

Table entries 1,2,3 and three demonstrate that in ethanol at 60C there appears to be a maximum functionalization of ~15% of repeat units. Moving to forcing conditions such as refluxing in aqueous solution show modest improvements (entry 4), but the largest increase occurs when refluxing in aqueous pH 4 buffer. This has been shown previously in the literature and is a result of protonation of the nitrogen activating the ring for nucleophilic attack.

Synthesis of AEBS (Allylated Emeraldine Base Sulfur composite)

While full characterization of the AEBS cathode materials are incomplete, we can measure the resulting sulfur content as the polymer is thermally robust while the sulfur in the materials will thermally decompose at ~350 °C. **Figure 5.4** Displays thermogravimetric analysis of AEB polymer (black), elemental sulfur (red), AEBS from a reaction with 60% S loading (AEBS 60 green), AEBS from 85% S loading (AEBS 85 blue), and AEBS from 90% S loading (AEBS 90 pink). We can see that while the AEB back bone is thermally robust that sulfur completely degrades at ~ 350 °C. The degradation happens slightly sooner in the AEBS composites. While the loading to resulting S content is not linearly correlated, it can clearly be controlled as seen by the increasing S content of the composite with increasing loadings.

Taken together this synthetic work demonstrates that we can control both functionalization percent of the conductive polymer and the loadings of sulfur in the final cathode. Both of these should provide useful handles for optimization of electrochemical performance. Further more the choice of these methods was done with the intention of making this process amenable to all forms of Poly-Aniline. In theory we should be able to functionalize, nano-structured or electro polymerized films and investigate what novel properties those may facilitate. Alternative nucleophiles are another handle as there has been work on functional groups which provide self-doping and increased conductivity¹²⁶ or unique architectures to facilitate ion transport.¹²⁷

Figure 5.5 Shows the galvanostatic cycling of an AEBS cathode from AEBS reactions with 85% sulfur loading and AEB material from a 60C ethanol reaction (AEBS 15%) and AEB from a refluxed pH4 reaction (AEBS 46%). We can see that while cycling AEBS 46% is yet incomplete it shows significantly more decay than the AEBS 15% the only difference between the two samples is the nucleophilic addition reaction conditions with AEBS 15% being under milder conditions and resulting in 15% functionalization (table 5.1 entry 1) and AEBS 46% being under more forcing conditions and resulting in 46% functionalization (Table 5.1 entry 4). We expected that the higher degree of allylation would increase stability due to an increased amount of C-S bonds, but instead the opposite is true. Some evidence for an explanation can be seen in the charge and discharge curves (**Figure 5.6**) where AEBS 46 shows significantly more hysteresis between charge and discharge. This suggest poor kinetics of either electronic transport or ionic transport. Further test can show which is the case, but poor ionic transport could be the result of increased crosslinking creating dense networks which inhibit mass transport, while electronic transport could be inhibit by degradation under the forcing allylation conditions.

5.4 Conclusions

We have successfully synthesized a Polyaniline-Sulfur hybrid which shows promise as a Li-S cathode. Reaction conditions allow for the optimization of both PANI functionalization percent and sulfur loading in the final composite. Contrary to expected results increased functionalization percent decreases stability which may be the result of decreased ionic or electronic conductivity. Future work should focus on the optimization of composition as well as application to novel states of PANI including nano-structures and thin films.

5.5 Experimental

Synthesis of EB (Polyaniline Emeraldine Base) figure 5.3a

Polyaniline Emeraldine base was synthesized as previously reported in the literature¹²⁸. In a typical procedure 200mmol of aniline is dissolved in 200mL of 1M HCl. In a separate container 70mmol of Ammonium peroxydisulfate is dissolved in 100mL of 1M HCl. The aniline solution is cooled to 0C in ice bath and stirred rapidly. The Ammonium peroxydisulfate is slowly added and the reaction stirred at RT for 3 hours. The solution quickly turns dark blue to dark green. After 3 hours the reaction is filtered and washed with 0.1M HCl, EtOH and Acetone. The result is a Green solid. This is the Emeraldine salt form and is not long term bench stable. The salt is converted to the base by dispersing the resulting solid in 400mL of DI water and stirring rapidly. 40mL of NH₄OH is added and the resulting mixture stirred for 20minutes. A rapid change to blue occurs. The reaction is filtered then washed with water, ethanol, and acetone before being dried at 60 C overnight under vacuum. The resulting deep blue solid is the PANI- Emeraldine base “**EB**”

Synthesis of AEB (Allylated Polyaniline Emeraldine Base) figure 5.3b

The nucleophilic addition of allylmercaptan was achieved by dispersing EB in the desired

solvent at a ratio of 10mg EB/ 1 mL of solvent. Ally mercaptan is then added to make the solution 0.5M in allyl mercaptan. With no special precautions to air or moisture the reaction is then stirred at the temperatures listed in table 5.1 for the times listed. The reaction is then filtered and washed throughoutly with ethanol, water, and acetone before drying at 60C overnight in vacuum.. There is change from dark blue to light blue. The product is “**AEB**”

Synthesis of AEBS (Allylated Polyaniline Emeraldine Base sulfur composite) figure 5.3c

AEB and elemental sulfur flake (Sigma 99.99% trace metal basis) are ground together in a mortar and pestle in the desired ratio (i.e from AEBS 85 85mg sulfur/15mg of AEB) A 10mL round bottom is then placed under vacuum and flame dried. The mixed solids are then added to the flask and N₂ and vacuum are cycled on the material 5x to exclude oxygen. The flask is then submerged in an oil bath at 135 C for 2 hours. (Note submerged as much of the flask as possible ideally all the way up to where the septa meets the neck. During the second heating step Sulfur has significant vapor pressure and can recrystallize on cool parts of the flask adding variability to the results). After 2 hours increase the temperature to 185C and react for 4 hours. Let the reaction then cool to RT and the resulting black solid is your product AEBS

Electrochemical measurements

Electrochemical measurements are all covered in other portions of this thesis and were run in the same manner.

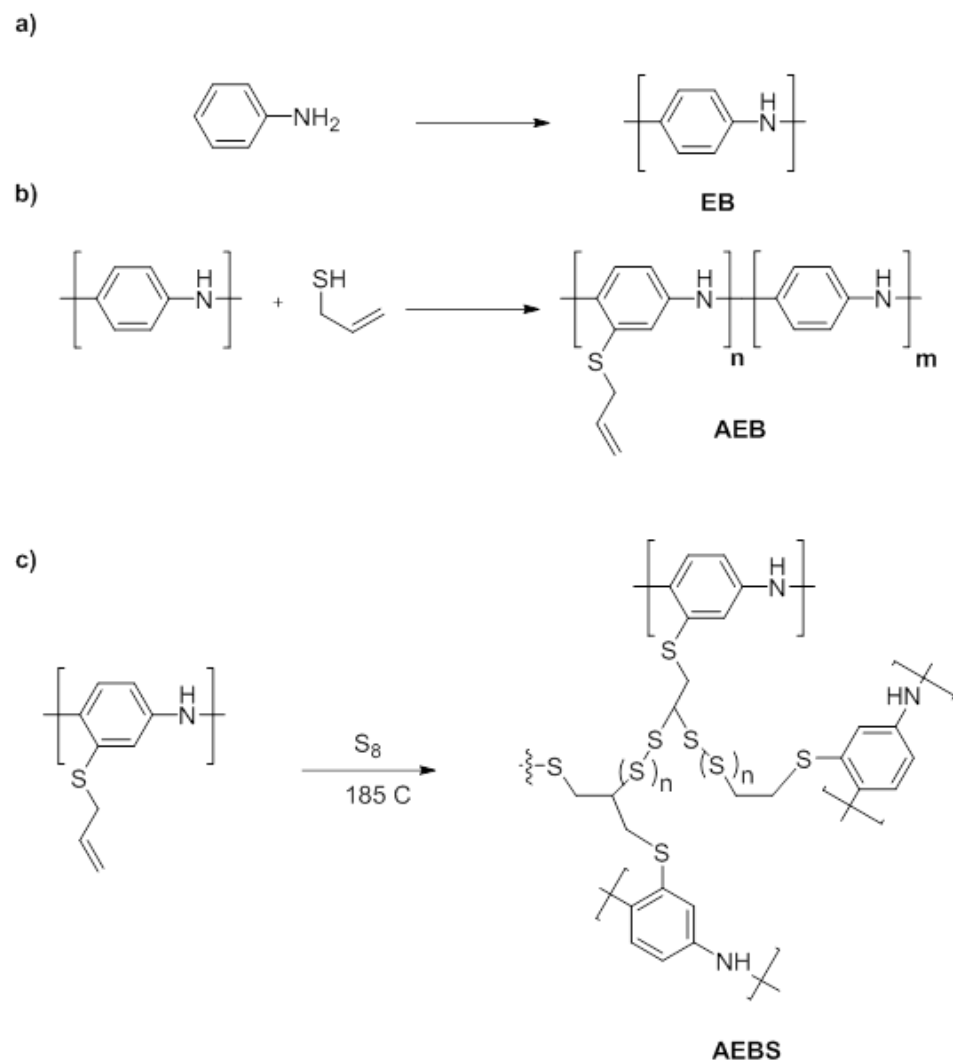


Figure 5.3. Chemical outline of proposed Li-S cathode.

Table 5.1. Conditions for AEB synthesis

Sample	Rxn Time (h)	Rxn Temp (C)	Solvent	pH	Functionalization %
1	4	60	EtOH	N/A	15
2	24	60	EtOH	N/A	15
3	48	60	EtOH	N/A	16
4	24	100	H ₂ O	(uncontrolled)	20
5	4	100	H ₂ O	4 (buffer)	46

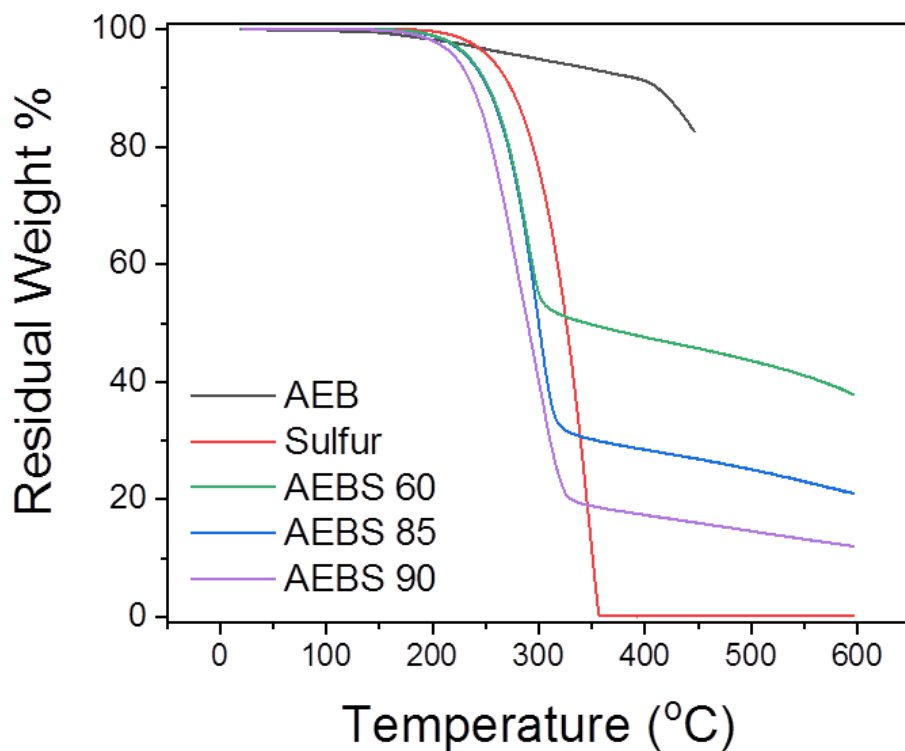


Figure 5.4. TGA analysis of AEB, S, AEBS 60, AEBS 85, AEBS 90

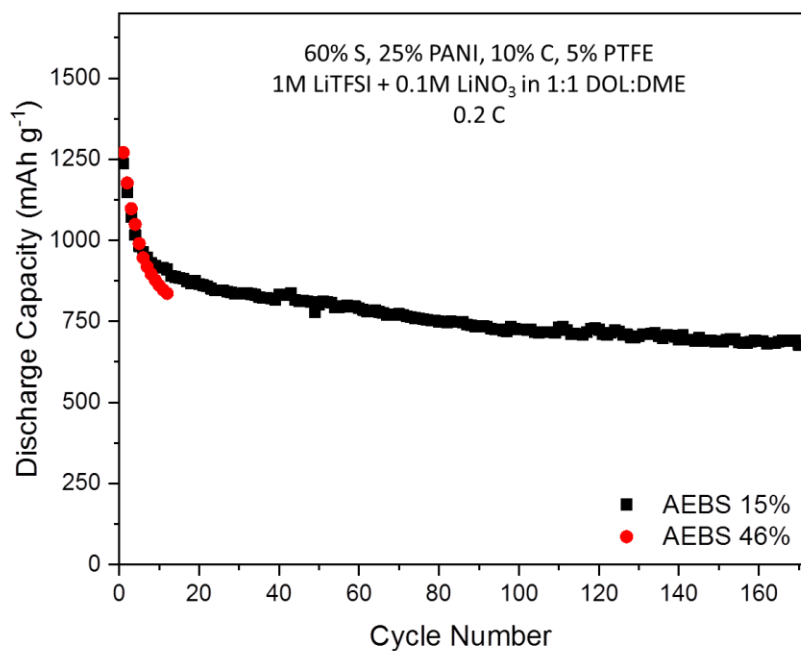


Figure 5.5. Galvanostatic cycling of AEBS cathodes at 0.2C

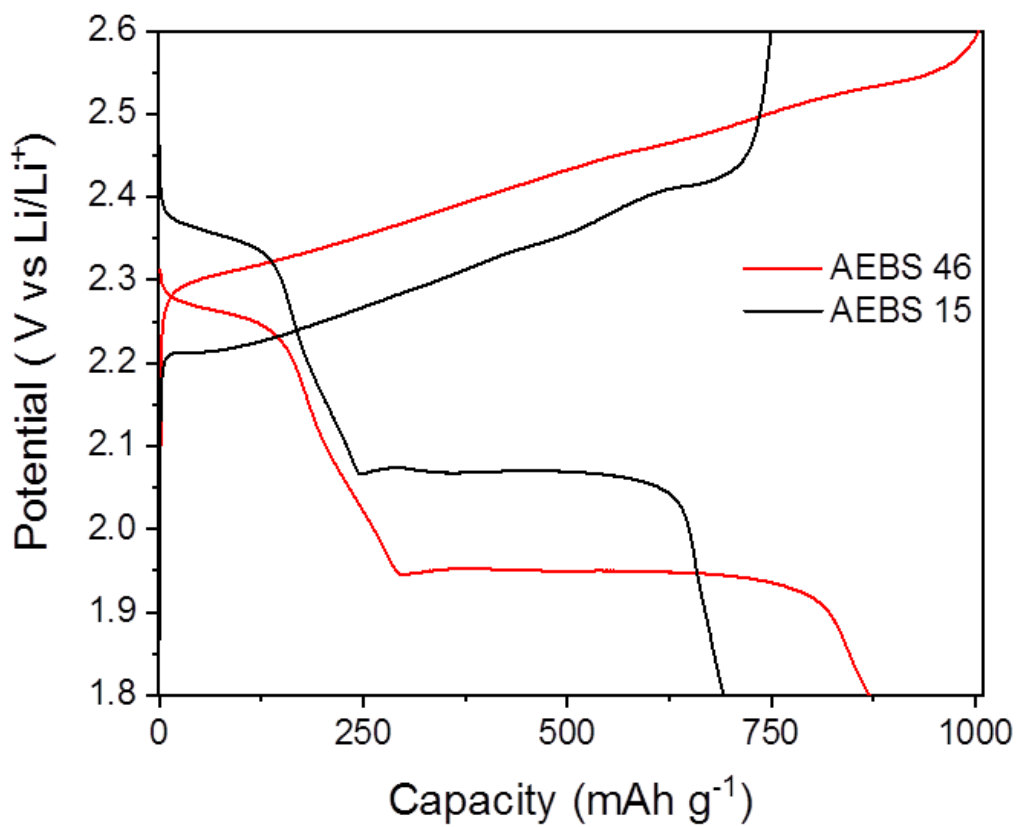


Figure 5.6. Galvanostatic charge and discharge curves for AEBS composites

References

1. (a) Mohtasham, J., Review Article-Renewable Energies. *Energy Procedia* **2015**, *74*, 1289-1297; (b) Dincer, I.; Acar, C., A review on clean energy solutions for better sustainability. *International Journal of Energy Research* **2015**, *39* (5), 585-606.
2. (a) Yilanci, A.; Dincer, I.; Ozturk, H. K., A review on solar-hydrogen/fuel cell hybrid energy systems for stationary applications. *Progress in Energy and Combustion Science* **2009**, *35* (3), 231-244; (b) Yang, Z.; Zhang, J.; Kintner-Meyer, M. C. W.; Lu, X.; Choi, D.; Lemmon, J. P.; Liu, J., Electrochemical Energy Storage for Green Grid. *Chem. Rev.* **2011**, *111* (5), 3577-3613.
3. Martinot, E., Grid Integration of Renewable Energy: Flexibility, Innovation, and Experience. *Annual Review of Environment and Resources* **2016**, *41* (1), 223-251.
4. E. Moore, G., *Cramming more components onto integrated circuits*, Reprinted from *Electronics*, volume 38, number 8, April 19, 1965, pp.114 ff. 2006; Vol. 11, p 33-35.
5. Thackeray, M. M.; Wolverton, C.; Isaacs, E. D., Electrical energy storage for transportation-approaching the limits of, and going beyond, lithium-ion batteries. *Energ. Environ. Sci.* **2012**, *5* (7), 7854-7863.
6. (a) Armand, M.; Tarascon, J. M., Building better batteries. *Nature* **2008**, *451* (7179), 652-657; (b) Cheng, F.; Liang, J.; Tao, Z.; Chen, J., Functional Materials for Rechargeable Batteries. *Advanced Materials* **2011**, *23* (15), 1695-1715.
7. Dunn, B.; Kamath, H.; Tarascon, J.-M., Electrical Energy Storage for the Grid: A Battery of Choices. *Science* **2011**, *334* (6058), 928-935.
8. (a) Li, H.; Wang, Z.; Chen, L.; Huang, X., Research on Advanced Materials for Li-Ion Batteries. *Advanced Materials* **2009**, *21* (45), 4593-4607; (b) Yao, F.; Pham, D. T.; Lee, Y. H., Carbon-Based Materials for Lithium-Ion Batteries, Electrochemical Capacitors, and Their Hybrid Devices. *ChemSusChem* **2015**, *8* (14), 2284-2311.
9. (a) Whittingham, M. S., Lithium Batteries and Cathode Materials. *Chem. Rev.* **2004**, *104* (10), 4271-4302; (b) Nitta, N.; Wu, F.; Lee, J. T.; Yushin, G., Li-Ion battery materials: present and future. *Mater. Today* **2015**, *18* (5), 252-264.
10. Kalhoff, J.; Eshetu, G. G.; Bresser, D.; Passerini, S., Safer Electrolytes for Lithium-Ion Batteries: State of the Art and Perspectives. *ChemSusChem* **2015**, *8* (13), 2154-2175.
11. Bard, A.; Faulkner, L., *Electrochemical Methods: Fundamentals and Applications*. John Wiley & Sons, Inc: 2001.
12. Kamali, A.; Fray, D. J., *Review on Carbon and Silicon Based Materials as Anode Materials for Lithium Ion Batteries*. 2010; Vol. 13, p 147-160.
13. Kozen, A. C.; Lin, C.-F.; Pearse, A. J.; Schroeder, M. A.; Han, X.; Hu, L.; Lee, S.-B.; Rubloff, G. W.; Noked, M., Next-Generation Lithium Metal Anode Engineering via Atomic Layer Deposition. *ACS Nano* **2015**, *9* (6), 5884-5892.
14. (a) Schipper, F.; Erickson, E. M.; Erk, C.; Shin, J.-Y.; Chesneau, F. F.; Aurbach, D., Review—Recent Advances and Remaining Challenges for Lithium Ion Battery Cathodes: I. Nickel-Rich, LiNi_xCoyMnzO₂. *J. Electrochem. Soc.* **2017**, *164* (1), A6220-A6228; (b) Daniel, C.; Mohanty, D.; Li, J.; Wood, D. L., Cathode materials review. *AIP Conference Proceedings* **2014**, *1597* (1), 26-43; (c) Cherkouk, C.; Nestler, T., Cathodes - Technological review. *AIP Conference Proceedings* **2014**, *1597* (1), 134-145.
15. Desilvestro, J.; Haas, O., Metal Oxide Cathode Materials for Electrochemical Energy Storage: A Review. *J. Electrochem. Soc.* **1990**, *137* (1), 5C-22C.

16. (a) Marcinek, M.; Syzdek, J.; Marczewski, M.; Piszcz, M.; Niedzicki, L.; Kalita, M.; Plewa-Marczewska, A.; Bitner, A.; Wieczorek, P.; Trzeciak, T.; Kasprzyk, M.; P.Łęzak; Zukowska, Z.; Zalewska, A.; Wieczorek, W., Electrolytes for Li-Ion transport – Review. *Solid State Ionics* **2015**, *276*, 107-126; (b) Li, Q.; Chen, J.; Fan, L.; Kong, X.; Lu, Y., Progress in electrolytes for rechargeable Li-based batteries and beyond. *Green Energ. Environ.* **2016**, *1* (1), 18-42.
17. Xu, K., Electrolytes and Interphases in Li-Ion Batteries and Beyond. *Chem. Rev.* **2014**, *114* (23), 11503-11618.
18. Cheng, X.-B.; Zhang, R.; Zhao, C.-Z.; Zhang, Q., Toward Safe Lithium Metal Anode in Rechargeable Batteries: A Review. *Chem. Rev.* **2017**, *117* (15), 10403-10473.
19. (a) Judez, X.; Zhang, H.; Li, C.; Eshetu, G. G.; González-Marcos, J. A.; Armand, M.; Rodriguez-Martinez, L. M., Review—Solid Electrolytes for Safe and High Energy Density Lithium-Sulfur Batteries: Promises and Challenges. *J. Electrochem. Soc.* **2018**, *165* (1), A6008-A6016; (b) Kerman, K.; Luntz, A.; Viswanathan, V.; Chiang, Y.-M.; Chen, Z., Review—Practical Challenges Hindering the Development of Solid State Li Ion Batteries. *J. Electrochem. Soc.* **2017**, *164* (7), A1731-A1744; (c) Zheng, F.; Kotobuki, M.; Song, S.; Lai, M. O.; Lu, L., Review on solid electrolytes for all-solid-state lithium-ion batteries. *J. Power Sources* **2018**, *389*, 198-213.
20. (a) Yiwen, W.; Ronghua, Z.; Junmin, N.; Dong, S.; Yongcai, Q.; Shu-Lei, C., Quinone Electrode Materials for Rechargeable Lithium/Sodium Ion Batteries. *Advanced Energy Materials* **2017**, *7* (24), 1700278; (b) Larcher, D.; Tarascon, J. M., Towards greener and more sustainable batteries for electrical energy storage. *Nature Chemistry* **2014**, *7*, 19; (c) Bernhard, H.; Andreas, W.; S., S. U., Carbonyls: Powerful Organic Materials for Secondary Batteries. *Advanced Energy Materials* **2015**, *5* (11), 1402034.
21. Haiyan, C.; Michel, A.; Gilles, D.; Franck, D.; Philippe, P.; Jean-Marie, T., From Biomass to a Renewable LiXC6O6 Organic Electrode for Sustainable Li-Ion Batteries. *ChemSusChem* **2008**, *1* (4), 348-355.
22. (a) Fei, Y.; Tho, P. D.; Hee, L. Y., Carbon-Based Materials for Lithium-Ion Batteries, Electrochemical Capacitors, and Their Hybrid Devices. *ChemSusChem* **2015**, *8* (14), 2284-2311; (b) Muench, S.; Wild, A.; Friebe, C.; Häupler, B.; Janoschka, T.; Schubert, U. S., Polymer-Based Organic Batteries. *Chem. Rev.* **2016**, *116* (16), 9438-9484.
23. Ting, M.; Qing, Z.; Jianbin, W.; Zeng, P.; Jun, C., A Sulfur Heterocyclic Quinone Cathode and a Multifunctional Binder for a High-Performance Rechargeable Lithium-Ion Battery. *Angew. Chem. Int. Ed.* **2016**, *55* (22), 6428-6432.
24. Lee, J.; Kim, H.; Park, M. J., Long-Life, High-Rate Lithium-Organic Batteries Based on Naphthoquinone Derivatives. *Chem. Mater.* **2016**, *28* (7), 2408-2416.
25. Zhiping, S.; Yumin, Q.; L., G. M.; Duihai, T.; Terrence, X.; Minoru, O.; Hui, Z.; Haoshen, Z.; Donghai, W., Polyanthraquinone as a Reliable Organic Electrode for Stable and Fast Lithium Storage. *Angewandte Chemie International Edition* **2015**, *54* (47), 13947-13951.
26. (a) Sterby, M.; Emanuelsson, R.; Huang, X.; Gogoll, A.; Strømme, M.; Sjödin, M., Characterization of PEDOT-Quinone Conducting Redox Polymers for Water Based Secondary Batteries. *Electrochim. Acta* **2017**, *235*, 356-364; (b) Emanuelsson, R.; Karlsson, C.; Huang, H.; Kosgei, C.; Strømme, M.; Sjödin, M., Quinone based conducting redox polymers for electrical energy storage. *Russian Journal of Electrochemistry* **2017**, *53* (1), 8-15; (c) Siew, L.; Ernould, B.; Gohy, J.-F.; Vlad, A., On the improved electrochemistry of hybrid conducting-redox polymer electrodes. *Scientific Reports* **2017**, *7* (1), 4847.

27. (a) Häring, D.; Novák, P.; Haas, O.; Piro, B.; Pham, M. C., Poly(5-amino-1,4-naphthoquinone), a Novel Lithium-Inserting Electroactive Polymer with High Specific Charge. *Journal of The Electrochemical Society* **1999**, *146* (7), 2393-2396; (b) Nokami, T.; Matsuo, T.; Inatomi, Y.; Hojo, N.; Tsukagoshi, T.; Yoshizawa, H.; Shimizu, A.; Kuramoto, H.; Komae, K.; Tsuyama, H.; Yoshida, J.-i., Polymer-Bound Pyrene-4,5,9,10-tetraone for Fast-Charge and -Discharge Lithium-Ion Batteries with High Capacity. *J. Am. Chem. Soc.* **2012**, *134* (48), 19694-19700.
28. Hong, L.; Zhaoxiang, W.; Liquan, C.; Xuejie, H., Research on Advanced Materials for Li-ion Batteries. *Advanced Materials* **2009**, *21* (45), 4593-4607.
29. (a) Yanliang, L.; Zhanliang, T.; Jun, C., Organic Electrode Materials for Rechargeable Lithium Batteries. *Advanced Energy Materials* **2012**, *2* (7), 742-769; (b) Song, Z.; Zhou, H., Towards sustainable and versatile energy storage devices: an overview of organic electrode materials. *Energ. Environ. Sci.* **2013**, *6* (8), 2280-2301.
30. Liang, Y.; Zhang, P.; Chen, J., Function-oriented design of conjugated carbonyl compound electrodes for high energy lithium batteries. *Chem. Sci.* **2013**, *4* (3), 1330-1337.
31. Kawai, T.; Oyaizu, K.; Nishide, H., High-Density and Robust Charge Storage with Poly(anthraquinone-substituted norbornene) for Organic Electrode-Active Materials in Polymer-Air Secondary Batteries. *Macromolecules* **2015**, *48* (8), 2429-2434.
32. Song, Z.; Qian, Y.; Zhang, T.; Otani, M.; Zhou, H., Poly(benzoquinonyl sulfide) as a High-Energy Organic Cathode for Rechargeable Li and Na Batteries. *Adv. Sci.* **2015**, *2* (9), 1500124.
33. Song, Z.; Qian, Y.; Liu, X.; Zhang, T.; Zhu, Y.; Yu, H.; Otani, M.; Zhou, H., A quinone-based oligomeric lithium salt for superior Li-organic batteries. *Energ. Environ. Sci.* **2014**, *7* (12), 4077-4086.
34. Birch, A. M.; Mercer, A. J. H.; Chippendale, A. M.; Greenhalgh, C. W., Quinizarin boroacetate and 1,4-diaminoanthraquinone diboroacetate as dienophiles. *Journal of the Chemical Society, Chemical Communications* **1977**, (21), 745-746.
35. Song, Z.; Zhan, H.; Zhou, Y., Anthraquinone based polymer as high performance cathode material for rechargeable lithium batteries. *Chem. Commun.* **2009**, (4), 448-450.
36. Pecher, O.; Carretero-González, J.; Griffith, K. J.; Grey, C. P., Materials' Methods: NMR in Battery Research. *Chem. Mater.* **2017**, *29* (1), 213-242.
37. Zhao, L.; Wang, W.; Wang, A.; Yuan, K.; Chen, S.; Yang, Y., A novel polyquinone cathode material for rechargeable lithium batteries. *J. Power Sources* **2013**, *233*, 23-27.
38. Wain, A. J.; Wildgoose, G. G.; Heald, C. G. R.; Jiang, L.; Jones, T. G. J.; Compton, R. G., Electrochemical ESR and Voltammetric Studies of Lithium Ion Pairing with Electrogenerated 9,10-Anthraquinone Radical Anions Either Free in Acetonitrile Solution or Covalently Bound to Multiwalled Carbon Nanotubes. *The Journal of Physical Chemistry B* **2005**, *109* (9), 3971-3978.
39. Pavlishchuk, V. V.; Addison, A. W., Conversion constants for redox potentials measured versus different reference electrodes in acetonitrile solutions at 25°C. *Inorganica Chimica Acta* **2000**, *298* (1), 97-102.
40. Lei, Z.; Wei-kun, W.; An-bang, W.; Zhong-bao, Y.; Shi, C.; Yu-sheng, Y., A MC/AQ Parasitic Composite as Cathode Material for Lithium Battery. *J. Electrochem. Soc.* **2011**, *158* (9), A991-A996.
41. Schon, T. B.; McAllister, B. T.; Li, P.-F.; Seferos, D. S., The rise of organic electrode materials for energy storage. *Chemical Society Reviews* **2016**, *45* (22), 6345-6404.

42. M., Z., Polycyclic Hydrocarbons. Band II. Von E. Clar. Academic Press, London-New York; Springer-Verlag, Berlin-Göttingen-Heidelberg 1964. 1. Aufl., LVIII, 487 S., 153 Abb., geb. DM 78.40. *Angewandte Chemie* **1965**, 77 (19), 876-876.
43. Wu, D.; Xie, Z.; Zhou, Z.; Shen, P.; Chen, Z., Designing high-voltage carbonyl-containing polycyclic aromatic hydrocarbon cathode materials for Li-Ion batteries guided by Clar's theory. *J. Mater. Chem. A* **2015**, 3 (37), 19137-19143.
44. Xu, W.; Read, A.; Koech, P. K.; Hu, D.; Wang, C.; Xiao, J.; Padmaperuma, A. B.; Graff, G. L.; Liu, J.; Zhang, J.-G., Factors affecting the battery performance of anthraquinone-based organic cathode materials. *Journal of Materials Chemistry* **2012**, 22 (9), 4032-4039.
45. Tobias, J.; D., H. M.; S., S. U., Powering up the Future: Radical Polymers for Battery Applications. *Advanced Materials* **2012**, 24 (48), 6397-6409.
46. (a) Ulas, G.; Lemmin, T.; Wu, Y.; Gassner, G. T.; DeGrado, W. F., Designed metalloprotein stabilizes a semiquinone radical. *Nature Chemistry* **2016**, 8, 354; (b) Guin, P. S.; Das, S.; Mandal, P. C., Electrochemical Reduction of Quinones in Different Media: A Review. *International Journal of Electrochemistry* **2011**, 2011, 22.
47. Benelli, C.; Dei, A.; Gatteschi, D.; Pardi, L., Redox potentials and charge transfer spectra of catecholate and semiquinone adducts of a cobalt-tetraazamacrocyclic complex. *Inorganica Chimica Acta* **1989**, 163 (1), 99-104.
48. Armarego, W. L. F.; Chai, C. L. L., Chapter 4 - Purification of Organic Chemicals. In *Purification of Laboratory Chemicals (Sixth Edition)*, Armarego, W. L. F.; Chai, C. L. L., Eds. Butterworth-Heinemann: Oxford, 2009; pp 88-444.
49. Aaron, P.; L., B. K.; G., N. B.; A., G. A.; G., N. R., Toward a Four-Electron Redox Quinone Polymer for High Capacity Lithium Ion Storage. *Advanced Energy Materials* **2018**, 8 (5), 1700960.
50. Zhiping, S.; Hui, Z.; Yunhong, Z., Polyimides: Promising Energy-Storage Materials. *Angew. Chem. Int. Ed.* **2010**, 49 (45), 8444-8448.
51. (a) Tavassol, H.; Jones, E. M. C.; Sottos, N. R.; Gewirth, A. A., Electrochemical Stiffness Measurements of Graphite Anodes for Li-Ion Batterie. *Meeting Abstracts* **2015**, MA2015-01 (2), 462; (b) Lundberg, K. E.; Capraz, O. O.; Sottos, N. R.; Gewirth, A. A., Asynchronous Stress and Strain Measurements of LiMn₂O₄ Composite Electrodes. *Meeting Abstracts* **2016**, MA2016-03 (2), 532; (c) Çapraz, Ö. Ö.; Bassett, K. L.; Gewirth, A. A.; Sottos, N. R., Electrochemical Stiffness Changes in Lithium Manganese Oxide Electrodes. *Advanced Energy Materials* **2017**, 7 (7), 1601778.
52. (a) Goodenough, J. B.; Kim, Y., Challenges for Rechargeable Li Batteries. *Chem. Mater.* **2010**, 22 (3), 587-603; (b) Goodenough, J. B.; Park, K.-S., The Li-Ion Rechargeable Battery: A Perspective. *J. Am. Chem. Soc.* **2013**, 135 (4), 1167-1176.
53. Tarascon, J. M.; Armand, M., Issues and challenges facing rechargeable lithium batteries. *Nature* **2001**, 414 (6861), 359-367.
54. Bachman, J. C.; Muy, S.; Grimaud, A.; Chang, H.-H.; Pour, N.; Lux, S. F.; Paschos, O.; Maglia, F.; Lupart, S.; Lamp, P.; Giordano, L.; Shao-Horn, Y., Inorganic Solid-State Electrolytes for Lithium Batteries: Mechanisms and Properties Governing Ion Conduction. *Chem. Rev.* **2016**, 116 (1), 140-162.
55. Goodenough, J. B.; Singh, P., Review—Solid Electrolytes in Rechargeable Electrochemical Cells. *J. Electrochem. Soc.* **2015**, 162 (14), A2387-A2392.

56. (a) Long, L.; Wang, S.; Xiao, M.; Meng, Y., Polymer electrolytes for lithium polymer batteries. *J. Mater. Chem. A* **2016**, *4* (26), 10038-10069; (b) Manuel Stephan, A., Review on gel polymer electrolytes for lithium batteries. *Eur. Polym. J.* **2006**, *42* (1), 21-42.
57. (a) Sang, L.; Haasch, R. T.; Gewirth, A. A.; Nuzzo, R. G., Evolution at the Solid Electrolyte/Gold Electrode Interface during Lithium Deposition and Stripping. *Chem. Mater.* **2017**, *29* (7), 3029-3037; (b) Richards, W. D.; Miara, L. J.; Wang, Y.; Kim, J. C.; Ceder, G., Interface Stability in Solid-State Batteries. *Chem. Mater.* **2016**, *28* (1), 266-273; (c) Takada, K.; Ohta, N.; Zhang, L.; Xu, X.; Hang, B. T.; Ohnishi, T.; Osada, M.; Sasaki, T., Interfacial phenomena in solid-state lithium battery with sulfide solid electrolyte. *Solid State Ionics* **2012**, *225*, 594-597.
58. Wiers, B. M.; Foo, M.-L.; Balsara, N. P.; Long, J. R., A Solid Lithium Electrolyte via Addition of Lithium Isopropoxide to a Metal–Organic Framework with Open Metal Sites. *J. Am. Chem. Soc.* **2011**, *133* (37), 14522-14525.
59. (a) Vazquez-Molina, D. A.; Mohammad-Pour, G. S.; Lee, C.; Logan, M. W.; Duan, X.; Harper, J. K.; Uribe-Romo, F. J., Mechanically Shaped Two-Dimensional Covalent Organic Frameworks Reveal Crystallographic Alignment and Fast Li-Ion Conductivity. *J. Am. Chem. Soc.* **2016**, *138* (31), 9767-9770; (b) Du, Y.; Yang, H.; Whiteley, J. M.; Wan, S.; Jin, Y.; Lee, S.-H.; Zhang, W., Ionic Covalent Organic Frameworks with Spiroborate Linkage. *Angew. Chem. Int. Ed.* **2016**, *55* (5), 1737-1741.
60. Van Humbeck, J. F.; Aubrey, M. L.; Alsaiee, A.; Ameloot, R.; Coates, G. W.; Dichtel, W. R.; Long, J. R., Tetraarylborate polymer networks as single-ion conducting solid electrolytes. *Chem. Sci.* **2015**, *6* (10), 5499-5505.
61. Park, J. H.; Suh, K.; Rohman, M. R.; Hwang, W.; Yoon, M.; Kim, K., Solid lithium electrolytes based on an organic molecular porous solid. *Chem. Commun.* **2015**, *51* (45), 9313-9316.
62. (a) Tozawa, T.; Jones, J. T. A.; Swamy, S. I.; Jiang, S.; Adams, D. J.; Shakespeare, S.; Clowes, R.; Bradshaw, D.; Hasell, T.; Chong, S. Y.; Tang, C.; Thompson, S.; Parker, J.; Trewin, A.; Bacsá, J.; Slawin, A. M. Z.; Steiner, A.; Cooper, A. I., Porous organic cages. *Nat. Mater.* **2009**, *8*, 973; (b) Zhang, G.; Presly, O.; White, F.; Oppel, I. M.; Mastalerz, M., A Permanent Mesoporous Organic Cage with an Exceptionally High Surface Area. *Angew. Chem. Int. Ed.* **2014**, *53* (6), 1516-1520.
63. Zhang, C.; Wang, Q.; Long, H.; Zhang, W., A Highly C70 Selective Shape-Persistent Rectangular Prism Constructed through One-Step Alkyne Metathesis. *J. Am. Chem. Soc.* **2011**, *133* (51), 20995-21001.
64. Hasell, T.; Culshaw, J. L.; Chong, S. Y.; Schmidtman, M.; Little, M. A.; Jelfs, K. E.; Pyzer-Knapp, E. O.; Shepherd, H.; Adams, D. J.; Day, G. M.; Cooper, A. I., Controlling the Crystallization of Porous Organic Cages: Molecular Analogs of Isoreticular Frameworks Using Shape-Specific Directing Solvents. *J. Am. Chem. Soc.* **2014**, *136* (4), 1438-1448.
65. Liu, M.; Chen, L.; Lewis, S.; Chong, S. Y.; Little, M. A.; Hasell, T.; Aldous, I. M.; Brown, C. M.; Smith, M. W.; Morrison, C. A.; Hardwick, L. J.; Cooper, A. I., Three-dimensional protonic conductivity in porous organic cage solids. *Nat. Commun.* **2016**, *7*, 12750.
66. (a) Lee, S.; Yang, A.; Moneypenny, T. P.; Moore, J. S., Kinetically Trapped Tetrahedral Cages via Alkyne Metathesis. *J. Am. Chem. Soc.* **2016**, *138* (7), 2182-2185; (b) Moneypenny, T. P.; Walter, N. P.; Cai, Z.; Miao, Y.-R.; Gray, D. L.; Hinman, J. J.; Lee, S.; Zhang, Y.; Moore, J. S., Impact of Shape Persistence on the Porosity of Molecular Cages. *J. Am. Chem. Soc.* **2017**, *139* (8), 3259-3264.

67. (a) Forsyth, M.; Pringle, J. M.; MacFarlane, D. R., Ion Conduction in Organic Ionic Plastic Crystals. In *Electrochemical Aspects of Ionic Liquids*, John Wiley & Sons, Inc.: Hoboken, New Jersey, 2011; pp 347-373; (b) McGrath, K. J.; Weiss, R. G., NMR Investigation of Molecular Motion in the Neat Solid and Plastic-Crystalline Phases of Cyclohexane. *Langmuir* **1997**, *13* (16), 4474-4479.
68. Fulmer, G. R.; Miller, A. J. M.; Sherden, N. H.; Gottlieb, H. E.; Nudelman, A.; Stoltz, B. M.; Bercaw, J. E.; Goldberg, K. I., NMR Chemical Shifts of Trace Impurities: Common Laboratory Solvents, Organics, and Gases in Deuterated Solvents Relevant to the Organometallic Chemist. *Organometallics* **2010**, *29* (9), 2176-2179.
69. Han, S.-D.; Borodin, O.; Seo, D. M.; Zhou, Z.-B.; Henderson, W. A., Electrolyte Solvation and Ionic Association: V. Acetonitrile-Lithium Bis(fluorosulfonyl)imide (LiFSI) Mixtures. *J. Electrochem. Soc.* **2014**, *161* (14), A2042-A2053.
70. Suo, L.; Hu, Y.-S.; Li, H.; Armand, M.; Chen, L., A new class of Solvent-in-Salt electrolyte for high-energy rechargeable metallic lithium batteries. *Nat. Commun.* **2013**, *4*, 1481.
71. Arvai, R.; Toulgoat, F.; Langlois, B. R.; Sanchez, J.-Y.; Médebielle, M., A simple access to metallic or onium bistrifluoromethanesulfonimide salts. *Tetrahedron* **2009**, *65* (27), 5361-5368.
72. (a) Archer, W. I.; Armstrong, R. D., The application of A. C. impedance methods to solid electrolytes. In *Electrochemistry: Volume 7*, Thirsk, H. R., Ed. The Royal Society of Chemistry: 1980; Vol. 7, pp 157-202; (b) *Impedance Spectroscopy Theory, Experiment, and Applications*. 1 ed.; John Wiley & Sons, Inc: Hoboken, New Jersey., 2005; p 595.
73. (a) Gao, H.; Guo, B.; Song, J.; Park, K.; Goodenough, J. B., A Composite Gel-Polymer/Glass-Fiber Electrolyte for Sodium-Ion Batteries. *Advanced Energy Materials* **2015**, *5* (9), 1402235; (b) Appetecchi, G. B.; Croce, F.; De Paolis, A.; Scrosati, B., A poly(vinylidene fluoride)-based gel electrolyte membrane for lithium batteries. *J. Electroanal. Chem.* **1999**, *463* (2), 248-252; (c) Panero, S.; Scrosati, B., Gelification of liquid-polymer systems: a valid approach for the development of various types of polymer electrolyte membranes. *J. Power Sources* **2000**, *90* (1), 13-19.
74. Saikia, D.; Kumar, A., Ionic conduction in P(VDF-HFP)/PVDF-(PC + DEC)-LiClO₄ polymer gel electrolytes. *Electrochim. Acta* **2004**, *49* (16), 2581-2589.
75. Zhao, N.; Lloyd, G. O.; Scherman, O. A., Monofunctionalised cucurbit[6]uril synthesis using imidazolium host-guest complexation. *Chem. Commun.* **2012**, *48* (25), 3070-3072.
76. (a) Chandra, S., *Superionic Solids*. North-Holland: Amsterdam, 1981; (b) Kamaya, N.; Homma, K.; Yamakawa, Y.; Hirayama, M.; Kanno, R.; Yonemura, M.; Kamiyama, T.; Kato, Y.; Hama, S.; Kawamoto, K.; Mitsui, A., A lithium superionic conductor. *Nat Mater* **2011**, *10* (9), 682-686.
77. (a) Matsumoto, K.; Inoue, K.; Nakahara, K.; Yuge, R.; Noguchi, T.; Utsugi, K., Suppression of aluminum corrosion by using high concentration LiTFSI electrolyte. *J. Power Sources* **2013**, *231* (Supplement C), 234-238; (b) Zheng, J.; Lochala, J. A.; Kwok, A.; Deng, Z. D.; Xiao, J., Research Progress towards Understanding the Unique Interfaces between Concentrated Electrolytes and Electrodes for Energy Storage Applications. *Adv. Sci.* **2017**, *4* (8), 1700032; (c) McOwen, D. W.; Seo, D. M.; Borodin, O.; Vatamanu, J.; Boyle, P. D.; Henderson, W. A., Concentrated electrolytes: decrypting electrolyte properties and reassessing Al corrosion mechanisms. *Energ. Environ. Sci.* **2014**, *7* (1), 416-426.

78. Li, L.-F.; Totir, D.; Gofer, Y.; Chottiner, G. S.; Scherson, D. A., The electrochemistry of nickel in a lithium-based solid polymer electrolyte in ultrahigh vacuum environments. *Electrochim. Acta* **1998**, *44* (6), 949-955.
79. Liu, Z.; Fu, W.; Payzant, E. A.; Yu, X.; Wu, Z.; Dudney, N. J.; Kiggans, J.; Hong, K.; Rondinone, A. J.; Liang, C., Anomalous High Ionic Conductivity of Nanoporous β -Li₃PS₄. *J. Am. Chem. Soc.* **2013**, *135* (3), 975-978.
80. Seino, Y.; Ota, T.; Takada, K.; Hayashi, A.; Tatsumisago, M., A sulphide lithium super ion conductor is superior to liquid ion conductors for use in rechargeable batteries. *Energ. Environ. Sci.* **2014**, *7* (2), 627-631.
81. Xu, K., Nonaqueous liquid electrolytes for lithium-based rechargeable batteries. *Chem Rev* **2004**, *104* (10), 4303-4417.
82. Jarry, A.; Gottis, S.; Yu, Y. S.; Roque-Rosell, J.; Kim, C.; Cabana, J.; Kerr, J.; Kostecki, R., The Formation Mechanism of Fluorescent Metal Complexes at the Li_xNi_{0.5}Mn_{1.5}O₄-delta/Carbonate Ester Electrolyte Interface. *J Am Chem Soc* **2015**, *137* (10), 3533-3539.
83. Zhan, C.; Lu, J.; Kropf, A. J.; Wu, T. P.; Jansen, A. N.; Sun, Y. K.; Qiu, X. P.; Amine, K., Mn(II) deposition on anodes and its effects on capacity fade in spinel lithium manganese-carbon systems. *Nat Commun* **2013**, *4*.
84. (a) Liu, Y. M.; Nicolau, B. G.; Esbenschade, J. L.; Gewirth, A. A., Characterization of the Cathode Electrolyte Interface in Lithium Ion Batteries by Desorption Electrospray Ionization Mass Spectrometry. *Anal Chem* **2016**, *88* (14), 7171-7177; (b) Nicolau, B. G.; Garcia-Rey, N.; Dryzhakov, B.; Dlott, D. D., Interfacial Processes of a Model Lithium Ion Battery Anode Observed, in Situ, with Vibrational Sum-Frequency Generation Spectroscopy. *J Phys Chem C* **2015**, *119* (19), 10227-10233.
85. Esbenschade, J. L.; Gewirth, A. A., Effect of Mn and Cu Addition on Lithiation and SEI Formation on Model Anode Electrodes. *J Electrochem Soc* **2014**, *161* (4), A513-A518.
86. Ha, H. W.; Yun, N. J.; Kim, K., Improvement of electrochemical stability of LiMn₂O₄ by CeO₂ coating for lithium-ion batteries. *Electrochim Acta* **2007**, *52* (9), 3236-3241.
87. Esbenschade, J. L.; Fox, M. D.; Gewirth, A. A., LiMn₂O₄@Au Particles as Cathodes for Li-Ion Batteries. *J Electrochem Soc* **2015**, *162* (1), A26-A29.
88. Jaber-Ansari, L.; Puntambekar, K. P.; Kim, S.; Aykol, M.; Luo, L. L.; Wu, J. S.; Myers, B. D.; Iddir, H.; Russell, J. T.; Saldana, S. J.; Kumar, R.; Thackeray, M. M.; Curtiss, L. A.; Dravid, V. P.; Wolverton, C.; Hersam, M. C., Suppressing Manganese Dissolution from Lithium Manganese Oxide Spinel Cathodes with Single-Layer Graphene. *Adv Energy Mater* **2015**, *5* (17).
89. Pujari, S. P.; Scheres, L.; Marcelis, A. T. M.; Zuilhof, H., Covalent Surface Modification of Oxide Surfaces. *Angew Chem Int Edit* **2014**, *53* (25), 6322-6356.
90. (a) Paniagua, S. A.; Li, E. L.; Marder, S. R., Adsorption studies of a phosphonic acid on ITO: film coverage, purity, and induced electronic structure changes. *Phys Chem Chem Phys* **2014**, *16* (7), 2874-2881; (b) Queffelec, C.; Petit, M.; Janvier, P.; Knight, D. A.; Bujoli, B., Surface Modification Using Phosphonic Acids and Esters. *Chem Rev* **2012**, *112* (7), 3777-3807; (c) Hotchkiss, P. J.; Jones, S. C.; Paniagua, S. A.; Sharma, A.; Kippelen, B.; Armstrong, N. R.; Marder, S. R., The Modification of Indium Tin Oxide with Phosphonic Acids: Mechanism of Binding, Tuning of Surface Properties, and Potential for Use in Organic Electronic Applications. *Accounts Chem Res* **2012**, *45* (3), 337-346.
91. Zettsu, N.; Kida, S.; Uchida, S.; Teshima, K., Sub-2 nm Thick Fluoroalkylsilane Self-Assembled Monolayer-Coated High Voltage Spinel Crystals as Promising Cathode Materials for Lithium Ion Batteries. *Sci Rep-Uk* **2016**, *6*.

92. Zoski, C. G., *Handbook of Electrochemistry*. Elsevier: Amsterdam, 2007.
93. Leopold, M. C.; Doan, T. T.; Mullaney, M. J.; Loftus, A. F.; Kidd, C. M., Electrochemical characterization of self-assembled monolayers on gold substrates derived from thermal decomposition of monolayer-protected cluster films. *J Appl Electrochem* **2015**, *45* (10), 1069-1084.
94. (a) Hoang, K., Understanding the electronic and ionic conduction and lithium over-stoichiometry in LiMn₂O₄ spinel. *J Mater Chem A* **2014**, *2* (43), 18271-18280; (b) Iguchi, E.; Tokuda, Y.; Nakatsugawa, H.; Munakata, F., Electrical transport properties in LiMn₂O₄, Li_{0.95}Mn₂O₄, and LiMn_{1.95}B_{0.05}O₄ (B=Al or Ga) around room temperature. *J Appl Phys* **2002**, *91* (4), 2149-2154.
95. Laoire, C. O.; Plichta, E.; Hendrickson, M.; Mukerjee, S.; Abraham, K. M., Electrochemical studies of ferrocene in a lithium ion conducting organic carbonate electrolyte. *Electrochim Acta* **2009**, *54* (26), 6560-6564.
96. (a) Sur, U. K.; Lakshminarayanan, V., Effect of bulk structure of some non-aqueous solvents on the barrier properties of alkanethiol monolayer. *J Electroanal Chem* **2001**, *516* (1-2), 31-38; (b) Nikitina, V. A.; Rudnev, A. V.; Tsirlina, G. A.; Wandlowski, T., Long Distance Electron Transfer at the Metal/Alkanethiol/Ionic Liquid Interface. *J Phys Chem C* **2014**, *118* (29), 15970-15977.
97. Jayanth-Babu, K.; Jeevan-Kumar, P.; Hussain, O. M.; Julien, C. M., Influence of annealing temperature on microstructural and electrochemical properties of rf-sputtered LiMn₂O₄ film cathodes. *J Solid State Electr* **2012**, *16* (10), 3383-3390.
98. Shui, J. L.; Jiang, G. S.; Xie, S.; Chen, C. H., Thin films of lithium manganese oxide spinel as cathode materials for secondary lithium batteries. *Electrochim Acta* **2004**, *49* (13), 2209-2213.
99. (a) Schmidt, J. P.; Chrobak, T.; Ender, M.; Illig, J.; Klotz, D.; Ivers-Tiffée, E., Studies on LiFePO₄ as cathode material using impedance spectroscopy. *J Power Sources* **2011**, *196* (12), 5342-5348; (b) Crain, D.; Zheng, J. P.; Sulyma, C.; Goia, C.; Goia, D.; Roy, D., Electrochemical features of ball-milled lithium manganate spinel for rapid-charge cathodes of lithium ion batteries. *J Solid State Electr* **2012**, *16* (8), 2605-2615.
100. Inamoto, J.-i.; Fukutsuka, T.; Miyazaki, K.; Abe, T., Investigation on Surface-Film Formation Behavior of LiMn₂O₄ Thin-Film Electrodes in LiClO₄/Propylene Carbonate. *ChemistrySelect* **2017**, *2* (10), 2895-2900.
101. Muthurasu, A.; Ganesh, V., Electrochemical characterization of Self-assembled Monolayers (SAMs) of silanes on indium tin oxide (ITO) electrodes - Tuning electron transfer behaviour across electrode-electrolyte interface. *J Colloid Interf Sci* **2012**, *374*, 241-249.
102. Militello, M. C.; Gaarenstroom, S. W., Lithium Manganese Oxide (LiMn₂O₄)(LiMn₂O₄) by XPS. *Surface Science Spectra* **2001**, *8* (3), 207-213.
103. (a) Sato, K.; Haruta, H.; Kumashiro, Y., Ab initio molecular-orbital study on the surface reactions of methane and silane plasma chemical vapor deposition. *Phys Rev B* **1997**, *55* (23), 15467-15470; (b) Sato, K.; Poojary, D. M.; Clearfield, A.; Kohno, M.; Inoue, Y., The surface structure of the proton-exchanged lithium manganese oxide spinels and their lithium-ion sieve properties. *J Solid State Chem* **1997**, *131* (1), 84-93.
104. Moulder, J. F.; Stickle, W. F.; Sobol, P. E.; Bomben, K. D., Handbook of X-ray Photoelectron Spectroscopy. In *PHI-Handbook: Handbook of X-ray Photoelectron Spectroscopy*, Physical Electronics: Eden Prairie, MN, 1992.

105. Hoque, E.; DeRose, J. A.; Bhushan, B.; Hipps, K. W., Low adhesion, non-wetting phosphonate self-assembled monolayer films formed on copper oxide surfaces. *Ultramicroscopy* **2009**, *109* (8), 1015-1022.
106. (a) Haasch, R. T., X-Ray Photoelectron Spectroscopy (XPS) and Auger Electron Spectroscopy (AES). In *Practical Materials Characterization*, Sardela, M., Ed. Springer New York: New York, NY, 2014; pp 93-132; (b) Petrovykh, D. Y.; Kimura-Suda, H.; Whitman, L. J.; Tarlov, M. J., Quantitative analysis and characterization of DNA immobilized on gold. *J Am Chem Soc* **2003**, *125* (17), 5219-5226; (c) Lane, S. M.; Monot, J.; Petit, M.; Bujoli, B.; Talham, D. R., XPS investigation of DNA binding to zirconium-phosphonate surfaces. *Colloid Surface B* **2007**, *58* (1), 34-38; (d) Lane, S. M.; Monot, J.; Petit, M.; Tellier, C.; Bujoli, B.; Talham, D. R., Poly(dG) spacers lead to increased surface coverage of DNA probes: An XPS study of oligonucleotide binding to zirconium phosphonate modified surfaces. *Langmuir* **2008**, *24* (14), 7394-7399.
107. Paniagua, S. A.; Hotchkiss, P. J.; Jones, S. C.; Marder, S. R.; Mudalige, A.; Marrikar, F. S.; Pemberton, J. E.; Armstrong, N. R., Phosphonic acid modification of indium-tin oxide electrodes: Combined XPS/UPS/contact angle studies. *J Phys Chem C* **2008**, *112* (21), 7809-7817.
108. Hofinger, S.; Zerbetto, F., Simple models for hydrophobic hydration. *Chem Soc Rev* **2005**, *34* (12), 1012-1020.
109. Warburton, R. E.; Iddir, H.; Curtiss, L. A.; Greeley, J., Thermodynamic Stability of Low- and High-Index Spinel LiMn₂O₄ Surface Terminations. *Acs Appl Mater Inter* **2016**, *8* (17), 11108-11121.
110. Li, H.; Paramonov, P.; Bredas, J. L., Theoretical study of the surface modification of indium tin oxide with trifluorophenyl phosphonic acid molecules: impact of coverage density and binding geometry. *J Mater Chem* **2010**, *20* (13), 2630-2637.
111. Paniagua, S. A.; Giordano, A. J.; Smith, O. L.; Barlow, S.; Li, H.; Armstrong, N. R.; Pemberton, J. E.; Bredas, J. L.; Ginger, D.; Marder, S. R., Phosphonic Acids for Interfacial Engineering of Transparent Conductive Oxides. *Chem Rev* **2016**, *116* (12), 7117-7158.
112. (a) Fischer, J.; Adelhelm, C.; Bergfeldt, T.; Chang, K.; Ziebert, C.; Leiste, H.; Stuber, M.; Ulrich, S.; Music, D.; Hallstedt, B.; Seifert, H. J., Development of thin film cathodes for lithium-ion batteries in the material system Li-Mn-O by r.f. magnetron sputtering. *Thin Solid Films* **2013**, *528*, 217-223; (b) Fischer, J.; Music, D.; Bergfeldt, T.; Ziebert, C.; Ulrich, S.; Seifert, H. J., Experimental and ab initio investigations on textured Li-Mn-O spinel thin film cathodes. *Thin Solid Films* **2014**, *572*, 208-215.
113. Verma, P.; Maire, P.; Novak, P., A review of the features and analyses of the solid electrolyte interphase in Li-Ion batteries. *Electrochim Acta* **2010**, *55* (22), 6332-6341.
114. Huff, L. A.; Rapp, J. L.; Baughman, J. A.; Rinaldi, P. L.; Gewirth, A. A., Identification of lithium-sulfur battery discharge products through Li-6 and S-33 solid-state MAS and Li-7 solution NMR spectroscopy. *Surf Sci* **2015**, *631*, 295-300.
115. Plimpton, S.; Thompson, A.; P. Crozier, L. LAMMPS Molecular Dynamics Simulator. <http://lammmps.sandia.gov>.
116. (a) Nose, S.; Klein, M. L., Constant Pressure Molecular-Dynamics for Molecular-Systems. *Mol Phys* **1983**, *50* (5), 1055-1076; (b) Nose, S., A Unified Formulation of the Constant Temperature Molecular-Dynamics Methods. *J Chem Phys* **1984**, *81* (1), 511-519; (c) Hoover, W. G., Canonical Dynamics - Equilibrium Phase-Space Distributions. *Phys Rev A* **1985**, *31* (3), 1695-1697.

117. Verlet, L., Computer Experiments on Classical Fluids .I. Thermodynamical Properties of Lennard-Jones Molecules. *Phys Rev* **1967**, *159* (1), 98-+.
118. Petrosyan, S. A.; Rigos, A. A.; Arias, T. A., Joint density-functional theory: Ab initio study of Cr₂O₃ surface chemistry in solution. *J Phys Chem B* **2005**, *109* (32), 15436-15444.
119. Gunceler, D.; Letchworth-Weaver, K.; Sundararaman, R.; Schwarz, K. A.; Arias, T. A., The importance of nonlinear fluid response in joint density-functional theory studies of battery systems. *Model Simul Mater Sc* **2013**, *21* (7).
120. Dudarev, S. L.; Botton, G. A.; Savrasov, S. Y.; Humphreys, C. J.; Sutton, A. P., Electron-energy-loss spectra and the structural stability of nickel oxide: An LSDA+U study. *Phys Rev B* **1998**, *57* (3), 1505-1509.
121. (a) Eftekhari, A.; Kim, D.-W., Cathode materials for lithium–sulfur batteries: a practical perspective. *Journal of Materials Chemistry A* **2017**, *5* (34), 17734-17776; (b) Fan, X.; Sun, W.; Meng, F.; Xing, A.; Liu, J., Advanced chemical strategies for lithium–sulfur batteries: A review. *Green Energy & Environment* **2018**, *3* (1), 2-19; (c) Manthiram, A.; Fu, Y.; Chung, S.-H.; Zu, C.; Su, Y.-S., Rechargeable Lithium–Sulfur Batteries. *Chemical Reviews* **2014**, *114* (23), 11751-11787; (d) Peng, H.-J.; Huang, J.-Q.; Cheng, X.-B.; Zhang, Q., Lithium-Sulfur Batteries: Review on High-Loading and High-Energy Lithium–Sulfur Batteries (Adv. Energy Mater. 24/2017). *Advanced Energy Materials* **2017**, *7* (24), 1770141.
122. (a) Burgos, J. C.; Balbuena, P. B.; Montoya, J. A., Structural Dependence of the Sulfur Reduction Mechanism in Carbon-Based Cathodes for Lithium–Sulfur Batteries. *The Journal of Physical Chemistry C* **2017**, *121* (34), 18369-18377; (b) Zheng, D.; Zhang, X.; Wang, J.; Qu, D.; Yang, X.; Qu, D., Reduction mechanism of sulfur in lithium–sulfur battery: From elemental sulfur to polysulfide. *Journal of Power Sources* **2016**, *301*, 312-316.
123. (a) Liu, J.; Lu, D.; Zheng, J.; Yan, P.; Wang, B.; Sun, X.; Shao, Y.; Wang, C.; Xiao, J.; Zhang, J.-G.; Liu, J., Minimizing Polysulfide Shuttle Effect in Lithium-Ion Sulfur Batteries by Anode Surface Passivation. *ACS Applied Materials & Interfaces* **2018**, *10* (26), 21965-21972; (b) Seh, Z. W.; Sun, Y.; Zhang, Q.; Cui, Y., Designing high-energy lithium–sulfur batteries. *Chemical Society Reviews* **2016**, *45* (20), 5605-5634; (c) Yu, X.; Manthiram, A., Electrode–Electrolyte Interfaces in Lithium–Sulfur Batteries with Liquid or Inorganic Solid Electrolytes. *Accounts of Chemical Research* **2017**, *50* (11), 2653-2660.
124. (a) Ma, Y.; Zhang, H.; Wu, B.; Wang, M.; Li, X.; Zhang, H., Lithium Sulfur Primary Battery with Super High Energy Density: Based on the Cauliflower-like Structured C/S Cathode. *Scientific Reports* **2015**, *5*, 14949; (b) Wang, D.-W.; Zeng, Q.; Zhou, G.; Yin, L.; Li, F.; Cheng, H.-M.; Gentle, I. R.; Lu, G. Q. M., Carbon–sulfur composites for Li–S batteries: status and prospects. *Journal of Materials Chemistry A* **2013**, *1* (33), 9382-9394.
125. Simmonds, A. G.; Griebel, J. J.; Park, J.; Kim, K. R.; Chung, W. J.; Oleshko, V. P.; Kim, J.; Kim, E. T.; Glass, R. S.; Soles, C. L.; Sung, Y.-E.; Char, K.; Pyun, J., Inverse Vulcanization of Elemental Sulfur to Prepare Polymeric Electrode Materials for Li–S Batteries. *ACS Macro Letters* **2014**, *3* (3), 229-232.
126. Yue, J.; Epstein, A. J., Synthesis of self-doped conducting polyaniline. *Journal of the American Chemical Society* **1990**, *112* (7), 2800-2801.
127. Petronico, A.; Moneypenny, T. P.; Nicolau, B. G.; Moore, J. S.; Nuzzo, R. G.; Gewirth, A. A., Solid–Liquid Lithium Electrolyte Nanocomposites Derived from Porous Molecular Cages. *Journal of the American Chemical Society* **2018**, *140* (24), 7504-7509.

128. Jiménez, P.; Levillain, E.; Alévêque, O.; Guyomard, D.; Lestriez, B.; Gaubicher, J., Lithium n-Doped Polyaniline as a High-Performance Electroactive Material for Rechargeable Batteries. *Angewandte Chemie International Edition* **2017**, *56* (6), 1553-1556.